Atomic-scale In Situ TEM Investigation of Grain Boundary Deformation Behavior in FCC Gold

by

Zhengwu Fang

B.E., Central South University, China, 2015

M.E., Central South University, China, 2018

Submitted to the Graduate Faculty of the

Swanson School of Engineering in partial fulfillment

of the requirements for the degree of

Doctor of Philosophy

University of Pittsburgh

2023

UNIVERSITY OF PITTSBURGH

SWANSON SCHOOL OF ENGINEERING

This dissertation was presented

by

Zhengwu Fang

It was defended on

August 30, 2023

and approved by

Patrick Smolinski, Ph.D., Associate Professor, Department of Mechanical Engineering and Materials Science

Qihan Liu, Ph.D., Assistant Professor, Department of Mechanical Engineering and Materials Science

Feng Xiong, Associate Professor, Department of Electrical and Computer Engineering

Dissertation Director: **Guofeng Wang**, Ph.D., Professor, Department of Mechanical Engineering and Materials Science

Copyright © by Zhengwu Fang

2023

ATOMIC-SCALE IN SITU TEM INVESTIGATION OF GRAIN BOUNDARY DEFORMATION BEHAVIOR IN FCC GOLD

Zhengwu Fang, PhD

University of Pittsburgh, 2023

The deformation mechanism of metallic polycrystalline materials is known to transform from dislocation-mediated plasticity into grain boundary (GB)-mediated plasticity when the crystal size decreases to sub-10 nm. Numerous studies have been performed in the past decades to reveal the mechanisms of GB deformation. However, the dynamic process of GB deformation at the atomic scale remains largely unclear due to the lack of real-time experimental observation. In this dissertation, in-situ high-resolution transmission electron microscopy (HRTEM) combined with molecular dynamics (MD) simulations have been employed to investigate the typical GB deformation behavior in face-centered cubic (FCC) gold (Au) nanocrystals at the atomic scale.

Dynamic GB structural transformation arising from reversible facet transformation and GB dissociation was observed during the migration of faceted GBs. It is found that the types of steps/disconnections mediating the migration of GB facets determine which pathway the GB structural transformation follows. Moreover, the loading dependence of GB facet transformation and the roles of GB junctions in accommodating GB migration and structural transformation are clarified.

Regarding the case of mixed tilt-twist GB, two distinct migration patterns showing the opposite signs of shear-coupling factor were observed, and further revealed to be mediated by the motion of GB disconnections with different crystallographic parameters and exhibit different lattice correspondence relations. MD simulation results confirm that the two distinct migration

patterns could be activated under different stress/strain states. Furthermore, excess GB sliding and GB plane reorientation were found to accommodate the GB migration in both experiments and simulations, as to establish a point-to-point lattice correspondence during GB migration.

Additionally, the deformation-induced formation and annihilation of a typical HAGB in an Au nanocrystal upon reciprocating bending deformation was investigated. HAGB formation underwent the process of accumulation, alignment, further accumulation, and eventually exhaustion of geometrically necessary dislocations. In comparison, HAGB annihilation was accomplished by the synergic operation of GB structure reconstruction, emission of partial and full dislocations, and twinning.

This dissertation advances the fundamental understanding of atomic-scale GB deformation behavior in FCC materials and provides important guidelines for the future development of ductile nanocrystalline materials and reliable nanocrystal components in nano electromechanical systems devices.

Table of Contents

1.0 Introduction 1

2.0 Background 5

- **2.1 Experimental investigation on deformation-induced GB migration 5**
- **2.2 Theoretical models for shear-coupled GB migration 10**
  - **2.2.1 CSL/DSC lattice model 10**
  - **2.2.2 Cahn model 13**
  - **2.2.3 Shear migration geometrical (SMIG) model 14**
  - **2.2.4 The unified GB disconnection model 17**
- **2.3 Computational simulations on shear-coupled GB migration 20**
- **2.4 Deformation-induced formation and annihilation of GBs 26**
- **2.5 Motivation and Objectives 30**

3.0 Materials and Experimental Procedures 32

- **3.1 Materials 32**
- **3.2 Experimental Procedures 33**
  - **3.2.1 In-situ TEM experimental configuration 33**
  - **3.2.2 Fabrication of nano bi-crystals with desirable GB structure. 35**
  - **3.2.3 GB plane identification 37**
- **3.3 Simulation methods 39**

4.0 Atomic-scale observation of dynamic grain boundary structural transformation during shear-mediated migration 43

- **4.1 Introduction 44**

4.2 Experimental results 46

4.2.1 Back-and-forth GB plane reorientation during shear-mediated migration.46

4.2.2 Reversible facet transformation between the ATGB and the STGB 50

4.2.3 Grain boundary dissociation during migration 57

4.3 Discussion 61

4.4 Conclusion 69

5.0 Revealing shear-coupled migration mechanism of a mixed tilt-twist GB at atomic scale.. 71

5.1 Introduction 72

5.2 Experimental results 74

5.2.1 Two distinct types of migration behavior of an identical GB 74

5.2.2 Atomistic processes of the two distinct types of GB migration......................76

5.2.3 Theoretical analysis of the GB disconnections 79

5.2.4 MD simulation of two types of GB migration...84

5.2.5 Origin of excess GB sliding and GB plane reorientation...............................88

5.3 Discussion 94

5.4 Conclusion 99

6.0 In-situ observation of formation and annihilation of a HAGB in an Au nanocrystal 101

6.1 Introduction 101

6.2 Experimental results 103

6.2.1 Dynamic process of the deformation-induced formation of a HAGB.........103

6.2.2 Fully annihilation of the as-formed HAGB upon reversal deformation.....106

6.2.3 MD simulation results of the HAGB annihilation..111

6.3 Discussion 114

6.4 Conclusion 116

7.0 Summary and conclusions... 117

8.0 Outlook.. 119

Bibliography 123

List of Tables

Table 3.1 Applied strains, dimensions, and GB energy of bicrystal models 42

Table 5.1 Crystallographic parameters of two admissible one-layer disconnections. be and bs represent the Burgers vectors of their edge and screw components, and bp indicates the Burgers vector component that is perpendicular to the GB plane. 82

Table 6.1 Theoretically calculated GB energy of different GBs based on GB energy function for FCC metals*[212]* 106

List of Figures

Figure 1.1 Schematic of GB classification based on the crystallographic description.(a) the symmetrical tilt GB (STGB), (b) the asymmetrical tilt GB (ATGB), (c) the general mixed tilt-twist GB, and (d) the pure twist GB (TwGB).[7].. 2

Figure 2.1 In-situ TEM observations of stress-driven/assisted GB migration in nanocrystalline Al. (a-d) Sequential dark-field TEM images showing the growth of grain A towards grain B by fast GB migration at room temperature [33]. (e-h) Sequential bright-field TEM images showing the grain growth via the migration of faceted GBs under applied stress at 350 °C [34]. (i, j) Bright-field TEM images of the same region containing three joint GBs before (i) and after (j) the stress-induced GB migration, respectively. (k) The superimposed image of (i) and (j). (l) Schematic showing the mechanism of GB triple junction on accommodating the GB migration [35]... 7

Figure 2.2 Concurrent GB migration and grain rotation during the deformation of nanocrystalline Au [36]. (a) Low-magnification TEM image of the sample. (b, c) HRTEM images of the GB network before (b) and after (c) the deformation. (d, e) Enlarged observation on the GB structure in the regions enclosed by the yellow dash boxes in (b) and (c), showing that the GB was consist of an array of GB dislocations. 9

Figure 2.3 Diagrams illustrating the CSL/DSC lattice model. (a) Example of constructing a coincidence-site lattice in an originally rectangular lattice [45]. (b) Coincidence-site lattices with different Σ values for [111] rotations in cubic crystals [45]. (c)

Coincidence-site lattice and displacement shift complete (DSC) lattice in a Σ5 bi-crystal for 36.9° <100> rotation [7]. Arrows in green indicate the DSC vectors. (d) Admission DSC dislocations that can lead to the normal migration of a Σ13a [010] pure tilt GB[34]. 12

Figure 2.4 Comparison of Cahn model and shear migration geometrical (SMIG) model. (a-c) The coupled glide of GB dislocations and grain rotation lead to the GB migration.[53] (d) Plots of predicted shear-coupling factors versus the misorientaion angle of <100>tilt STGBs based on Cahn model. Shear-coupling factors of typical CSL GBs obtained by molecular dynamic simulations are also given for comparsion[53]. (e) Schematic showing the transformations between parallelograms with the same area[58]. (f) Plots of predicted shear-coupling factors versus the misorientaion angle of <100>tilt STGBs based on SMIG model[59]. 16

Figure 2.5 The unifed disconnection model for GB kinetics. (a) Schematic of creating a GB disconnection by jointing two crystals with incompatible surface steps[65]. (b) Example of constructing Burgers circuit around a GB disconneciton on a Σ5 {210} STGB[7]. (c) Example of predicting the admissible disconnections for a Σ17 {410} STGB[69]. (d) Schmatic of the homogeneous nucleation of a disconnection dipole[7]. 19

Figure 2.6 Snapshots of MD simulations showing the atomic movements during the three types of deformation mode[77]. (a) GB sliding mediated by the ramdon atomic shuffing. (b) Emission of a partial dislocation, as indicated by the emergence of a stacking fault (SF), at a free volumn of the GB. (c) GB migration accommodated by the collective movement of atoms. 22

Figure 2.7 Atomistic mechanisms of the thermal-induced migration of mixed tilt-twist GBs in vicinal to the <111> Σ 7 STGB in Al [105, 106]. (a,d) The bicrystal models used for constructing the GBs. Snapshots (b, e) and enlarged views(c, f) of MD simulations showing the equilibrium structure of the facted mixed GB(b, c) and the kinked mixed GB(e, f). (g) Snapshot showing the structure of faceted GB. (h, i) Views of these GB disconnections (steps) from different directions by applying the step-detection algorithm.. 26

Figure 2.8 Mechanical-induced formation of GBs in an Au nanocrystal[124] (a-c) and in the Ni nanowire[134] (d-g). (a)Formation of a 15° LAGB during the off-axial deforamtion of an Au nanocrystal. (b) Fourier filtered images showing that the LAGB is consisted of arrays of full dislocations. (c) Crystal lattice recovered to it pristine state after the release of stress. (d) Atomic structure of the Ni nanowire before bending. (e-g) Bending induced formation of a 17.4° flat GB in the Ni nanowire. 29

Figure 3.1 (a) Fracture surface of the flat Au substrate with plenty of nano-tips on it. (b) HRTEM image of a typical Au nano-tip. The zone axis of the nano-tip is 011. Insert is the correspodning fast fourier transformation (FFT) pattern of the HRTEM image, which agrees well with the features of 011-oriented pattern of FCC Au. Scale bar: (a) 200 nm; (b) 5 nm. 33

Figure 3.2 In-situ TEM experimental configuration used in this work. (a) photo of FEI Titan Themis G2 200 probe Cs corrected STEM at the NFCF lab. (b) The configuration at the head of Nanofactory, which contains the fixed sample side and the movable probe side. (c) The approaching two sides under the TEM observation. x, y, and z axes indicate the motion directions of the probe side. 34

Figure 3.3 Experimental set-up and examples of fabricating nano bicrystals with desirable GB structure. (a) The positions of the sample side and the probe side before the fabrication crystal. (b-d) Examples of as-fabricated GB structure: 011-tilt 15° LAGB (b); 011-tilt 59° HAGB (c); 110-twist 45° GB (d); mixed tilt-twist GB (e). 36

Figure 3.4 The identification of faceted GBs. (a, b) Two types of faceted ATGBs which both contain the $(002)/(111)$ GB facet. The blue dash lines indicate the 111 lattice planes. The yellow dash lines indicate the positions of GB planes. (c) The contrast intensity line profiles are extracted along the orange solid lines in (a). For a clear comparison, the line profiles were selected to make sure the sixth and the seventh atom columns be on the two sides of the interfacial steps. Scale bar: 2nm 38

Figure 3.5 Schematic of the bicrystal computational cells and corresponding optimized atomistic structure for $(10\ 10\ 7)/(10\ 10\ 7)$ STGB (a,c) and $(1\ 1\ 3)/(7\ 7\ 1)$ ATGB (b,d). Figure 4.4e-h and Figure 4.6d-f are captured from different regions at the faceted $(10\ 10\ 7)/(10\ 10\ 7)$ STGB, as indicated by the dashed rectangles in (c). Figure 4.9 are captured from the region as indicated by the dashed rectangles in (d). 40

Figure 3.6 Schematic (a) and crystallographic orientations (b-d) of the Au bicrystal models used in MD simulations. 41

Figure 4.1 Stress-driven migration of a faceted grain boundary (GB) accompanied by back-and-forth GB plane reorientation and reversible facet transformation. (a) Structure of an as-fabricated Au bicrystal with a faceted GB consisting of $(002)/(111)$ ATGBs and several one-atomic-layer $111/002$ steps. The misorientation between the upper and bottom grains in this bicrystal is ~ 53.5°, close to the ideal misorientation angle

(i.e., 54.74°) of $(002)/(111)$ ATGB. Shear stress nearly parallel to the $(002)/(111)$ ATGB was then applied to the bottom grain, as indicated by the white arrow. (b) The $(002)/(111)$ ATGB facets migrated via the lateral motion of $111/002$ steps until a Σ11 (113) STGB facet was formed at the right side of GB. The average GB plane has a clockwise rotation of ~5° during this process. The direction of GB migration is indicated by yellow arrows. (c) The $(002)/(111)$ ATGB and Σ11 (113) STGB facets migrated jointly until another STGB facet was formed at the left side of GB. Then the average GB inclination angle gradually increased to ~20°. (d-h) Sequential snapshots showing the back-and-forth GB plane reorientation and the reversible facet transformation between the STGB and the ATGB facets at the left end (d-f) and the right end (f-h) of GB in this bicrystal. The misorientation angle of the bicrystal in (h) is ~52.16°, indicating a slightly relative grain rotation during the deformation. (i, j) Closer observation of the core structure of $111/002$ steps and the structure of Σ11 (113) STGB. The red dash lines in (b-h) represent the initial position of the as-fabricated faceted GB. Scale bar: (a-h) 2 nm, (i,j) 0.5 nm 47

Figure 4.2 (a) Plots of the average GB inclination angle and the normalized facet ratio of the $(002)/(111)$ ATGB, the Σ11 (113) STGB and the $111/002$ steps versus time. (b) The plot of the normalized facet ratio versus average grain boundary inclination angle. The Σ11 (113) STGB facet exists only when the average inclination is larger than 15° (indicated by the dark dash line).. 49

Figure 4.3 Sequential TEM snapshots showing the joint migration behaviors of the Σ11(113) STGB and the $(002)/(111)$ ATGB facets. (a) A faceted GB composed of the $(002)/(111)$ATGB, $111/002$ step and the Σ11(113) STGB. (b) A $111/002$ step

emitted from the facet junction of (002)/(111)ATGB and Σ11(113) STGB. Σ11(113) STGB kept stationary. (c) Σ11(113) STGB migrated downwards while (002)/(111) ATGB remained stationary. (d) Σ11(113) STGB kept migrating without 111/002 step emitted from the facet junction. Scale bar: 2 nm.. 50

Figure 4.4 Atomistic mechanism of the (002)/(111) ATGB to the Σ11(113) STGB facet transformation. (a) The (002)/(111) ATGB facets connected by a pre-existing 111/002 step. (b-d) Sequential snapshots showing the nucleation and lateral motion of another 111/002 step on the (002)/(111) ATGB, and the formation of a Σ11(113) STGB facet at the right corner of GB. (e-h) Molecular dynamic (MD) simulation showing the same (002)/(111) ATGB to Σ11(113) STGB facet transformation process as the experimental observation. In all MD simulation results, the green, red, and grey atoms indicate the face-centered cubic structure, hexagonal close-packed structure, and other coordination structure (i.e., GB structure), respectively. Dark dash lines in (f-h) represent the positions of GB in the previous snapshot. (i) The contrast intensity line profiles extracted from (a-d) at the same area as indicated by the blue solid line in (a). Atom columns are numbered from 0 to 6. J Plot of the lattice spacing between atom columns 0,1,2,3 and 4 in (a-d). Two dot lines indicate the ideal length of 12110 (2.88 Å for Au) and 12112 (2.5 Å for Au), respectively. Scale bar:1 nm... 51

Figure 4.5 (a) Trichromatic pattern showing the rearrangement of the localized atoms during the reversible facet phase transformation between (002)/(111) ATGB and Σ11(113) STGB, viewing direction is along <110>. The solid and hollow patterns indicate different {002} or {110} planes. The yellow dash line and rhombuses indicate the

Σ11(113) STGB and its corresponding structure units, while the blue dash lines and irregular quadrilaterals indicate the stepped GB plane after the decomposition of Σ11(113) STGB and the core structures of those $111/002$ steps, respectively. (b) Selected area b to show the movement of atoms during the $(002)/(111)$ ATGB-to-Σ11(113) STGB facet phase transformation, the yellow arrows indicate the movement of atoms during the lateral motion of $111/002$ steps while the rearrangement of atoms along the blue arrows leads to the formation of Σ11(113) STGB. (c) Selected area c to show the movement of atoms leading to the backward facet phase transformation of Σ11(113) STGB into the $111/002$ steps and $(002)/(111)$ ATGB. The white solid arrows indicate the net movement of those atoms at the left side of this stepped GB, which could also be accomplished by the movement of atoms along with the blue and yellow dash arrows. The blue solid arrow indicates the movement of atoms at the right side of this stepped GB. 53

Figure 4.6 Atomistic mechanism of the backward facet transformation from the Σ11(113) STGB to the $(002)/(111)$ ATGB. (a) A long and flat Σ11(113) STGB facet, where the structure units are indicated by the rhombuses in the dark. (b) Part of the Σ11(113) STGB transformed into several $111/002$ steps connecting the $(002)/(111)$ ATGBs. (c) More $111/002$ steps were formed and GB migrated backward via the lateral motion of $111/002$ steps towards the free surface on the right. (d-f) Molecular dynamic simulation shows a similar backward facet transformation process as the experimental observation. Blue dash lines in (a, c) and dark dash lines in (e, f) represent the GB position in the last snapshot. (g) The contrast intensity line profiles extracted from (a-c) at the same area as indicated by the orange solid line in

(a). Atom columns are numbered from 0 to 6. (h) Plot of lattice spacing between atom columns 2,3,4,5 and 6 in (a-d). Some error bars are too short to show in the plot. The lattice spacing of 45 and 56 in (c) means the average lattice spacing of 45' and 5'5, respectively. Scale bar 2 nm 55

Figure 4.7 The motion behaviors of $111/002$ steps after decomposed from the Σ11 (113) STGB. (a) The steps moved rightwards first, then returned to their normal motion direction (leftwards) shortly. (b) Those steps are even transformed back into the Σ11 (113) STGB during the subsequent deformation. The blue and yellow dash lines indicate the position of the GB plane in the last snapshots and in the current state, respectively. Scale bar: 2 nm 57

Figure 4.8 Shear-driven migration of another faceted GB coupled with GB dissociation. (a) The structure of an as-fabricated Au bicrystal with a faceted GB composed of $(002)/(111)$ ATGB and near $(111)/(111)$ GB facets. The misorientation angle between the upper and bottom grains in this bicrystal is ~ 56°. Shear stress nearly parallel to the $(002)/(111)$ ATGB facets was then applied to the bottom grain, as indicated with the white arrow. (b) The $(111)/(111)$ GB facets either decomposed into several one-atomic-layer $(111)/(111)$ steps or migrated via collective motion. (c) Further migration of the entire GB via the lateral motion of $(111)/(111)$ steps and collective motion of $(111)/(111)$ GB facets along the $(002)/(111)$ ATGB facets. (d) The $(111)/(111)$ steps nucleated at the free surface and moved into the bicrystal. (e) The faceted GB dissociated into a Σ11 (113) STGB and a Σ3 (111) STGB (or twin boundary (TB)). A sub-grain region (Grain 3) was then formed. (f) The sub-grain grew via the extension of $(002)/(111)$ ATGB facets and the migration of Σ11

(113) STGB. In figures (a-f), the yellow and the red dash lines represent the current position of mixed GB and their previous position in the last frame, and the green dash lines represent the newly formed Σ3 (111) STGB. Scale bar: 2nm 58

Figure 4.9 Molecular dynamic simulations showing the GB dissociation during the migration of the faceted GB. (a-c) Sequential snapshots of simulation results showing the same process as experimental observation in Figure 4.8 of the formation and growth of a sub-grain during the migration of a faceted GB consisting of $(002)/(111)$ ATGB and $(111)/(111)$ GB facets. (d) Detailed MD simulation results showing the dynamic GB dissociation process of the $(002)/(111)$ ATGB into a Σ 11 (113) STGB and a Σ3 (111) STGB. 59

Figure 4.10 Sequential snapshots of MD simulations showing the GB migration assisted by the motion of a GB triple-junction. The GB triple-junction is the intersection point of Σ11(113) STGB, Σ3(111) STGB, and the original serrated GB consisting of $(002)/(111)$ ATGB and $111/111$ steps. Disconnections of Σ11(113) STGB and $111/111$ steps emitted from the GB triple-junction to assist GB migration (d-i). The solid dark lines indicate the current position of the GB plane while the dash dark lines mean the previous position of the GB plane in the last snapshot. 60

Figure 4.11 Transformations of $002/111$ type ATGB into Σ11 (113) STGB under different loading conditions. (a-d) A flat $(111)/(002)$ ATGB bounded by two GB junctions transformed into the Σ11 (113) STGB under the compressive loading perpendicular to the ATGB. Similarly, the ATGB-to-STGB transformation is via the nucleation and coalescence of $(002)/(111)$ steps. (e-h) $(002)/(111)$ ATGB-to- Σ11 (113) STGB

transformation started from a GB triple junction. Shear loading with an inclination angle of ~30° was applied as indicated by the white arrow. Scale bar: 2 nm............ 62

Figure 4.12 The loading-direction-dependence of Σ11 (113) STGB-to- $002/111$ ATGB transformation. (a-h) Conservative migration of Σ11 (113) STGB mediated by disconnections. Shear loading was near parallel (a-d) or had an inclination angle of ~14° (e-h) to the STGB, as indicated by the white arrow in (a,e). (i-p) STGB-to-ATGB transformation occurred when the STGB had an inclination angle of ~15° (i-l) or ~22° (m-p) with the shear loading direction. Scale bar: 2nm... 64

Figure 4.13 Plot of loading angle between STGB and applied shearing versus the experimental number. Black balls indicate the disconnection-mediated migration of STGB, while red cubes mean the STGB-to-ATGB transformation happened during the migration process.. 65

Figure 4.14 Atomistic mechanisms of the loading-direction-dependence of STGB-to-ATGB transformation. (a-h) MD simulation snapshots showing the frequent faceting/de-faceting transformation between the $002/111$ type nanofacets and the Σ11 (113) STGB. (i) Schematic illustration showing the faceting/de-faceting transformation. (j) Disconnection-mediated migration of Σ11 (113) STGB after initial faceting (i.e., nucleation and motion of disconnection dipoles). (k) STGB-to-ATGB transformation via the motion of $(111)/(002)$ steps formed after initial faceting. 66

Figure 5.1 Two distinct types of shear-coupled migration behavior of the 001200011111 MGB in Au bicrystals. (a) As-fabricated Au bicrystal containing a flat 200111 MGB at the neck region. Fast Fourier transformation (FFT) pattern and filtered Inversed FFT (IFFT) pattern are inserted to show the crystallography of the bicrystal and the

semi-coherent feature of the GB. (b-d) With the applied shear deformation (indicated by the white arrow), part of the GB migrated upwards along the [100] direction of grain 1 (denoted as G1) by transforming the 2001 plane of G1 into the 1112 plane of grain 2 (denoted as G2). (e-f) With the "same" shear loading, another type of GB migration behavior that also involves the transformation of 200 plane into 111 plane was observed. This kind of GB migration is accompanied by the formation of new grain G3 that is in a twinning relationship with G2. Scale bar: 2nm 76

Figure 5.2 Sequential HRTEM snapshots showing the atomistic processes of the two types of GB migration behavior. (a-f) Type-1 GB migration via the continuous motion of GB steps/disconnections. These disconnections are primarily at the step height of the one-atomic layer, but the formation and de-composition of disconnections with a step height of two or three atomic-layer were also observed. Inserts in (a) and (b) show the lattice deformation during GB migration, indicating the transformation from 0201 plane into 2002 plane during the process. (g-l) Type-2 GB migration that was accompanied by the formation and growth of a new grain (denoted as G3). The growth of G3 was via the migration of GBs between G1 and G3 (indicated by the blue and the yellow dash lines). Some GB disconnections with the step height of one atomic layer can be identified on the 20011113 GB. Scale bar: (a-l), 1nm; inserts in (a,b), 0.5 nm. 78

Figure 5.3 Theoretical analysis of the admissible GB disconnections of the 001200011111 MGB. (a) Comparsion of the GB disconnections mediating the two types of GB migration. (a$_1$) was cropped from Figure 5.2b while (a$_2$) is taken from Figure 5.2j and flipped horizontally for comparison. (b) Schematic illustration showing the formation

of a GB disconnection by bonding the two incompatible surface steps. The direction of the sense vector ξ is out-of-paper. (c) Schematic illustration showing the construction of a strained coherent reference state at the GB plane. The dark blue, light blue, and dark unfilled symbols indicate the unstrained (200) plane of crystal μ, the unstrained (111) plane of crystal λ, and the coherent reference state, respectively. The cubic and circle symbols indicate the atoms in different depths along the $[001]_1$ direction. (d) Coherent dichromatic pattern for the disconnection analysis of 001200011111 GB. The dark blue and light blue symbols in (d) indicate the strained crystal μ and crystal λ, separately. The yellow dash lines indicate the GB plane with a disconnection on it. 81

Figure 5.4 Topological analysis of the lattice transformation relations during GB migration. (a) Atomic models of the 001-oriented G1 and the 011-oriented G2 with the 100 plane of G1 parrallel to the 111 plane of G2. Atoms in G1 are colored purple while that in G2 are blue. (b) Schematic illustration showing the necessary localized atoms adjustment to complete the 2001-to- 1112 transformation. (c) Schematic illustration showing the two different lattice transformation relations: 0201-to-2002 and 0201-to-1112. The dash purple circles indicate the atoms arrangement of 0201 plane after the shuffling during the 2001-to- 1112 transformation. The purple arrows in (b) and (c) indicate the movement of atoms during the transformations. The dash orange arrow and the green arrow in (c) indicate the shear displacement contributed by the screw component of disconnection and the atoms shuffling to accompany the transformation, separately. 83

Figure 5.5 MD results of GB migration following the 0201 -to- 1112 type lattice transformation. (a, b) Au bicrystal before and after the shear deformation. Shear displacement was applied on the top fixed end along the [010]$_1$ direction. (c-f, g-j) Sequential snapshots showing the GB structures at different depths along the [010]1 direction . The sliced positions are indicated by the dashed lines in k. Selected atom columns on 0201 atomic planes were colored orange to show the lattice transformation. New grains formed after twinning are denoted as G3 and G4, separately. The purple arrows indicate the motion directions of GB disconnections. (k-n) Top views of a thin (indicated by the red arrows in c and g) atomic layer showing the atomic plane transformation during GB migration in c-f and g-h. The curved lines represent the disconnection lines between different grains. Green atoms represent the bulk face-centered cubic atoms while white ones indicate boundary atoms. 86

Figure 5.6 MD results of GB migration following the 2002-to-0201 lattice transformation. (a, b) Au bicrystal before and after the shear deformation. Shear displacement was applied on the top fixed end along the x-axis of the bicrystal, i.e., [011]1 direction. (c-f) Sequential snapshots showing the 2002 -to- 0201 lattice plane transformation during the GB migration. The sliced positions are indicated by the dashed lines in g. Atoms on 2002 atomic planes are selectively colored in dark green to trace the lattice transformation. The purple arrows indicate the motion directions of GB disconnections. (g-j) Top views of a thin slice perpendicular to the z-axis showing the 1112-to-2001 atomic plane transformation during GB migration in c-f. The position of the thin slice is indicated by the red arrows in c. 88

Figure 5.7 Geometrical analysis of the concurrent GB migration and GB sliding under shear deformation. (a, b) Schematics of bicrystals with a flat 001200011111 GB (a) and with the GB plane reoriented by a certain inclination angle α (b). The lengths of the atomic planes matching at the GB change with the reorientation of GB. (b) Plot of the length ratio between 2001 and 1112 planes that match at the reoriented GB plane. (d-i) Sequential HRTEM images showing the shear deformation of the Au bicrystal was dominated by GB migration after the GB plane reoriented to α = 23°. (j-m) MD simulation results showing the migration of a GB with α = 19° was accommodated by the coordinate migration of 001200011111 GB facets. Scale bar. (d-i) 5 nm........ 93

Figure 5.8 A typical example of GB migration accommodated by the GB triple-juction. (a) as-fabricate sample with a mixed tilt twist GB_{12} between 001-oriented and 011-oriented G2, and a mixed tilt-twist GB_{13} between G1 and 011-G3, and a twin boundary between G2 and G3. The misorientation relation between G1 and G2 is the same as the 001200011111 GB, but differ at the GB plane orientation. (b) GB_{12} and G_{13} migrated downwards under the leftwards shear loading. The Shear -coupling factor of G_{12} is measured to be ~0.514±0.014. (c) Schematic illustration showing the lattice transformation relation and the calculation of corresponding theoretical value of the shear-coupling factor of G_{12}, which is $\beta \approx tan41° - tan18° = 0.544$. Scale bar: 1 nm.. 97

Figure 5.9 Twinning-assisted transition of lattice transformation relations during the GB migration. (a) As-fabricated Au bicrystal with a similar orientation relation to that in Figure 1. The GB plane has an inclination angle of ~20° with the 001200011111 GB plane. (b-d) under the leftward shear loading, GB migration changed from following

the 0201 -to- 1112 type transformation relation into the 0201 -to- 2003transformation relation, assited by the twinning and formation of a new grain 3. (f-i) the reversed GB migration under the rightwards shear loading. GB migration changed from following the 2003-to- 0201 transformation relation into the 1112-to- 0201 transformation relation, assisted by the shrinkage and disappearance of G3. Scale bar: 2 nm. 98

Figure 6.1 Formation process of a 011-tilt 311111 GB in an Au nanowire upon bending deformation. (a) Pristine Au nanocrystal. (b, c) Nucleation and accumulation of GNDs to accommodate lattice rotation. (d) Alignment of GNDs to form a curved GB. (e, f) Additional GNDs formed during subsequent bending deformation. (g, f) The GNDs and the curved GB collapsed to form the (311)/(111) GB. Inserts in the left-bottom of (a-i) and the right-top of (b) are corresponding fast Fourier transformation (FFTs) patterns and the schematic of Thompson tetrahedron, respectively. 105

Figure 6.2 Annihilation process of a 311111 GB in an Au nanowire upon reversed bending deformation. (a, b) Lattice rotation mediated by GB structure reconstruction until the GB transformed into a (944)/(111) GB (c) GB dissociation to form two chevron regions. (d) Further GB annihilation by emission of SFs, twinning, and GB structure reconstruction into GNDs. (e) The elimination of the SFs and GNDs. Residual SFs on inclined {111} plane may still exist, as shown in the enlarged view in the insert. (f) Fully annihilation of the GB. Inserts in the left-bottom of (a-f) are corresponding fast Fourier transformation (FFTs) patterns of the nanowire. 108

Figure 6.3 HRTEM images showing the GB structure reconstruction and dislocation activity at the incipient stage of deformation. (a-c) GB structure reconstruction during the

deformation, as reflected by the variance of GB structure. Residual dislocation in (a) also interacted with the GB. (d-f) Continuous GB structure reconstruction accompanied by the release of lattice distortion on the GB and a dislocation event occurred near the GB and the free surface. Inserts in (d-f) are enlarged views to show the occurrence of the dislocation event causing the disappearance of the surface step. 110

Figure 6.4 HRTEM images showing the synergic mechanisms accommodating GB annihilation. (a, b) Nucleation of twin and SF from the GB, accompanied by the shrinkage of extended GB region. (c, d) Additional SFs nucleated from the GB and GB structure reconstructed into GNDs. (e, f) SFs eliminated during subsequent deformation, along with the decreasing quantity of GNDs. Inserts in (c, d) were enlarged from the lattice distortion region as enclosed by the blue dashed circle.. 111

Figure 6.5 MD simulation of 311111 GB annihilation in an Au nanowire upon bending deformation. (a-c) Typical snapshots showing the GB annihilation process. (d-h) Snapshots showing the GB structure reconstruction during GB annihilation. (i-m) Snapshots showing the twinning and detwinning process during GB annihilation. (n-p) Snapshots showing the nucleation, interaction, and elimination of SFs during GB annihilation. Note that FCC atoms (in green) in (n-p) were not shown and the sample was slightly tilt to visualize the SFs. Inserts in (n-p) show the crystal structure before modification. 113

Figure 8.1 Bending-induced formation of a ‘thick’ GB region consisted of BCT Au in FCC Au nanocrystal. (a-d) Sequential HRTEM images showing the formation process. (e)

Schematic of the atomic structure of FCC Au in grain 1 (G1) and grain 2 (G2) and BCT Au in GB. (f-h) Enlarged views of selected GB regions in (b-d)...................... 122

Preface

I would like to extend my acknowledgment to all those who have helped and supported me during my Ph.D. study. First and foremost, I would like to express my deepest gratitude to my advisors Dr. Guofeng Wang and Dr. Scott Mao for their patient guidance and constant support. Their professional instructions and encouragement inspired me to complete my Ph.D. study.

My sincere acknowledge also goes to my collaborators: Dr. Chuang Deng and Dr. Jianwei Xiao at the University of Manitoba, for their brilliant MD simulation work and insightful discussion on revealing the dynamic grain boundary structural transformation during migration; Dr. Susheng Tan at the University of Pittsburgh, for his instruction and help on TEM characterization. I also would like to express my sincere gratitude to my committee members: Dr. Patrick Smolinski, Dr. Qihan Liu, and Dr. Feng Xiong, for their encouragement, advice, and insightful comments on my dissertation. I also thank my group member: Li Zhong, Yang He, Xiang Wang, Sixue Zheng, Boyang Li, and Ying Fang, for their helpful discussion and support of my Ph.D. study.

Finally, from the bottom of my heart, I would like to thank my family, especially my beloved wife Miao Ou, and my son Miles Fang. Their sacrifice, love, support, and smile have inspired and will always inspire me to keep the faith and move forwards. This dissertation is dedicated to them!

1.0 Introduction

Grain boundary (GB), i.e., the region separating two adjoining grains with the same crystal structure but of different orientations, is known as the ubiquitous interfacial structure in polycrystalline materials. GBs have been demonstrated to greatly influence the mechanical[1], electrical[2, 3], and magnetic properties[4, 5] of polycrystalline materials, and thus have received extensive attention from the community of material researchers for a long time. Unlike other lattice defects such as vacancy, dislocation, and twin boundary which usually have limited types, there is a broad spectrum of types of GBs due to the complexity of GB structure. The complexity of GB structure comes from which at least five macroscopic parameters, i.e., 3 for the orientation relationship and 2 for the grain boundary plane orientation, are needed to unambiguously define a GB[6]. From the perspective of crystallographic description, GBs can be classified into three types: tilt GB, twist GB, and general tilt-twist GB. As shown in Figures 1.1a and 1.1b, GBs are referred to as tilt GBs if the GB plane is parallel to the rotation axis of adjoining two grains. More specifically, the GB is called symmetrical tilt GB (STGB) if the two grains are in mirror symmetry to the GB plane (Figure 1.1a). While it is called asymmetrical tilt GB (ATGB) if the GB plane has an inclination angle deviated from the ideal position of STGB (Figure 1.1b). In comparison, twist GB (TWGB) is formed when the GB plane is perpendicular to the rotation axis (Figure 1.1d). All other GBs with the GB plane having an arbitrary angle with the rotation axis are referred to as general mixed tilt-twist GBs (Figure 1.1c). Based on the atomic structure of GBs, GBs can also be classified into two types: low-angle GB (LAGB) and high-angle GB (HAGB). The critical misorientation angle between LAGB and HAGB is normally referred to as ~15°, only below which the GB can be described by the lattice dislocation model.

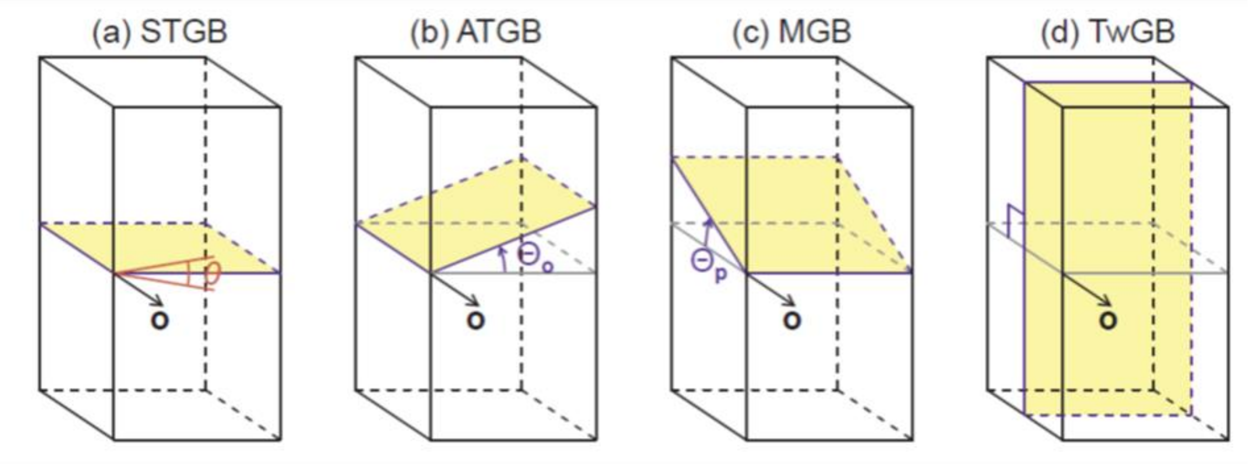

Figure 1.1 Schematic of GB classification based on the crystallographic description.(a) the symmetrical tilt GB (STGB), (b) the asymmetrical tilt GB (ATGB), (c) the general mixed tilt-twist GB, and (d) the pure twist GB (TwGB).[7]

Understanding the influence of GBs on the mechanical properties of polycrystalline materials is critical for the development of high-performance materials with a combination of high strength and excellent ductility. On the one hand, it is known that GBs could act as barriers to the motion of lattice dislocations, leading to the strengthening of materials[8]. On the other hand, GBs could be the source of weakness, resulting in intergranular fracture and leading to the early failure of materials[9]. Moreover, when the crystal size comes down to below a critical value, e.g., 10 nm, GB itself can contribute to the plastic deformation of polycrystalline materials[10, 11]. General GB-mediated deformation mechanisms include GB sliding[12-14], grain rotation[15, 16], and GB migration[17]. Among these, the deformation-induced GB migration is highly related to the grain growth and plastic instability during the room-temperature deformation of nanocrystalline materials[18, 19], and is chosen as the topic of this dissertation study.

Numerous investigations, including experimental observation, theoretical models, and computational simulations, have been conducted to uncover the mechanisms of deformation-induced GB migration in the past decades. However, due to the existence of technical bottleneck, previous experimental studies mainly focused on the macro- or micro-scale GB migration behaviors. Knowledge of the GB migration behaviors at the atomic-scale relied largely on the theoretical models and atomistic simulations, which shall need verification from the experimental observations. Moreover, even for the atomistic simulations, most studies focus on the migration of flat and special GBs such as the STGBs, much less is known about the migration behaviors and atomistic mechanisms of the faceted GBs, which is the common morphology of ATGBs in the real case, and the general mixed tilt-twist GBs.

In addition, the deformation-induced formation of GBs mediates the intensive grain refinement during the severe plastic deformation of coarse-grained polycrystalline materials. The grain refinement process involves the formation of LAGB first and later the LAGB-to-HAGB transformation. Recent in-situ TEM studies revealed the fully reversible formation of LAGB via the motion of GB dislocation. However, the LAGB-to-HAGB transformation and the annihilation behavior of the as-formed HAGB have never been explored.

This dissertation is organized as follows. In Chapter 2, previous studies, including experimental observation, theoretical models, and computational simulations on the shear-coupled GB migration, as well as the deformation-induced formation and annihilation of GBs will be reviewed. The motivation and objective of this dissertation will be proposed accordingly.

In Chapter 3, materials, experimental procedures including in-situ TEM experimental configuration, fabrication of nano bi-crystals with desirable GB structures, and GB plane identification, as well as simulation methods are introduced in detail.

Chapter 4 reports the dynamic GB structural transformation arising from reversible facet transformation and GB dissociation during the shear-coupled migration of <110>-tilt faceted ATGBs. It was found that the types of steps/disconnections mediating the migration of GB facets determine which pathway the GB structural transformation follows. Moreover, the loading-dependence of GB facet transformation and the roles of GB junctions in accommodating GB migration and structural transformation were also analyzed.

Chapter 5 focuses on the atomic-scale migration behavior of a typical MGB, i.e., $\langle 001\rangle\{200\}/\langle 0\bar{1}1\rangle\{\bar{1}11\}$ GB. Two distinct migration patterns showing the opposite signs of shear-coupling factor were observed and further revealed to be mediated by the motion of GB disconnections with different crystallographic parameters and exhibit different lattice correspondence relations. MD simulation results confirm that the two distinct migration patterns could be activated under different stress/strain states. Moreover, excess GB sliding and GB plane reorientation were found to accommodate the GB migration in both experiments and simulations, which is likely due to the necessity of establishing a point-to-point lattice correspondence during GB migration.

In Chapter 6, the dynamic formation and annihilation process of a $(311)/(111)$ HAGB upon reciprocating bending deformation of a gold nanocrystal is studied. It is found that HAGB formation underwent the process of accumulation, alignment, and exhaustion of geometrically necessary dislocations. In comparison, HAGB annihilation was accomplished by the synergic operation of GB structure reconstruction, emission of partial and full dislocations, and twinning. Such synergic mechanisms were further confirmed by molecular dynamics simulation.

At last, the conclusions of this dissertation are summarised in Chapter 7 and future research directions are discussed in Chapter 8.

2.0 Background

In this section, previous research, including experimental investigation, theoretical models, and computational simulations, on deformation-induced GB migration will be reviewed. Previous studies on the deformation-induced formation and annihilation of GBs will also be discussed.

2.1 Experimental Investigation of Deformation-induced GB Migration

As early as the 1950s, Parker et al. [20] reported the first experimental observation on deformation-induced GB migrations. They fabricated zinc bicrystal samples with LAGBs in different misorientation angles and investigated the dynamic deformation behavior of these GBs using optical microscope. The movement of these LAGBs under mechanical loading were observed and found to be reversible when shifting the loading directions[20]. Since then, the methodology of fabricating and using bicrystal samples to investigate the deformation-induced GB migration behaviors were widely adopted, and numerous studies were reported[21-30]. For instance, Fukutomi et al.[21] reported that <112>, <110>, and <100> STGBs with misorientation angles of 3°-17° in aluminum bicrystals all migrated under the external stress at high temperatures, and proposed an equation to quantify the relation between GB migration velocity, applied stress, and temperature. Winning et al.[22-24] did a series of studies on the deformation-induced migration of <112>, <111>, and <100> STGBs in a wide range of misorientation angles, i.e., 3-35°, in aluminum bicrystals at elevated temperatures. They found that there exist step changes of the activation enthalpy for GB migration with the increase of GB misorientation angles, indicating the sharp transitions between LAGBs and HAGBs. The transition angle for <112> and <111> STGBs were measured to be 13.6°[22, 23], while 8.6° for <100> STGBs[24]. Molodov et. al[26, 27] investigated the deformation-induced migration of <100> STGBs across the entire misorientation range and found that GBs with misorientation angles below 31° and above 36° migrated in opposite directions under the same applied external stress. In addition, Gorkaya et al.[28] studied the deformation-induced migration behaviors of a planar 18.2° <100> non-tilt GB with a 20° twist component at elevated temperatures, and they reported that concurrent GB migration and grain rotation occurred during the tensile deformation of the bicrystal.

Although these bicrystal studies helped us to understand the migration behaviors and kinetics of some special flat STGBs (and a mixed GB) at the macro-scale, there are two main limitations in these studies: 1. They were conducted at elevated temperatures to ensure the measurable GB mobility, which makes it hard to differentiate the mechanical effect and the thermal effect; 2. The bicrystal samples did not receive constraints from neighboring grains that commonly exist in polycrystalline materials. Thus, understanding the GB migration behaviors in polycrystals at room temperature remains to be fundamentally important. It was noted that nanocrystalline metals could occur in room-temperature grain growth during the plastic deformation, which was suspected to be caused by the stress-driven GB migration [31]. To verify this conjecture, Rupert et al[32] introduced the spatial variation of stress and strain states in nanocrystalline Al thin films by using the special sample geometrics (i.e., introducing holes at horizontal or angled orientations on the thin film), and they discovered that grain growth was largest at the region with the highest stresses and occurred faster at regions where the distortional energy is large. In addition, Sharon et al[17] reported a similar stress-driven grain growth phenomenon in nanocrystalline Pt thin films. Having clarified that stress-driven GB migration led to the room-temperature microstructural evolution in nanocrystalline material, understanding the GB migration dynamics at the micro-scale was the other remaining goal to achieve. And, it became possible with the development of in-situ transmission electron microscopy (TEM) methods.

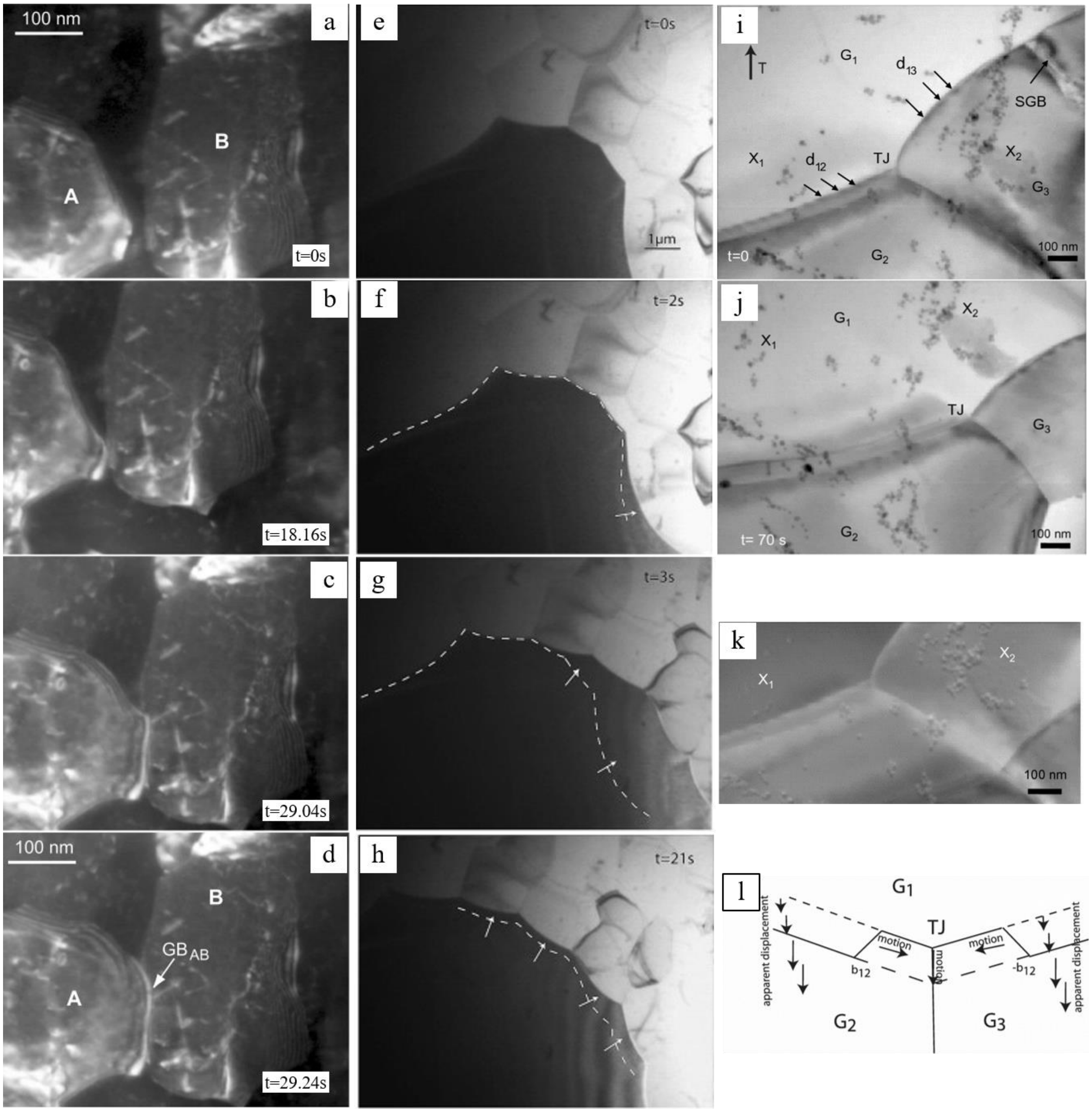
a
100 nm
B
A
t=0s
e
t=0s
1μm
i
T
G1
d13
SGB
X1
d12
TJ
X2
G3
t=0
G2
100 nm
b
t=18.16s
f
t=2s
j
G1
X1
X2
TJ
G3
t= 70 s
G2
100 nm
c
t=29.04s
g
t=3s
k
X1
X2
100 nm
d
100 nm
B
GBAB
A
t=29.24s
h
t=21s
l
G1
TJ
apparent displacement
motion
b12
motion
motion
-b12
apparent displacement
G2
G3

Figure 2.1 In-situ TEM observations of stress-driven/assisted GB migration in nanocrystalline Al. (a-d) Sequential dark-field TEM images showing the growth of grain A towards grain B by fast GB migration at room temperature [33]. (e-h) Sequential bright-field TEM images showing the grain growth via the migration of faceted GBs under applied stress at 350 °C [34]. (i, j) Bright-field TEM images of the same region containing three joint GBs before (i)

and after (j) the stress-induced GB migration, respectively. (k) The superimposed image of (i) and (j). (l) Schematic showing the mechanism of GB triple junction on accommodating the GB migration [35].

Figure 2.1 shows the in-situ TEM observations of stress-driven or stress-assisted GB migration in nanocrystalline Al samples [33-35]. The sequential dark-field images in Figure 2.1a-d was captured at the crack tip of deforming Al thin films at room temperature. The initially isolated two grains (Figure 2.1a) [33], i.e., grains A and B, were found to be connected to form a GB_{AB} after the straining (Figure 2.1d), which was enabled by the fast motion of GB at the lower right of grain A towards the grain B (Figure 2.1a-d). Figure 2.1e-h presents another case of fast grain growth observed in ultrafine grain Al under applied stress at 350 °C, which clearly shows that the stress-assisted migration of the faceted GB (indicated by the white dash lines) led to the microstructural evolution [34]. Moreover, the role of the GB triple junction in accommodating the GB migration was also reported [35]. Figure 2.1i and Figure 2.1j are the bright-field TEM images that were captured at the same region before and after GB migration, separately. By superimposing these two images (Figure 2.1k), it was found that GBs between G1 and G2/G3 (GB_{12} and GB_{13}) migrated, while in contrast, the GB between G2 and G3 (GB_{23}) kept stationary. The underlying mechanism was proposed as shown in the schematic in Figure 2.1l that dislocations moved in opposite directions along GB_{12} and GB_{13} and finally merged at the GB triple junctions. It needs to mention that the above in-situ TEM studies were conducted at either conventional bright-field observation or dark-field observation, and the GB migration in these studies is fast, which both made revealing the GB migration behavior at the atomic scale impossible.

In comparison, Wang et al [36] reported the in-situ high-resolution TEM (HRTEM) observation of the stress-induced GB migration in nanocrystalline Au. As shown in Figures 2.2a and 2.2b, the in-situ observation was targeted at the region containing an 18.52° <110> tilt LAGB, which ensured the acquirement of HRTEM images. The enlarged view of this GB revealed that it consisted of an array of GB dislocations (Figure 2.2d). After straining the sample, this GB was found to migrate (Figure 2.2c), accompanied by the decease of GB misorientation angle into 7.98°, which indicated the concurrent GB migration and grain rotation during this process, and was attributed to the climb and glide of GB dislocations (Figure 2.2e). In addition, Zhu et al. did a series of in-situ HRTEM studies on the disconnection-mediated GB migration[37], the controllable reversible migration of LAGBs[38], the GB migration subject to defect interaction[39], the dynamic adjustment of GB mobility assisted by twinning[40], and the deformation of LAGBs governed by the inclination angle[41]. The work by Zhu et al justifies the powerful ability of in-situ HRTEM studies to directly reveal the dynamic GB migration process at the atomic scale.

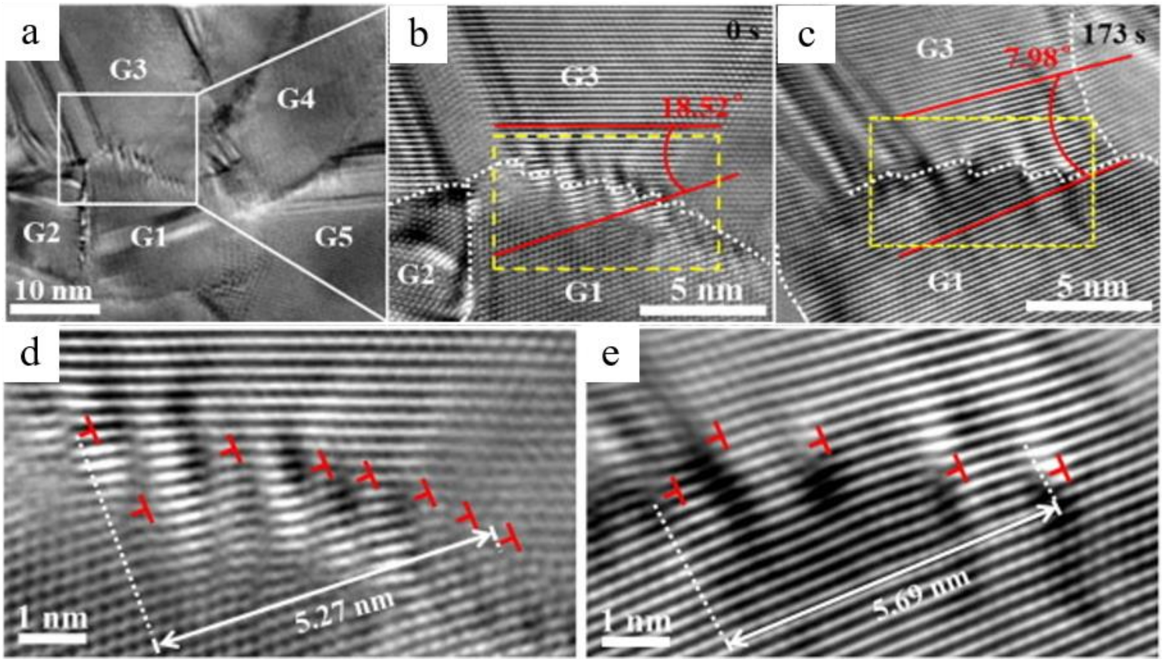

Figure 2.2 Concurrent GB migration and grain rotation during the deformation of nanocrystalline Au [36]. (a) Low-magnification TEM image of the sample. (b, c) HRTEM images of the GB network before (b) and after (c) the deformation. (d, e) Enlarged observation on the GB structure in the regions enclosed by the yellow dash boxes in (b) and (c), showing that the GB was consist of an array of GB dislocations.

2.2 Theoretical Models for Shear-coupled GB Migration

In this section, theoretical models, including CSL/DSC lattice model, Cahn model, SMIG model, and the unified disconnection model that were used or proposed to interpret the shear-coupled GB migration behaviors will be reviewed.

2.2.1 CSL/DSC lattice model

The CSL/DSC lattice model is a well-recognized mode for describing the equilibrium structure of GBs in cubic crystals [42-45]. CSL means the coincidence-site lattice, while DSC denotes displacement shift complete. To construct the coincidence-site lattice, one should first rotate a lattice around an axis for certain angles to make it partial self-coincidence. Then, the new lattice, with larger cell dimensions, constructed by the common sites between the original lattice and the rotated lattice stands for the coincidence-site lattice. Figure 2.3a shows an example of constructing a coincidence-site lattice in a rectangular lattice, the rotation of the lattice point (x, -y) around the origin by an angle of ω into the other lattice point (x, y) will construct a coincidence-site lattice that consists of the row which (x, -y) lies and the other row perpendicular to it [45]. It was noted that the coincidence-site lattice always has a larger unit cell than the origin lattice. Therefore, a quantity Σ, called the reciprocal coincidence site density, was proposed to characterize the coincidence-site lattice. The value of Σ equals the ratio of the area of the CSL unit cell over that of the original unit cell [43]. Figure 2.3b presents a diagram showing the coincidence-site lattices with different Σ values for [111] rotations. The details on the calculation of the Σ values can be found in the reference [45]. It needs to mention that for a given value of Σ (e.g., 3, 7, or

21), the coincidence-site lattice is not unique. Therefore, the rotation angle must be given to ambiguously define a coincidence-site lattice.

The CSL model reflects the rotational symmetry between two grains, while the DSC lattice implies the translational symmetry of the coincidence-site lattice. Figure 2.3c shows a dichromatic pattern (obtained by superimposing the rotated lattice with the original lattice) that includes the Σ5 coincidence-site lattice of a bi-crystal for 36.9° <100> rotation [7]. The coincidence sites are colored gray, and a CSL unit cell is shadowed yellow which has an area five times larger than the original unit cell. It needs to mention that displacing the entire black lattice along the vectors colored green would only shift the dichromatic pattern but not change it. In other words, these displacements would conserve the dichromatic pattern. Therefore, the new lattice constructed by these green vectors (shadowed in green) is called the displacement shift complete (DSC) lattice. Dislocations carrying these DSC vectors that glide on the GB plane would lead to the motion of GB, and thus are often called as DSC dislocations[35, 46] or secondary GB dislocations [47-49].

The CSL/DSC model has been successfully applied in practice to interpret stress-driven GB migration behaviors in both experiments [34, 35, 47, 48] and simulations [46, 50, 51]. For example, Mompiou et al.[34] applied this model to explain the observed shear-coupled migration of a GB close to the Σ13a $[0\bar{1}0]$ pure tilt GB in Al. As shown in Figure 2.3d, there are two types of DSC dislocations (i.e., $\mathbf{b}_1$ or $\mathbf{b}_2$) that can lead to the normal motion of GB from white lattice towards dark lattice, which would generate the theoretical shear-coupling factor ($\beta = b/h$) of 40% or 25%, separately. The theoretical of 25% is quite close to the experimental measured values (16-23%), indicating that $\mathbf{b}_2$ type DSC dislocations mediated the GB migration. Wan et al.[50, 51] investigated the various structure evolution behaviors of Σ9 $\langle 110\rangle\{221\}$ STGB[51], Σ3 $\langle\bar{1}10\rangle$-tilt $(\bar{1}\bar{1}5)/(111)$ ATGB[50], and Σ9 $\langle\bar{1}10\rangle$-tilt $(115)/(111)$ ATGB [50] under different shear loading conditions (i.e., shear directions) in fcc metals using molecular dynamic simulations. The CSL/DSC model was applied to describe the observed GB sliding-migration coupled motion in these GBs.

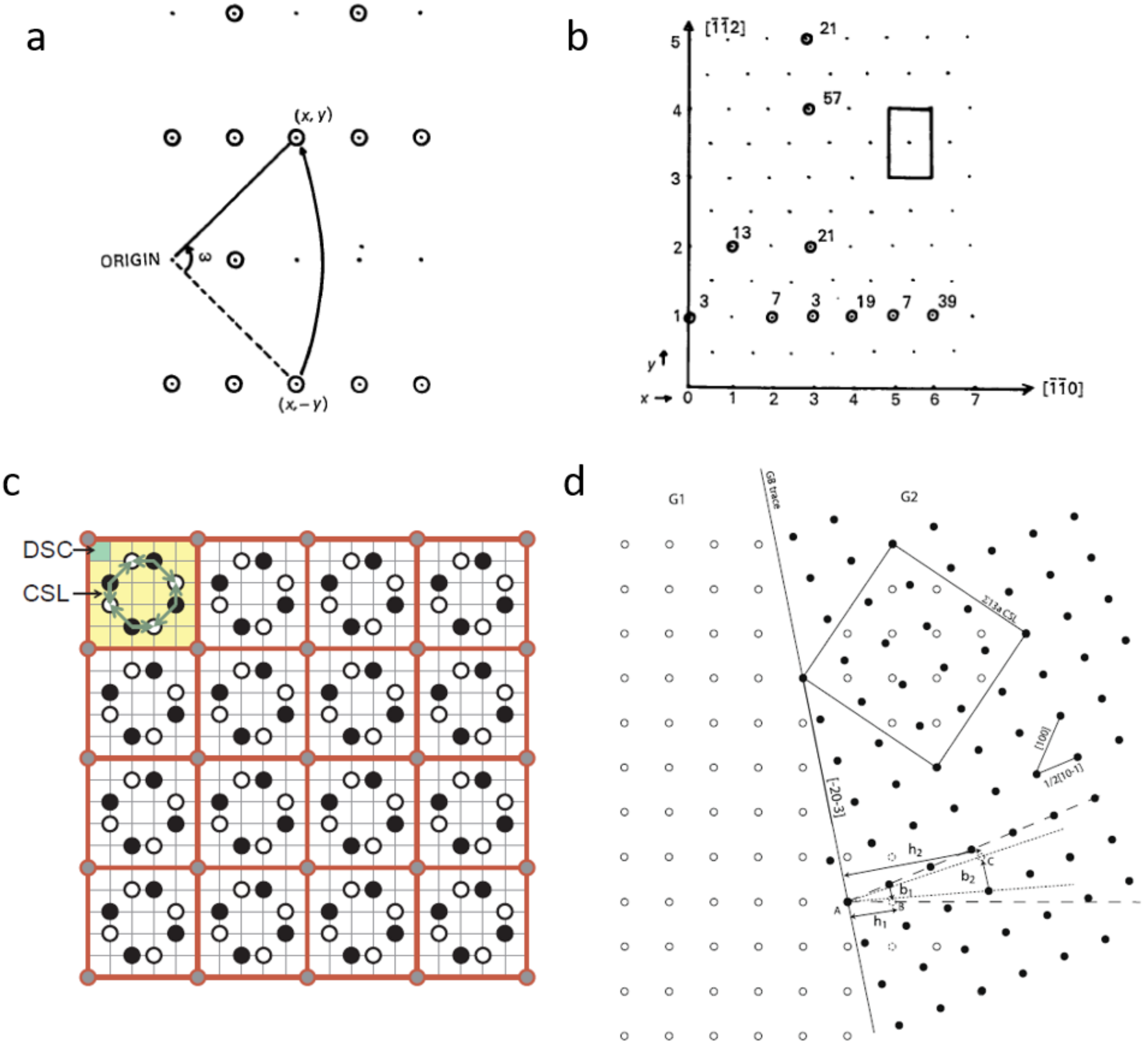
a
(x, y)
ORIGIN
ω
(x, −y)
b
[1̄1̄2]
5
4
3
2
1
21
57
13
21
3
7
3
19
7
39
y
x
0
1
2
3
4
5
6
7
[1̄1̄0]
c
DSC
CSL
d
G1
G2
GB trace
Σ13a CSL
[100]
1/2[10-1]
[-20-3]
h₂
b₁
b₂
h₁
A
B
C

Figure 2.3 Diagrams illustrating the CSL/DSC lattice model. (a) Example of constructing a coincidence-site lattice in an originally rectangular lattice [45]. (b) Coincidence-site lattices with different Σ values for [111] rotations in cubic crystals [45]. (c) Coincidence-site lattice and displacement shift complete (DSC) lattice in a Σ5 bi-crystal for 36.9° <100> rotation [7]. Arrows in green indicate the DSC vectors. (d) Admission DSC dislocations that can lead to the normal migration of a Σ13a $[\mathbf{0\bar{1}0}]$ pure tilt GB[34].

2.2.2 Cahn model

The series work by Cahn et al.[52-54] proposed and confirmed that the normal GB motion is always coupled to the shear deformation applied to the GB. Using molecular dynamic simulations, they investigated the shear-coupled GB migration of [001] STGBs in copper (Cu) and revealed the misorientation dependence of the shear-coupling factor β of these STGBs [53]. A geometric model, called the Cahn model by later, was proposed to account for the sudden switch of positive shear-coupling factors into negative ones at a tilt angle of ~35°. The Cahn model was developed upon the classical Read and Shockley model on the motion of LAGBs [55]. The main assumption behind it is that GBs are constructed by arrays of GB dislocation, and the motion of GBs is assisted by the glide of these GB dislocations. Figure 2.4a-c shows the schematic illustration of how the glide of GB dislocations accommodated the shear-coupled GB migration [53]. Firstly, assuming there is a block of material, OABC, which contains an initial GB consisting of an array of GB dislocations (Figure 2.4a). The sides of this block (e.g., CO, and BA) are parallel to the slip planes of these GB dislocations. Next, apply shear deformation on this block along the AB direction with the origin O fixed. This shear deformation would be accommodated by the glide of GB dislocations, which would not change the lattice orientation of the block OABC but lead to rotation of the reference atomic plane (indicated by the dotted lines) by an angle of ψ (Figure 2.4b). However, this operation would generate a void area, OAA'. To maintain the material contiguity, the rotation of the entire block around the origin O by an angle of θ is needed (Figure 2.4c). Then, the initial GB would migrate to the position of the final GB (i.e., B'C').

Accordingly, Cahn et al proposed two modes of shear-coupling in [001] STGBs[53]. One is the <100> mode where the Burgers vectors of GB dislocation are parallel to [100] direction of the lattice, and the other is the <110> model which the governing GB dislocations have the direction of Burgers vectors parallel to the [110] direction. Based on the Frank equation [56, 57], the shear-coupling factors of these two modes are derived as $\beta_{\langle 100\rangle} = 2\tan(\theta/2)$and $\beta_{\langle 110\rangle} = -2\tan((\pi/2-\theta)/2)$, separately. The shear-coupling factors predicted by the model are plotted in Figure 2.4d, which are in good agreement with the simulation results (indicated by back dots). Moreover, experimental measurement of shear-coupling factors of <100> STGBs in Al [27] also shows a good agreement with the prediction of the Cahn model.

2.2.3 Shear migration geometrical (SMIG) model

The limitation that lies behind the Cahn model is that it is derived based on the GB dislocation model, which would lose the physical meaning when the GB misorientation angle is high (e.g., larger than 15°, the core structure of dislocations would be overlapped). In addition, the experimentally measured shear-coupling factor of GBs in polycrystalline materials deviating from the prediction of the Cahn model was also reported [34]. Therefore, another geometrical model called the shear migration geometrical (SMIG) model, was alternatively proposed to explain the shear-coupled GB migration behaviors [58-60]. The main idea of the SMIG model is to find out the combinations of shear and rotation operations that can transform one lattice into another lattice with a different orientation. It is a purely geometrical model without considering the GB plane orientations. Moreover, the choices of lattice supercell (i.e., parallelograms enclosing the same number of atoms) would largely affect the values of shear and rotation for the transformation. Figure 2.4e presents an example of determining different parallelograms with the same area in a fcc {011} plane [58]. All these parallelograms can be transformed into each other by shearing them with different combinations of vectors **p** and **q**. The abundant choices of parallelograms lead to a broad spectrum of predicted shear-coupling factors. As shown in Figure 2.4f, the shear-coupling factors of <100> STGBs predicted by the SMIG model are plotted in dark spots, which clearly shows a quite dense but discrete distribution. The predicted values based on the Cahn model are also plotted in this diagram, as indicated by the green and blue curves, showing that the SMIG model includes the predictions based on the Cahn model. More importantly, the experimentally measured shear-coupling factor (circles in red) [27] that slightly deviated from the curves of the Cahn model also falls into good agreement with the prediction of the SMIG model. All these justify the validation of SMIG in describing the GB-mediated plasticity in polycrystals.

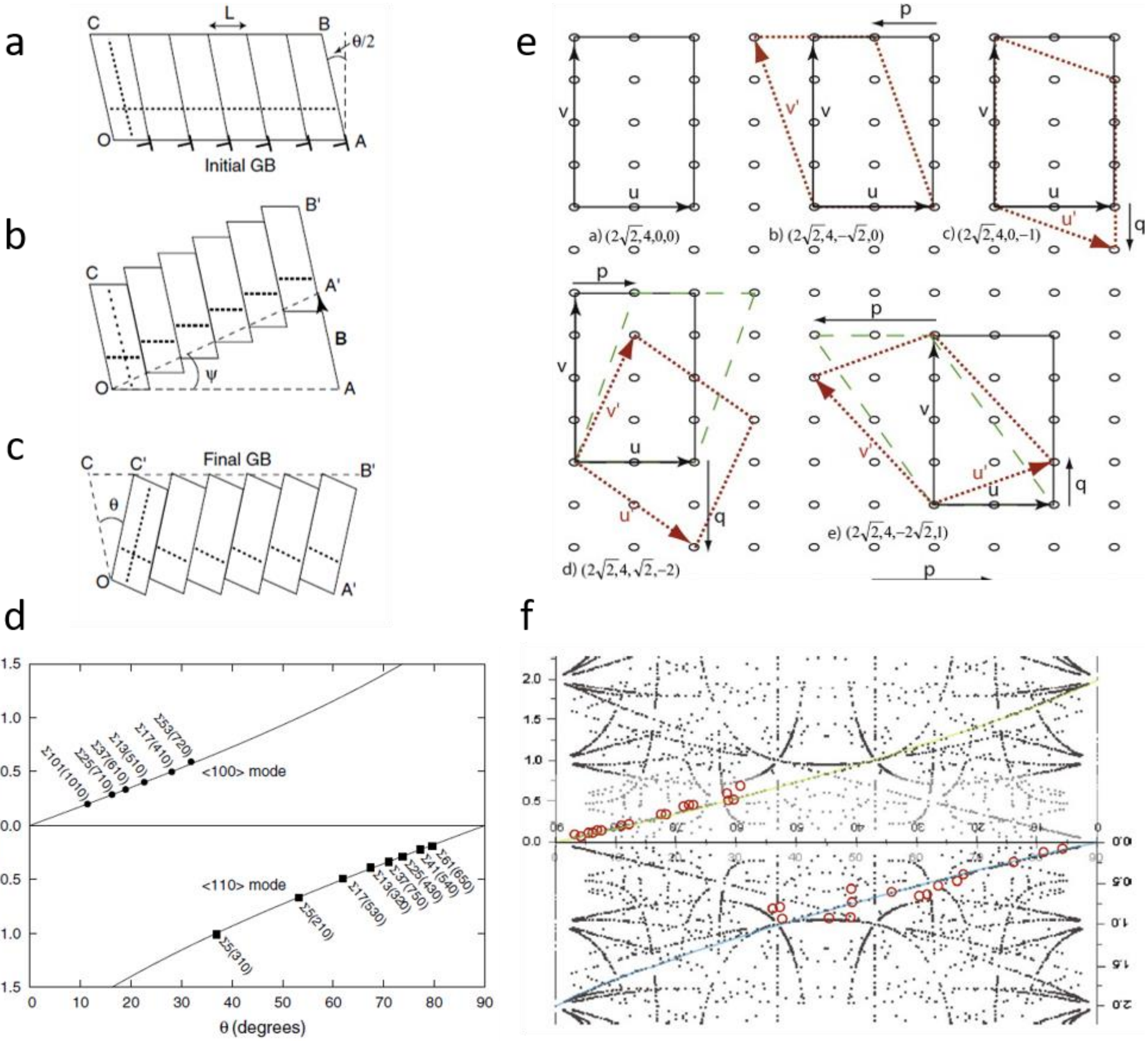
a
C
L
B
θ/2
O
A
Initial GB
b
B'
C
A'
B
ψ
O
A
c
C
C'
Final GB
B'
θ
O
A'
d
e
p
v
u
v'
u'
q
a) (2√2,4,0,0)
b) (2√2,4,−√2,0)
c) (2√2,4,0,−1)
d) (2√2,4,√2,−2)
e) (2√2,4,−2√2,1)
f
Coupling factor
θ (degrees)
<100> mode
<110> mode
Σ101(1010)
Σ25(710)
Σ37(610)
Σ13(510)
Σ17(410)
Σ53(720)
Σ5(310)
Σ5(210)
Σ17(530)
Σ13(320)
Σ37(750)
Σ25(430)
Σ41(540)
Σ61(650)
1.5
1.0
0.5
0.0
-0.5
-1.0
-1.5
0
10
20
30
40
50
60
70
80
90
2.0
1.5
1.0
0.5
0.0

Figure 2.4 Comparison of Cahn model and shear migration geometrical (SMIG) model. (a-c) The coupled glide of GB dislocations and grain rotation lead to the GB migration.[53] (d) Plots of predicted shear-coupling factors versus the misorientaion angle of <100>tilt STGBs based on Cahn model. Shear-coupling factors of typical CSL GBs obtained by molecular dynamic simulations are also given for comparsion[53]. (e) Schematic showing the transformations between parallelograms with the same area[58]. (f) Plots of predicted shear-coupling factors versus the misorientaion angle of <100>tilt STGBs based on SMIG model[59].

2.2.4 The unified GB disconnection model

Although the SMIG model has been successfully applied to explain the abnormal shear-coupling factors of GB migration measured in experiments, it remains enduring doubts from the community. The major doubt is that it is a purely geometrical model without physical meaning. Consequently, the broad spectrum of shear-coupling factors for a given bi-crystal system predicted by the SMIG includes many circumstances that are unlikely to happen physically. This limitation also makes the SMIG model can only be used to interpret the already observed GB migration behaviors in experiments, but not to predict the favorable shear-coupling model for a given GB. Very recently, the GB disconnection model has been regarded as the unified model to describe GB kinetics [7]. The concept of disconnection can be traced back to the 1970s, Bollmann[61], Ashby[62], and Hirth and Balluffi[63] developed the geometrical theory to describe the defects residing on crystalline interfaces. Compared to the conventional lattice line defects (i.e., dislocations), GB disconnections are line defects with both the dislocation feature (i.e., carrying the Burgers vector) and the step feature, and move only along GBs [64]. The formation of GB disconnection can be understood by merging two crystals with incompatible surface steps[64]. Figure 2.5a shows the schematic of constructing a GB disconnection by merging crystal λ with crystal μ[65]. The two incompatible crystal surface steps need to be bounded together to maintain the continuity of the material. The operation generates a line defect carrying the Burgers vector **b** on the interface, which is called the GB disconnection[65].

There are two methods to determine the Burgers vector of GB disconnection. One is a posteriori method by constructing Burgers circuits around a given GB disconnection. Figure 2.5b shows an example of determining the Burgers vector of a one-layer disconnection on a Σ5 {210}

STGB[7]. The construction of Burgers circuits follows the general Right-Hand(RH)/Start-Finish(SF) convention[66] used for lattice dislocation. The red arrow closing the circuit indicates the Burgers vector carried by this disconnection. The other method is a prior method based on the Bicrystallography theory[67, 68]. The basic procedure of this method is: First, select two separate translational vectors, starting from the common site, in the two grains constructing the bi-crystal. Secondly, draw a vector connecting the ends of these two translational vectors to form a closed circuit. This closing vector would be the Burgers vector of a GB disconnection. The step height of this GB disconnection is then determined by how many atomic planes are crossed by the translational vectors. Figure 2.5c shows examples of this operation in a $\Sigma 17$ $\{410\}$ GB[69]. When the translational vectors are chosen as $\frac{1}{2}\langle 100\rangle$, the corresponding disconnection would have the Burgers vector being $\boldsymbol{b}_{100}$, and the step height of 4 $\{410\}$ atomic layers. While for the translational vectors of $\frac{1}{2}\langle 110\rangle$, the corresponding disconnection shall have the Burgers vector of $\boldsymbol{b}_{110}$ and the step height of 5 $\{410\}$ atomic layers. It needs to mention that GB migration is mediated by the $\boldsymbol{b}_{100}$ type and $\boldsymbol{b}_{110}$ type disconnections correspond to the two shear-coupling modes of <100> STGBs predicted by the Cahn model. In addition, similar to the SMIG model, this prior method would also generate a broad spectrum of GB disconnections with different Burgers vectors and step heights. Nevertheless, the nucleation barrier and the mobility of these predicted GB disconnections could be obtained with the assistance of computational simulations, which makes revealing the favorable GB disconnections for a given GB being possible. The progress in computational simulations will be reviewed in the next section.

Similar to the nucleation of lattice dislocations, the nucleation of GB disconnections would either be homogeneous or heterogeneous. Homogeneous nucleation normally refers to the nucleation of disconnection pairs on a flat GB[70]. Figure 2.5d show a schematic of a typical disconnection pair[7], the two disconnections consisting the pair have the same step height and the same magnitude of Burgers vectors, but the directions of the Burgers vectors are opposite. In Comparison, heterogeneous nucleation could either be the nucleation of disconnections pairs at pre-exist GB defects [71], or the nucleation of disconnections from the GB junctions[72].

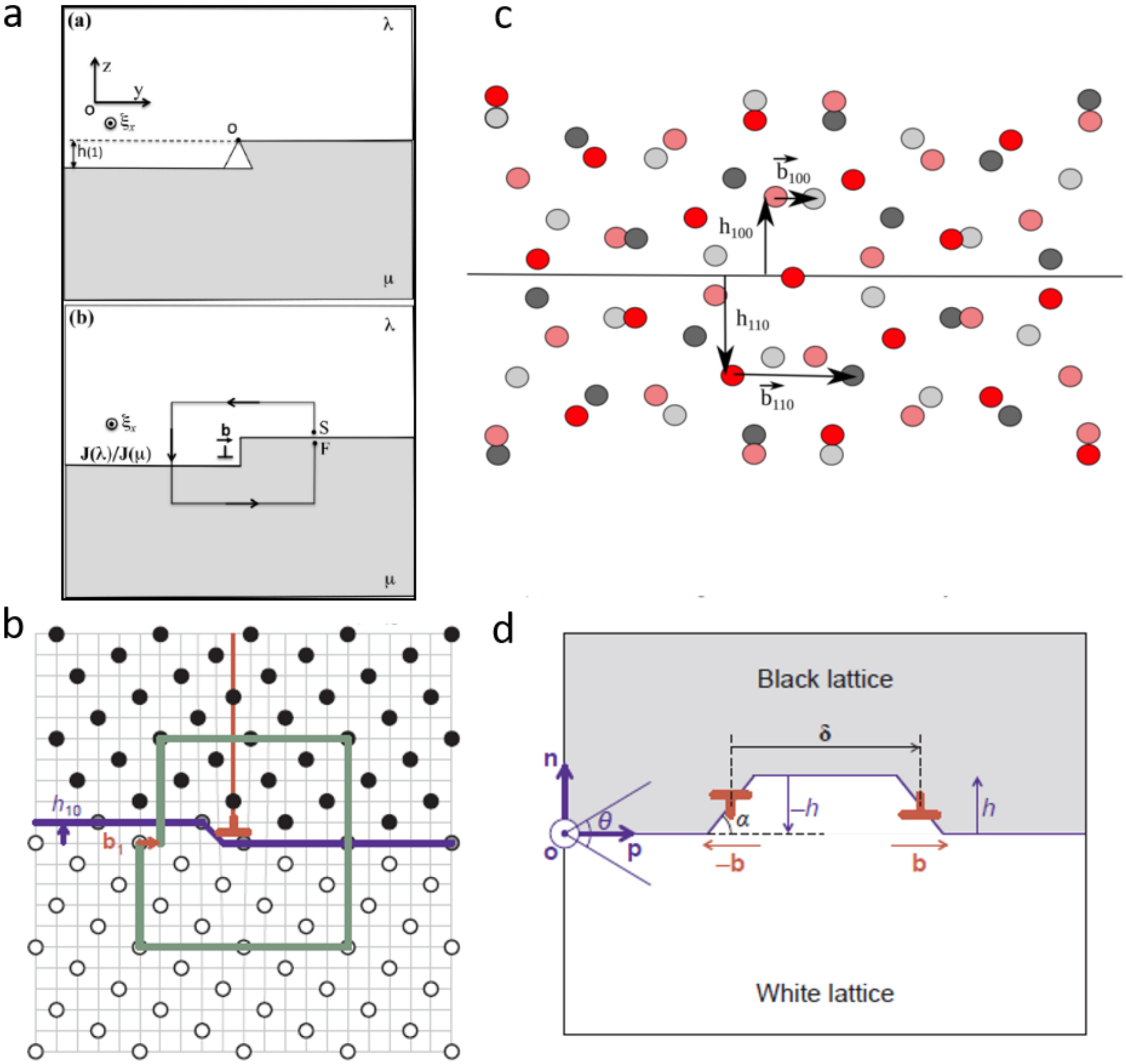
a
(a)
λ
z
y
o
ξ_r
o
h(1)
μ
(b)
λ
ξ_r
b
S
F
J(λ)/J(μ)
μ
c
b100
h100
h110
b110
b
h10
b1
d
Black lattice
δ
n
θ
α
−h
h
o
p
−b
b
White lattice

Figure 2.5 The unifed disconnection model for GB kinetics. (a) Schematic of creating a GB disconnection by jointing two crystals with incompatible surface steps[65]. (b) Example of constructing Burgers circuit around a GB disconneciton on a Σ5 {210} STGB[7]. (c) Example of predicting the admissible disconnections for a Σ17 {410} STGB[69]. (d) Schmatic of the homogeneous nucleation of a disconnection dipole[7].

2.3 Computational Simulations on Shear-coupled GB Migration

Molecular dynamics (MD)[73] and Phase-field crystal (PFC) simulations[74, 75] are the two powerful tools used for understanding the shear-coupled GB migration behaviors. MD simulations have advantages in the controllable deformation conditions and the capability of examining atomic trajectories during deformation. However, the limited time-scale (i.e., usually tens of nanoseconds) makes that MD simulations are commonly conducted in a large strain rate (e.g., 1m/s). The high strain-rate along with the empirical or semi/empirical potential used in MD simulations usually put doubts on the accuracy of MD simulation results. The PFC simulation offers the capability to investigate the GB migration behaviors in the mesoscale and in a larger time-scale that is enough for diffusion, but the main question lies behind it is that the vacancy concentration in the PFC model is hard to define and control, making the description of deformation behaviors based on the PFC model largely qualitative[75]. As the focus of this thesis is the atomistic processes of GB migration, the literature review on progress of computational simulations would mainly focus on MD simulations.

Most of the previous MD simulations[46, 50, 51, 75-91] were conducted to investigate the shear-coupled migration behaviors of special CSL GBs, such as <100> tilt Σ5 GBs, <110> tilt Σ3 GBs, <110> tilt Σ9 GBs, and <110> tilt Σ11 GBs. Zhang et al. [77, 78, 80, 82] did a series of work on the migration behaviors and mechanisms of <100> tilt GBs in fcc Ni. For instance, they revealed that the mobility of flat <100> tilt Σ5 ATGBs is related to boundary diffusivity and boundary energy[77]. By analyzing the atomic trajectories of GB atoms during migration, they further revealed that the strong anisotropy in boundary diffusivity of different <100> tilt Σ5 ATGBs is related to the string-like atomic motion that is parallel to the <100> tilt axis[80]. In addition, they performed systematic simulations on the shear responses of both special Σ GBs and general non-Σ GBs with different GB inclinations[82]. The results showed that shear-coupled GB migration was observed in all studied general GBs, independent of GB inclination, which was attributed to the lower critical stress for shear-coupled GB migration than that for GB sliding. While in comparison, shear-coupled GB migration was observed only in some Σ5 GBs. Very recently, Li et al[91] investigated the lattice transformation during the migration of a series of <100> Σ STGBs. They found that the {110} atomic plane or the {100} atomic plane could be the invariant plane during GB migration. Accordingly, they defined a quantity named the nominal magnitude of shear as a criteria to determine the migration-to-sliding transition of these GBs.

For the <110> tilt GBs, Sansoz and Molinari[73] examined the mechanical behaviors of 18 <110> STGBs and 2 <110> ATGBs in Cu and Al. Three deformation modes were observed, including GB sliding, emission of partial dislocations from GB, and GB migration. Figure 2.6 shows the atomistic processes of these three modes. As shown in Figure 2.6a, GB sliding was mediated by the random atomic shuffling of GB atoms, as indicated by the non-directional movement of atoms at the site enclosed by the dashed circle. In contrast, the nucleation of partial dislocation from the GB was observed at a free volume of the GB (area in the circle in Figure 2.6b). For the deformation mode of GB migration, the atomistic mechanism was found to be via the collective movement of atoms at the GB with the movement direction perpendicular to the loading condition (Figure 2.6c). Similarly, Zhang et al.[88] reported the same three deformation modes activated during the shear deformation of Cu bi-crystals with <110> Σ11 (113) STGB and ATGBs. It needs to mention a special case that the shear response of <110> Σ3 {112} GB (or called incoherent twin boundary) was found to be the dissociation of the GB with the formation of a new phase-9R phase [16, 83].

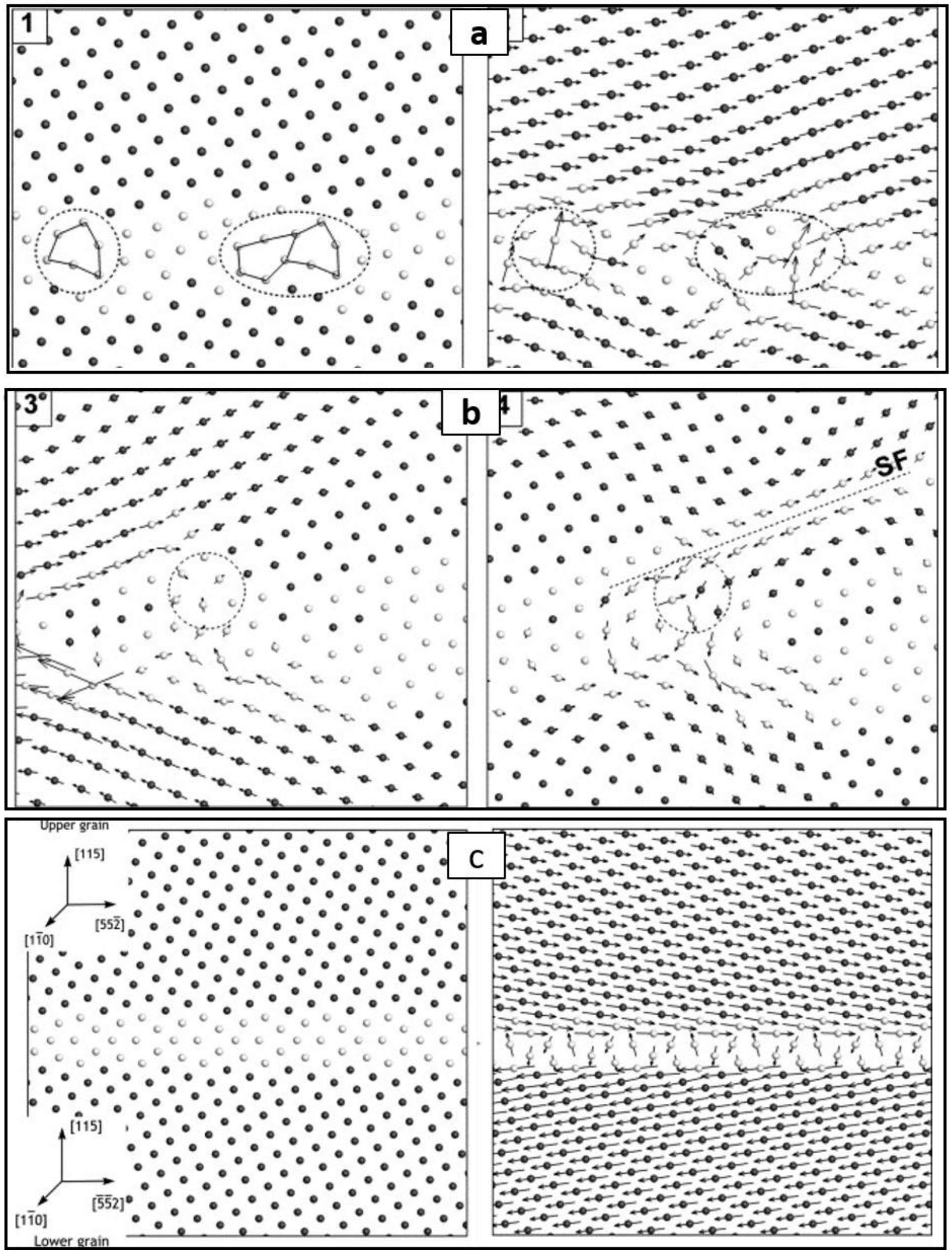
1
a
3
b
4
SF
c
Upper grain
[115]
[55$\bar{2}$]
[1$\bar{1}$0]
[115]
[$\bar{5}\bar{5}$2]
[1$\bar{1}$0]
Lower grain

Figure 2.6 Snapshots of MD simulations showing the atomic movements during the three types of deformation mode[77]. (a) GB sliding mediated by the ramdon atomic shuffing. (b) Emission of a partial dislocation, as indicated by the emergence of a stacking fault (SF), at a free volumn of the GB. (c) GB migration accommodated by the collective movement of atoms.

Except the GB misorientation and inclination, shear loading direction is another factor affecting the GB migration behaviors. Wan et al [46, 50, 51, 90] did a series of work on the influence of shear direction on the migration behaviors of various kinds of GBs, including Σ9 <110>

{221} STGB, {115}/{111} ATGBs, GBs vicinal to <110> Σ11 (113) STGB, and Σ7 <111> {132} STGB. Different shear responses, including GB sliding, shear-coupled GB migration, emission of dislocations, GB faceting, and formation of the 9R phase, were observed when the shear direction was altered. Temperature can also influence the GB migration behaviors as the increase in temperature would change the equilibrium states of the GB structure [75]. For instance, Cheng et al.[92] studied the migration behaviors of <100> Σ5 (310) STGB in Al at the temperature range of 300K-600K, and they found the abrupt change of GB migration behavior at a temperature of 500K due to the change of GB structure. It needs to mention that introducing vacancy defects can also lead to the change of GB structural phase (also called GB complexion transitions [93, 94]). For instance, Frolov et al[95] reported the structural phase transformations in <100> Σ5 (310) STGB and <100> Σ5 (210) STGB. There are two types of GB structural phase, split kites, and filled kites, for the Σ5 (210) STGB. The shear-coupled migration of these two types of GBs have different magnitudes and signs of shear-coupling factors[86], corresponding to the <100> mode and <110> mode as stated in the previous section regarding the Cahn model.

Another research focus of MD simulations on shear-coupled GB migration is regarding GB disconnections. Rajabzadeb et al.[96] reported that the nucleation and motion of GB disconnections accommodated the shear-coupled migration of a Σ13(320) GB in a Cu bicrystal. Akin to this, Combe et al.[69] found that GB disconnections mediated the two observed migration modes of a Σ17(410) GB in a copper bicrystal. One of the differences between these two migration modes is that the disconnection mediating the <100> mode migration was found to have some kinks along the disconnection lines. In addition, Combe et al.[71] studied the heterogeneous nucleation of disconnection in the same Σ17(410) GB as above, they found that the pre-exist sessile GB disconnection in an imperfect GB can act as a source of mobile disconnections, leading to the easier migration of imperfect GB than the perfect one. Larranaga et al.[97] did similar work on the heterogeneous nucleation of disconnections in a Σ41 (540) STGB. It is also reported that vacancies can enhance the shear-coupled GB migration by weakening the line tension of a disconnection loop and serving as energy-favorable sites for disconnection nucleation[98].

There are also progresses on the simulations of stress-driven GB migration in the polycrystalline environment[99-103]. Farkas et al.[99] did simulations on plastic deformation of nanocrystalline Ni containing 200 grains of the average grain size of 5nm, where they observed the movement of GBs at the maximum distance of 2.5 nm. Aramfard et al.[100] studied the influence of GB triple junctions on the shear-coupled migration of GBs in nanocrystalline Cu. Compared to the bicrystal model, GB migration in polycrystalline materials receives constraints from neighbor grains and GB triple junctions, and the asymmetric pinning effects of GB triple junctions resulted in non-linear GB migration behaviors[100]. In addition, Jason et al.[102] investigated the reconstruction of the GB network after the cycling deformation of a nanocrystalline Al, where they observed an increase in special boundary (i.e., Σ GBs) fraction after the deformation. Spencer et al.[72] reported the concurrent motion GB triple junctions (TJs) and proposed a theory of coupled GB/TJ migration to describe the microstructure evolution during the plastic deformation of polycrystalline materials.

Unlike the well-established knowledge on the shear-coupled migration of flat tilt GBs, there is less report on the migration behaviors of non-flat (i.e., faceted) GBs and non-tilt (i.e., mixed) GBs. For the mixed GBs, using a combination of discrete dislocation dynamics simulations and analytical arguments, Lim et al.[104] studied the stress-driven migration of a series of low-angle mixed GBs (LAMGBs). They found that the glide of dislocations led to the migration of LAMGBs and the migration velocities were proportional to the external-applied stress but independent of GB misorientation [104]. For the faceted GBs, only the thermal-driven migration of these GBs was systematically investigated. For instance, Hadian et al.[105, 106] studied atomistic migration mechanisms of mixed faceted or kinked GBs that are vicinal to the <111> Σ 7 STGB in Al. Figures 2.7a and 2.7d present the bicrystal models used for constructing the faceted or kinked GBs. The atomistic structures of these GBs after relaxation at 0 K are shown in Figures 2.7b, 2.7c, 2.7e, and 2.7f, clearly indicating the faceted or kinked feature of these GBs. The migration of faceted GB was found to be mediated by the nucleation and motion of double kinks, while the kinked GB migration was believed to be via the propagation of pre-existing single kinks along the GB. Moreover, further investigation on the migration of this kind of faceted GB revealed that it is via the collective movement of disconnections at lower driving force but by the detachment of disconnections from facet junction and their subsequent motion along the GB at higher driving force[106].

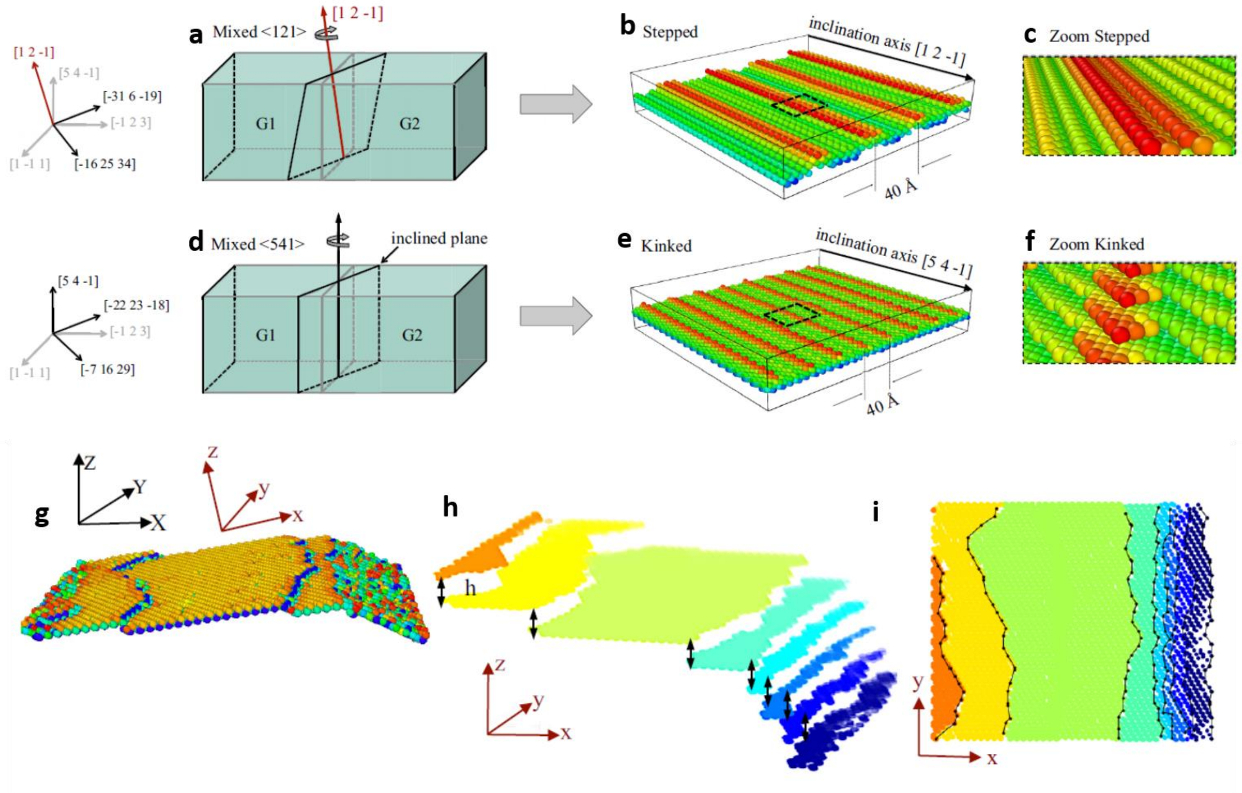
[1 2 -1]
[5 4 -1]
[-31 6 -19]
[-1 2 3]
[1 -1 1]
[-16 25 34]
a
Mixed <121>
[1 2 -1]
G1
G2
b
Stepped
inclination axis [1 2 -1]
40 Å
c
Zoom Stepped
[5 4 -1]
[-22 23 -18]
[-1 2 3]
[1 -1 1]
[-7 16 29]
d
Mixed <541>
inclined plane
G1
G2
e
Kinked
inclination axis [5 4 -1]
40 Å
f
Zoom Kinked
g
Z
Y
X
z
y
x
h
h
z
y
x
i
y
x

Figure 2.7 Atomistic mechanisms of the thermal-induced migration of mixed tilt-twist GBs in vicinal to the <111> Σ 7 STGB in Al [105, 106]. (a,d) The bicrystal models used for constructing the GBs. Snapshots (b, e) and enlarged views(c, f) of MD simulations showing the equilibrium structure of the facted mixed GB(b, c) and the kinked mixed GB(e, f). (g) Snapshot showing the structure of faceted GB. (h, i) Views of these GB disconnections (steps) from different directions by applying the step-detection algorithm.

2.4 Deformation-induced Formation and Annihilation of GBs

Nanocrystalline metallic materials often show superior strength and hardness compared to their bulk counterparts, as the strength of materials obeys the classical Hall-Petch relationship that is ‘smaller’ is stronger. Benefited from the exceptional mechanical properties, nanocrystalline metallic materials have broad applications as structural components in areas such as transportation and nanomaterials-based devices [107, 108]. General methods applied to fabricate nanocrystalline materials include consolidation from nanocrystalline powders, electrodeposition, and severe plastic deformation [109]. Among which, severe plastic deformation is through achieving intensive grain refinement of coarse-grained materials to eventually obtain the nanocrystalline structure. Numerous studies have been performed in the past to investigate the grain refinement mechanism during several plastic deformation [110-113], and one general finding is that the grain refinement is highly related to the deformation-induced formation of GBs. For instance, Kamikawa et. al. investigated the microstructural evolution of a Ti-added ultralow carbon interstitial free steel that was deformed by accumulative roll-bonding and found that the produced ultrafine structures mostly consist of deformation-formed HAGBs[111]. Similar GB network evolution that the number of GBs and the fraction of HAGBs in overall GBs increased with strain accumulating was also observed during the accumulative rolling-bonding of a commercial purity aluminum[113]. However, the dynamic process of HAGB formation remains largely unclear yet, as previous studies commonly used the post-mortem observation to deduce the GB network evolution during deformation.

In comparison to GB formation that leads to grain refinement, GB annihilation is the reversal process that could lead to the coalescence of adjoining grains, consequently leading to grain growth and the softening of nanocrystalline materials[114]. For LAGBs consist of dislocation arrays, GB annihilation is believed to be mediated by dislocation climb at the GB [115, 116]. In comparison, less is known about the mechanism of HAGB annihilation. It is recognized that HAGBs could be the preferable nucleation sites for dislocations[88, 117], deformation twinning[118], and phase transformation[119]. Nanotwins nucleated from HAGB could assist grain growth in nanocrystalline Au films under cyclic loading [118]. Nevertheless, the dynamic process of the HAGB annihilation have not been witnessed.

In addition, metallic nanocrystals possess unique mechanical properties such as pseudoelasticity compared to their bulk counterpart, which make them have prospective applications in flexible electronics[120, 121] and reliable nano electromechanical systems (NEMS)[122, 123]. Both experimental [124, 125] and simulation studies[126-132] have been employed to investigate the pseudoelasticity of various metallic nanowires, including Cu[126, 130], Au[126, 130], Pd[127], and Fe[131], during their uniaxial deformation or bending deformation. By conducting in-situ TEM study, Zheng et al [124] reported a novel pseudoelastic deformation mechanism in an Au nanocrystal that is enabled by the pile-up of full dislocations to form a 15° LAGB during the coupled tensile and bending deformation (Fig. 2.8a-c) and the spontaneous annihilation of this GB after the release of stress. However, the GB annihilation process was too fast to be captured. Recently, Li et. al. [133] reported that nanotwins can assist the reversible formation of LAGB upon reciprocating shear load of Au nanocrystals. Similar mechanically induced formation of GB has also been observed during the bending deformation of Ni nanowires (Fig. 2.8d-g) [134]. All these studies indicate that mechanically-induced GB may play important roles to assist the pseudoelastic deformation of metallic nanocrystals. Fundamental understanding on the deformation-induced formation and annihilation of HAGB would inspire future applications of metallic nanocrystals in reliable NEMS systems devices.

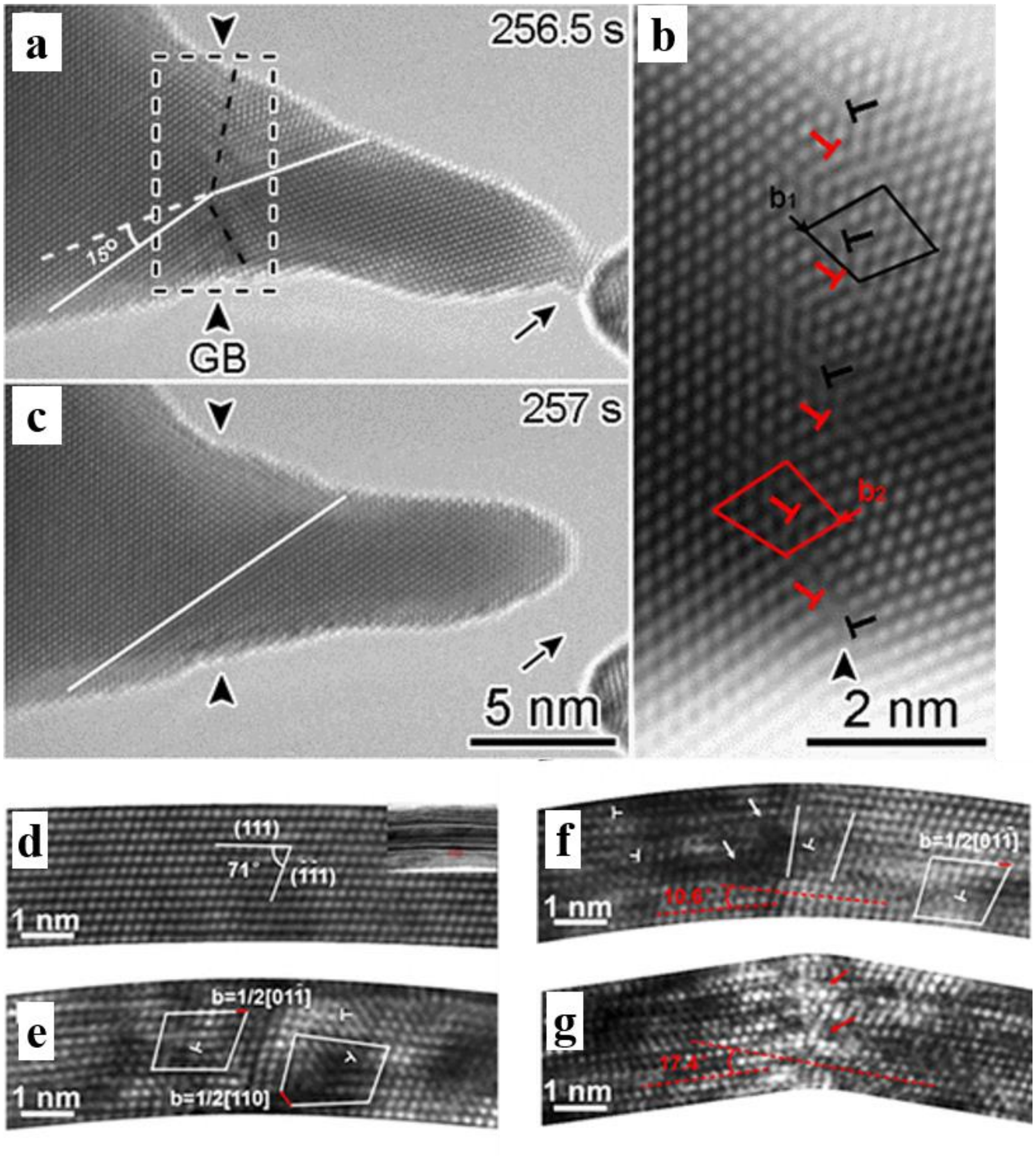
a
256.5 s
15°
GB
b
b1
b2
2 nm
c
257 s
5 nm
d
(111)
71°
(11̄1)
1 nm
e
b=1/2[011̄]
b=1/2[110]
1 nm
f
b=1/2[011̄]
10.6°
1 nm
g
17.4°
1 nm

Figure 2.8 Mechanical-induced formation of GBs in an Au nanocrystal[124] (a-c) and in the Ni nanowire[134] (d-g). (a)Formation of a 15° LAGB during the off-axial deforamtion of an Au nanocrystal. (b) Fourier filtered images showing that the LAGB is consisted of arrays of full dislocations. (c) Crystal lattice recovered to it pristine state after the release of stress. (d) Atomic structure of the Ni nanowire before bending. (e-g) Bending induced formation of a 17.4° flat GB in the Ni nanowire.

2.5 Motivation and Objectives

Although considerable progress has been made in investigating the shear-coupled GB migration behavior and deformation-induced formation of GBs, there remain plenty of unresolved issues that need to be addressed due to the complexity of the GB structure. Specifically, most of the previous experimental studies were conducted at either macro-scale (i.e., bicrystal studies) or micro-scale (i.e., conventional TEM studies), which offered no information on the GB migration mechanisms at the atomic scale. Current knowledge on the atomistic mechanisms of GB migration largely relied on MD simulations, the accuracy of which, however, usually suffers from the applied large strain rate and empirical/semi-empirical potential. Moreover, most of the previous MD simulation studies focused on the migration of flat and special GBs, such as Σ5 (210) STGB. While in the real case of polycrystalline materials, GBs are usually to be faceted at the atomic scale[135, 136], it is unclear whether and how these faceted GBs migrate under the external shear loading. In addition, general GBs in polycrystalline materials normally refer to the mixed tilt-twist GBs. Limited experimental research on the shear-coupled migration of a mixed GB reported that only the tilt part of mixed GB contributes to the migration[28]. However, how the mixed GBs migrated at the atomic-scale remains largely clear to date due to the lack of both experimental and simulation evidence. Furthermore, the gradual increase of the fraction of HAGBs in overall GBs during the accumulating several plastic deformation of metallic materials implies the LAGB-to-HAGB transformation during the process. However, the dynamic process of such transformation remains unclear as limited by the postmortem observation in previous studies. Thereafter, the objectives of this study are proposed as follows:

1. Find out and fabricate representative faceted GBs for the investigation of their shear-coupled migration behaviors; reveal the atomistic mechanisms of the migration of these typical

faceted GBs via the in-situ HRTEM observation; further investigate the influences of facet types and external loading conditions on the migration behaviors of faceted GBs.

2. Search and fabricate representative mixed tilt-twist GBs for the investigation of their shear-coupled migration behaviors; Investigate the shear responses of typical mixed tilt-twist GBs and reveal the dominant atomistic mechanisms via the in-situ HRTEM observation; Explore the lattice transformation relations during the migration of these mixed GBs.

3. Reveal the atomistic mechanism of the LAGB-to-HAGB transformation and uncover the annihilation mechanism of the HAGB during the reversal deformation.

Considering that GBs in the real case are common to be faceted and to be mixed tilt-twist, the research objectives proposed in this study would provide important implications for understanding the shear-coupled migration of general GBs in polycrystalline materials. The revealed GB migration mechanisms at the atomic scale could also benefit the development and improvement of theoretical models for describing GB migration. Moreover, uncovering the atomistic mechanism of the formation and annihilation of HAGB during reciprocating bending deformation of Au metallic nanocrystals would provide insights into grain refinement mechanisms during severe plastic deformation and important guidelines for the development of reliable and sustainable NEMS devices.

3.0 Materials and Experimental Procedures

In this chapter, the materials and experimental procedures employed in this dissertation will be introduced. Au is selected as the model material, due to its excellent anti-oxidation property and the moderate stacking fault energy, to investigate the shear-coupled migration behaviors of <110> tilt faceted GB and mixed tilt-twist GB in fcc metals, along with the deformation-induced formation and annihilation of a HAGB during reciprocating bending. The methodology of in-situ fabricating nano bi-crystals with desirable GB structures and single-crystal nanowires inside the TEM will also be presented. Moreover, the methodology used to identify the GB plane and the simulation method used to support the experimental results will be introduced.

3.1 Materials

The fcc Au metal used in this study is acquired from ESPI metals in the form of wire with a diameter of 0.254 mm, and the purity at 99.999%. To acquire specimens that are suitable for high-resolution TEM observation and fabrication of single-crystal nanowires or nano bi-crystals, subtle specimen preparation is needed. Firstly, the metal wires were cut into rods with a length of ~5 mm to make sure they can be mounted into the TEM holder. Then, one end of these short metal rods was compressed by a punch to create a flat substrate. After that, the flat substrate was torn apart with the clamp, which will create a fracture surface with plenty of nano-tips (Figure 3.1a). These nano-tips are thin enough for the high-resolution TEM observation and thus are suitable for the subsequent preparation of single-crystal nanowires or nano bi-crystals. Figure 3.1b shows the

HRTEM image of a typical Au nano-tip with the zone axis being $\langle 0\bar{1}1\rangle$. All samples were plasma cleaned before the TEM observation to minimize the potential influence of carbon deposition under electron beam irradiation.

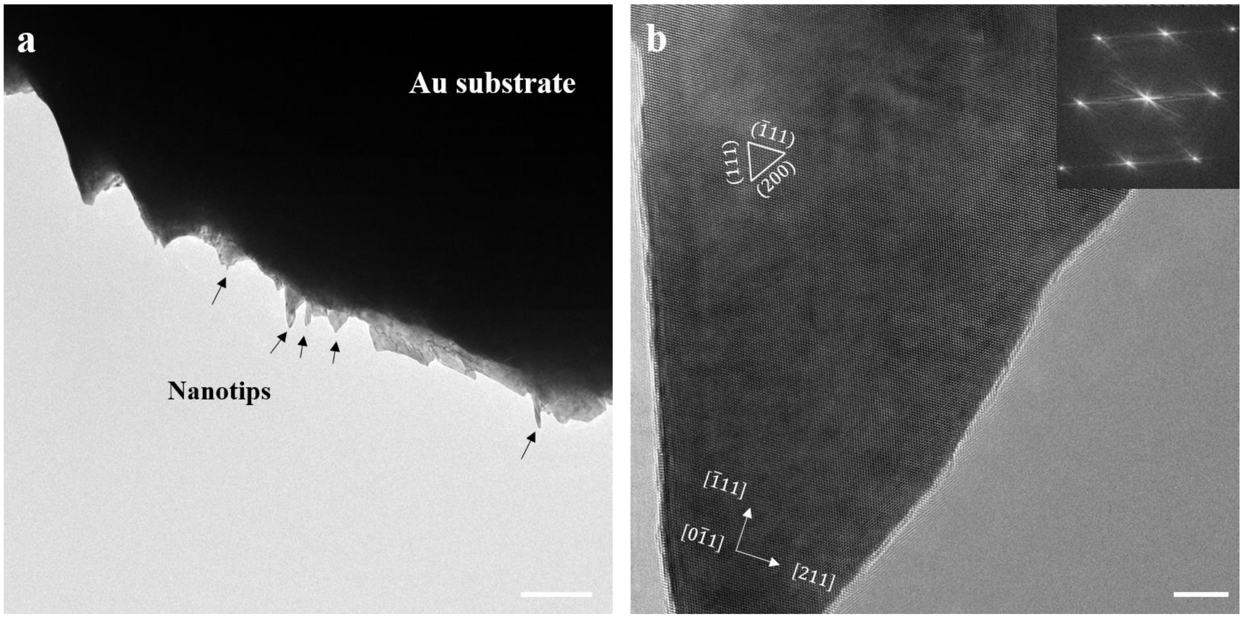

Figure 3.1 (a) Fracture surface of the flat Au substrate with plenty of nano-tips on it. (b) HRTEM image of a typical Au nano-tip. The zone axis of the nano-tip is $\langle \mathbf{0\bar{1}1}\rangle$. Insert is the correspodning fast fourier transformation (FFT) pattern of the HRTEM image, which agrees well with the features of $\langle \mathbf{0\bar{1}1}\rangle$-oriented pattern of FCC Au. Scale bar: (a) 200 nm; (b) 5 nm.

3.2 Experimental Procedures

3.2.1 In-situ TEM Experimental Configuration

The TEM observations in this work were carried out with an FEI Titan Themis G2 200 probe Cs corrected STEM (Figure 3.2a) at the Nanoscale Fabrication & Characterization Facility (NFCF) lab of University of Pittsburgh. The Nanofactory scanning tunneling microscope (STM) platform was adopted to perform the in-situ TEM study. Figure 3.2b shows the configuration at the head of the Nanofactory STM holder. It consists of two parts: one is the fixed sample side, while the other is the movable probe side. The as-prepared short metal rod with plenty of nano-tips (as stated in Chapter 3.1) was mounted into the fixed sample side. For the probe side, metal probe (prepared by creating the wedge shape fracture surface of a metal rod) was mounted onto a hat that can clamp on the piezo tube. The movement of the probe is controlled by the motion of the hat that is driven by the piezo tube. With the capability of moving the probe side at the mutual-orthogonal axes x, y, and z, the two sides of the platform can be approached and eventually get into touch with each other at the atomic scale inside TEM (Figure 3.2c). In addition, bias potential

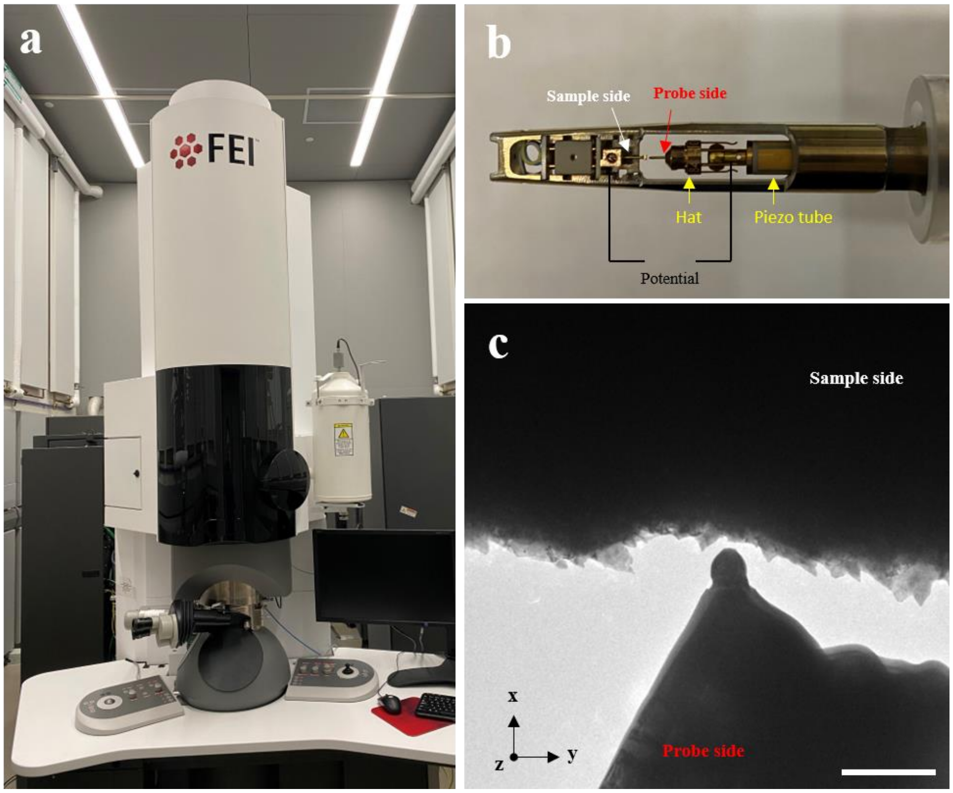

Figure 3.2 In-situ TEM experimental configuration used in this work. (a) photo of FEI Titan Themis G2 200 probe Cs corrected STEM at the NFCF lab. (b) The configuration at the head of Nanofactory, which contains the fixed sample side and the movable probe side. (c) The approaching two sides under the TEM observation. x, y, and z axes indicate the motion directions of the probe side.

within the range of ±10 V can be applied on the side sample, which enables the fabrication of high-quality sub-100nm single-crystal nanowires or nano bi-crystals through the in-situ welding processing[137, 138]. Next, the strategy to fabricate nano bi-crystals with desirable GB structure will be introduced in detail.

3.2.2 Fabrication of Nano Bi-crystals with Desirable GB Structure.

Although the Nanofactory STM holder possesses a great capability to manipulate and process (e.g., welding) the sample inside TEM, along with excellent spatial and temporal resolutions, fabricating nano bi-crystals with desirable GB structure remains to be a huge challenge. To achieve this goal, the crystal orientations of the crystals at both the sample side and the probe side must be precisely controlled. Figure 3.3a shows an example of an experimental set-up before fabricating the nano bi-crystal. Firstly, the probe side was treated by applying the welding-fracture strategy to get a $\langle 001 \rangle$-oriented nanocrystal at the head of the probe. The low-index $\langle 001 \rangle$ zone axis ensures the acquisition of the HRTEM image, wherein the bright spots can be interpreted as the atom columns. Then, a nano-tip region at the sample side, which is also $\langle 001 \rangle$-oriented and has a misorientation angle of ~30° with the crystal at the probe side, was selected as the reference to move the probe side close in. Thereafter, a bias potential of ~1 V was applied at the sample side, and meanwhile, the probe side was moved to get in touch with the sample. After doing these operations, a $\langle 001 \rangle$-oriented nano bi-crystal with a misorientation angle of ~ 30° is expected (not shown here), but there remains large uncertainty on controlling the GB plane of the bi-crystal. Thereby, a trial-and-error approach was adopted to eventually get the nano bi-crystal with a desirable GB structure.

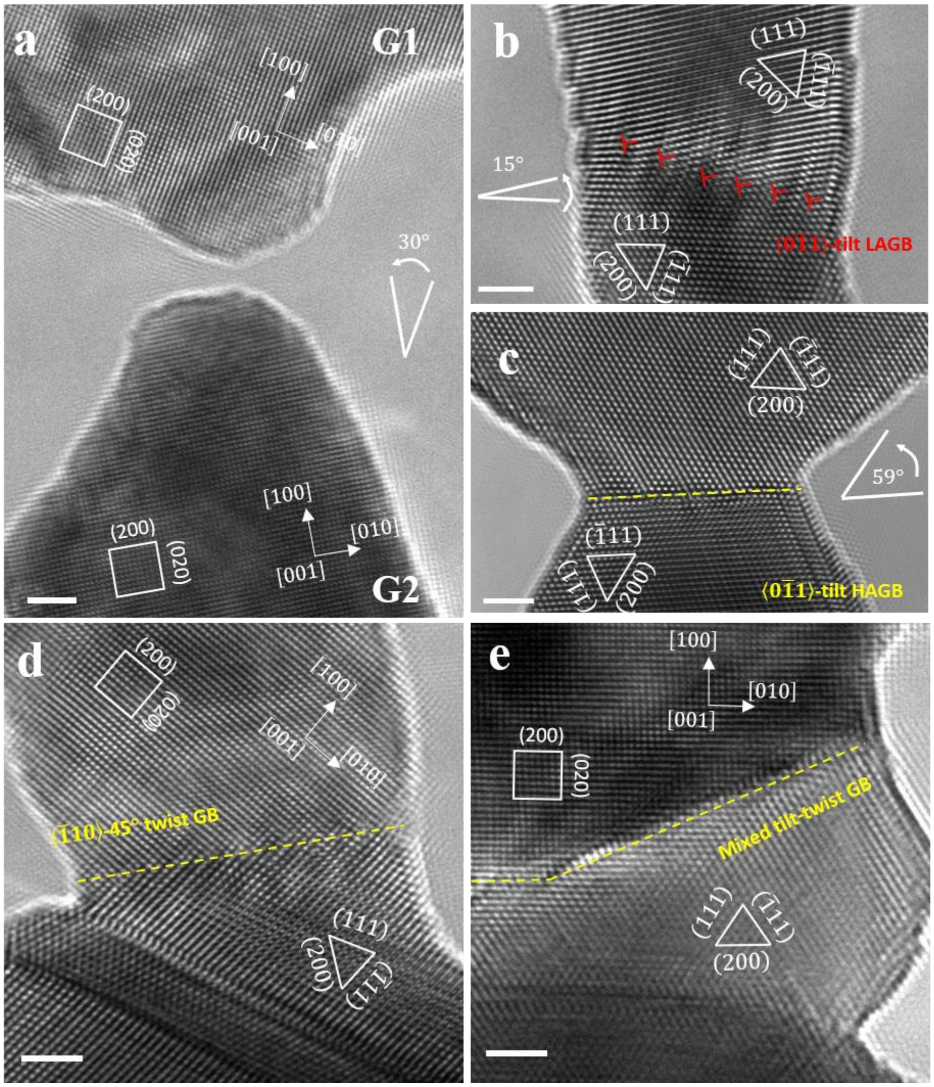
a
G1
[100]
(200)
(020)
[001]
[010]
30°
(200)
(020)
[100]
[010]
[001]
G2
b
(111)
(200)
(1̄11)
15°
(111)
(200)
(11̄1)
⟨01̄1⟩-tilt LAGB
c
(111)
(1̄11)
(200)
59°
(1̄11)
(111)
(200)
⟨01̄1⟩-tilt HAGB
d
(200)
(020)
[100]
[001]
[010]
⟨1̄10⟩-45° twist GB
(111)
(200)
(1̄11)
e
[100]
[010]
[001]
(200)
(020)
Mixed tilt-twist GB
(111)
(1̄11)
(200)

Figure 3.3 Experimental set-up and examples of fabricating nano bicrystals with desirable GB structure. (a) The positions of the sample side and the probe side before the fabrication crystal. (b-d) Examples of as-fabricated GB structure: $\langle \mathbf{011} \rangle$-tilt 15° LAGB (b); $\langle \mathbf{011} \rangle$-tilt 59° HAGB (c); $\langle \bar{\mathbf{1}}\mathbf{10} \rangle$-twist 45° GB (d); mixed tilt-twist GB (e).

Except the $\langle 001 \rangle$ zone axis, $\langle 011 \rangle$ direction is also a common low-index zone axis of fcc crystals. Therefore, by controlling the orientations of nano crystals at both the sample side and the probe side, and applying the bi-crystal fabrication technique and trial-and-error approach, a variety of bi-crystals with different GB structures can be obtained. For instance, the $\langle 011 \rangle$-tilt 15° LAGB which is composed of an array of lattice dislocations is presented in Figure 3.3b. The $\langle 011 \rangle$-tilt 59° HAGB with a flat GB plane is shown in Figure 3.3c. In addition, twist GB or mixed tilt-twist

GB can also be fabricated by differencing the zone axis of the crystals at the two sides (Figure 3.3d and 3.3e). Then, the in-situ shear testing on bi-crystals with desirable GB structure was conducted by moving the probe side with the piezo-manipulator of the STM holder at a constant rate between 0.001 and 0.01 nm s^{-1}. Note that the fabrication of the single-crystal nanowires is similar to that of bi-crystals, the only difference the crystal orientations of the sample side and the probe side are close. Relevant research on the fabrication and mechanical testing of single-crystal nanowires using in-situ HRTEM platform can be found in Refs. [139-142]

3.2.3 GB Plane Identification

Successfully fabricating the bi-crystals with desirable GB structures does not guarantee the successful conduction of in-situ TEM studies on GB behaviors. Precisely identifying the GB positions and GB structures is critical for understanding the GB behaviors. Here we take the $\langle 011 \rangle$-tilt HAGBs that will be investigated as examples. To identify the GB positions and mark the GB structures of the bicrystals, we marked the (111) planes of G1 and the $(11\bar{1})$ planes of G2 first. As shown in Figures 3.4a and 3.4b, these lattice planes, as indicated by the blue dashed lines, would intersect with each other at the junctions of the bi-crystals, which determined the positions of GB. Note that the atoms on the GBs might deviate from the lattice planes of crystal, i.e., G1 and G2, due to the existence of misfit strain. Then, the intersections of these lattice planes were connected by the yellow dashed lines to represent the GB planes. The serrated feature of these yellow dashed lines reflected the existence of interfacial steps, such as $(\bar{1}\bar{1}1)/(002)$ type steps and $(111)/(11\bar{1})$ type steps that will be discussed in section 5.1.

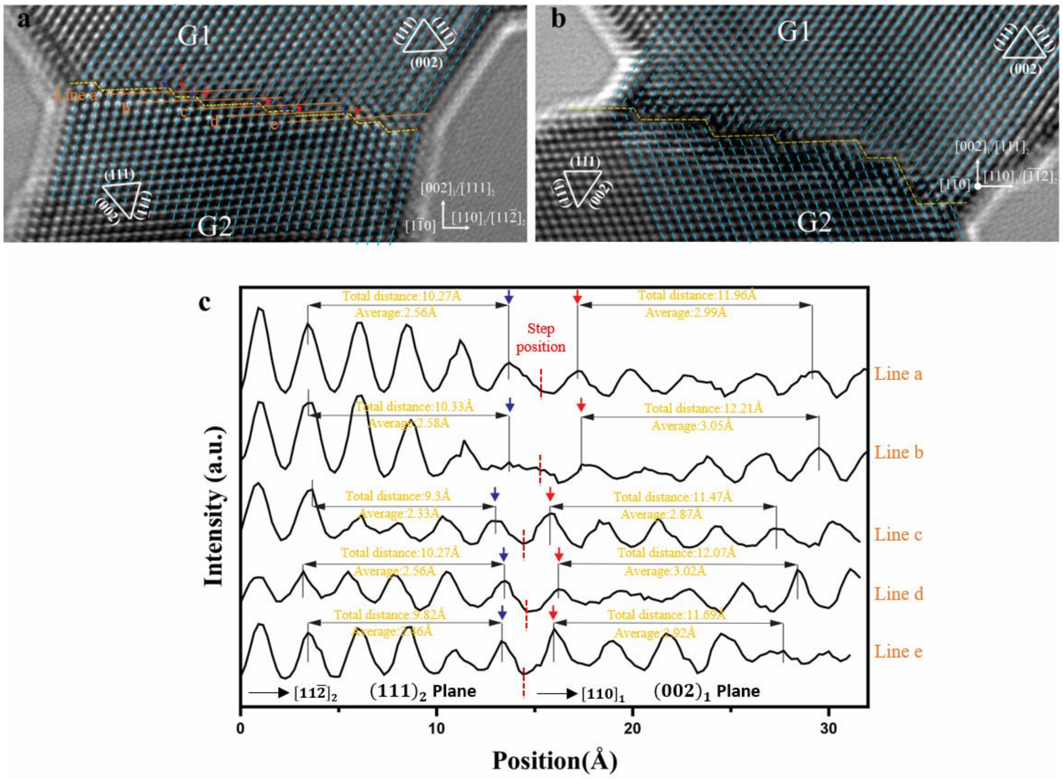

Figure 3.4 The identification of faceted GBs. (a, b) Two types of faceted ATGBs which both contain the $(\mathbf{002})/(\mathbf{111})$ GB facet. The blue dash lines indicate the $\{\mathbf{111}\}$ lattice planes. The yellow dash lines indicate the positions of GB planes. (c) The contrast intensity line profiles are extracted along the orange solid lines in (a). For a clear comparison, the line profiles were selected to make sure the sixth and the seventh atom columns be on the two sides of the interfacial steps. Scale bar: 2nm

Moreover, we took advantage of line intensity profile analysis to further confirm the existence and positions of these steps, considering that these steps should separate the (002) plane in G1 (i.e., $(002)_1$ plane) and the (111) plane in G2 (i.e., $(111)_2$ plane). One example is shown in Figure 3.4c, where we extracted the line intensity profiles along the orange solid lines that threaded the steps in Figure 3.4a. The orange solid lines were nearly parallel to the (002) plane and [110] direction of G1 and the (111) plane and $[11\bar{2}]$ direction of G2. In theory, the lattice spacings along the [110] direction and $[11\bar{2}]$ direction under the projection of $[1\bar{1}0]$ direction in Au is ~2.88Å and ~2.5Å, respectively. As seen from Figure 3.4c, the average lattice spacings between the atom columns (i.e., the distances between intensity peaks) at the left side of all five steps were close to 2.5 Å, while those at the right side of the steps were close to 2.88Å. Therefore, the interfacial steps that we marked out indeed separated the $(002)_1$ and $(111)_2$ planes. Similar analyses on the line intensity profiles were also carried out in other types of GB, such as the mixed tilt-twist GB.

3.3 Simulation Methods

MD simulations were performed to help understand the atomistic mechanisms of the shear-coupled migration of faceted GBs and mixed tilt-twist GBs and the annihilation of the HAGB during bending deformation in Au. The simulation results presented in Chapter 4 was performed by our collaborators Chuang Deng and Jianwei Xiao from the University of Manitoba, while those presented in Chapter 5 and 6 were performed by myself. The simulations were conducted on an Au bicrystal structure using the Large-scale Atomic/Molecular Massively Parallel simulation (LAMMPS)[143] and embedded atom method (EAM) potential [144] for Au.

In Chapter 4, for constructing "zig-zag" $(002)/(111)$ ATGB, we first constructed a $(10\ 10\ 7)/(10\ 10\ \bar{7})$ STGB by joining two separate orthogonal crystal lattices along the <10 10 7> direction as shown in (Figure 3.5a). Then the $(10\ 10\ 7)/(10\ 10\ \bar{7})$ STGB were optimized at 300 K under zero pressure with an isothermal-isobaric (NPT) ensemble to obtain the equilibrium "zig-zag" $(002)/(111)$ ATGB (Figure 3.5c). For faceted GB consisting of $(111)/(11\bar{1})$ STGB and $(002)/(111)$ ATGB, we first constructed a $(113)/(771)$ ATGB by joining two separate orthogonal crystal lattices along the $< 1\ 1\ 3 >$ and $< 7\ 7\ 1 >$ direction (Figure 3.5b). Then, the $(113)/(771)$ ATGB were optimized at 300 K by using an NPT ensemble (Figure 3.5d). Periodic boundary conditions were applied along all the directions under structural optimization. In the shear deformation, a constant shear velocity of 1 m s^{-1} parallel to the GB plane at the temperature of 300 K was applied on a fixed area of the top grain along the <7 7 20> direction for $(10\,10\,7)/(10\,10\,\bar{7})$ STGB or along <3 3 2> direction for (113)/(771) ATGB (Figure 3.5). Periodic boundary conditions were applied along the <110> tilt direction, and the canonical (NVT) ensemble was used in this case.

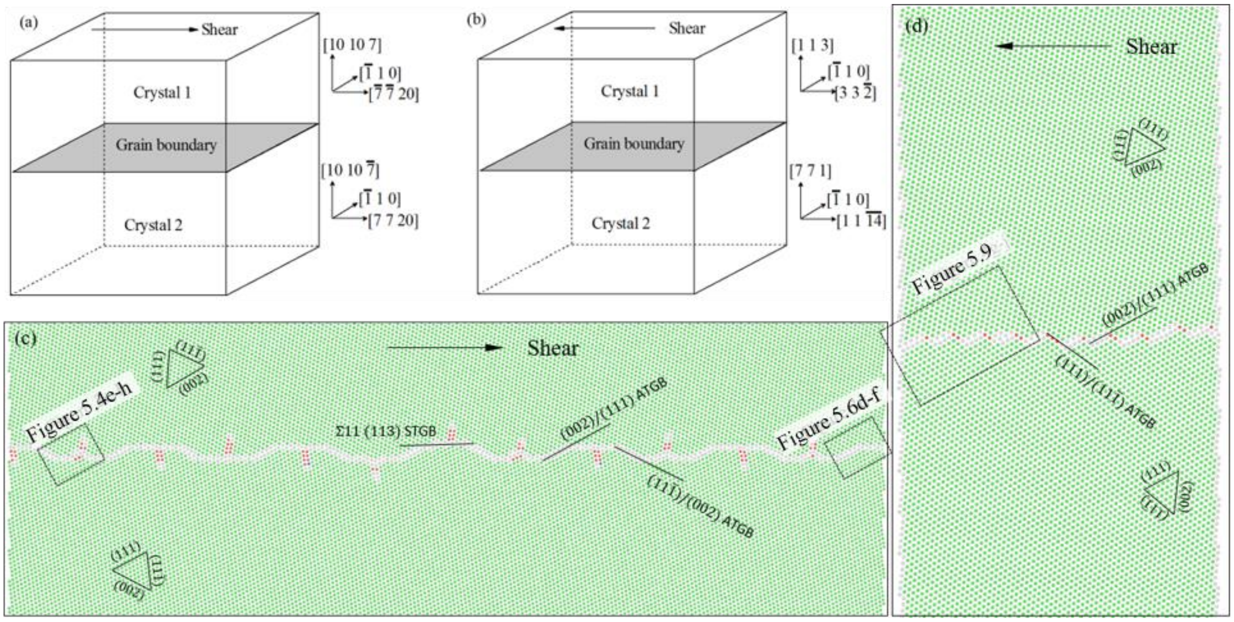
(a)
Shear
Crystal 1
Grain boundary
Crystal 2
[10 10 7]
[$\bar{1}$ 1 0]
[$\bar{7}$ $\bar{7}$ 20]
[10 10 $\bar{7}$]
[$\bar{1}$ 1 0]
[7 7 20]
(b)
Shear
Crystal 1
Grain boundary
Crystal 2
[1 1 3]
[$\bar{1}$ 1 0]
[3 3 $\bar{2}$]
[7 7 1]
[$\bar{1}$ 1 0]
[1 1 $\overline{14}$]
(c)
Shear
Figure 5.4e-h
Σ11 (113) STGB
(002)/(111) ATGB
(111)/(002) ATGB
Figure 5.6d-f
(111)
(002)
(d)
Shear
Figure 5.9
(002)/(111) ATGB
(111)/(111) ATGB
(111)
(002)
(200)

Figure 3.5 Schematic of the bicrystal computational cells and corresponding optimized atomistic structure for $(\mathbf{10\,10\,7})/(\mathbf{10\,10\,\bar{7}})$ STGB (a,c) and $(\mathbf{1\,1\,3})/(\mathbf{7\,7\,1})$ ATGB (b,d). Figure 4.4e-h and Figure 4.6d-f are captured from different regions at the faceted $(\mathbf{10\,10\,7})/(\mathbf{10\,10\,\bar{7}})$ STGB, as indicated by the dashed rectangles in (c). Figure 4.9 are captured from the region as indicated by the dashed rectangles in (d).

In Chapter 5, a total of three Au bicrystal models that were constructed by joining two separate crystal lattices (grain 1 and grain 2 in Fig. 3.6a) with different lattice orientations (as shown in Figs. 3.6b-d) together along the Z axis are studied in this work. Structural optimization of these bicrystals was performed using the conjugate gradient method and with periodic boundary conditions along all three dimensions. Note that the lattices in all bicrystal models are slightly strained to meet the periodic boundary conditions given that the periods of the lattices in directions parallel to the GB planes, i.e., X and Y axes, are incommensurate. The applied strains and the dimensions of these bicrystals are summarized in Table 3.1. This is a commonly used strategy to construct the incommensurate GBs in simulations [145-147]. We have also examined different integer ratios of the period to construct the bicrystals (i.e., different strains and dimensions), and the observed shear-coupled GB migration behavior is quite similar. The bicrystal models were further equilibrated at 300K with a pressure of 0 bar for 50ps using the NPT ensemble MD simulations. Two thin slabs with a thickness of 1nm at the top and the bottom of the bicrystals were fixed, and the shear deformation was applied by displacing the top fixed slabs moving along the X axis of the bicrystals at a constant speed of 1 m s^{-1} (Fig. 3.6a). The shear deformation of the bicrystals was performed at 300K via the NVT ensemble, with periodic boundary conditions along the Y axis and free surfaces along X and Z axes.

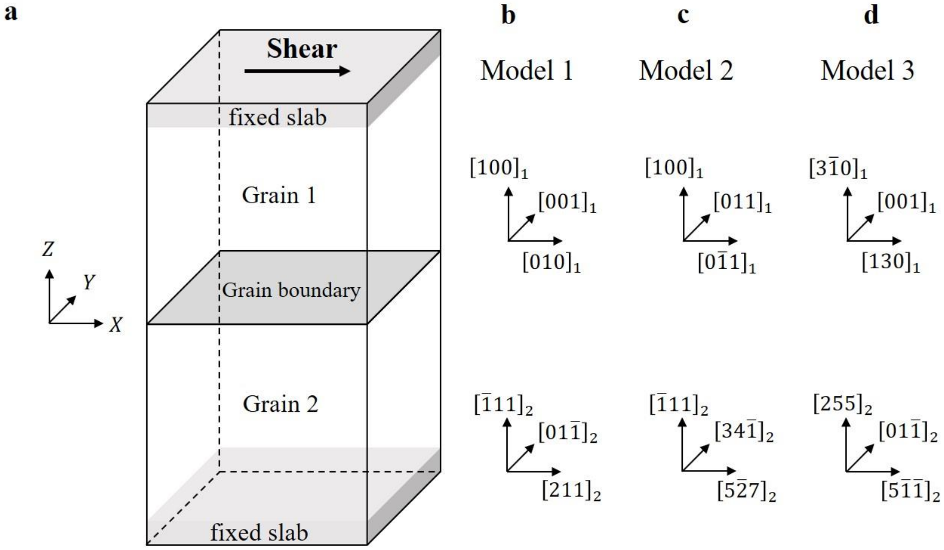
a
b
c
d
Shear
fixed slab
Grain 1
Grain boundary
Grain 2
fixed slab
Z
Y
X
Model 1
Model 2
Model 3
$[100]_1$
$[001]_1$
$[010]_1$
$[100]_1$
$[011]_1$
$[0\bar{1}1]_1$
$[3\bar{1}0]_1$
$[001]_1$
$[130]_1$
$[\bar{1}11]_2$
$[01\bar{1}]_2$
$[211]_2$
$[\bar{1}11]_2$
$[34\bar{1}]_2$
$[5\bar{2}7]_2$
$[255]_2$
$[01\bar{1}]_2$
$[5\bar{1}\bar{1}]_2$

Figure 3.6 Schematic (a) and crystallographic orientations (b-d) of the Au bicrystal models used in MD simulations.

In Chapter 6, an Au bicrystal containing a $(311)/(111)$ HAGB was constructed and the structural optimization was performed using the conjugate gradient method. Before bending deformation, the modelled bicrystal was equilibrated at 300K with a pressure of 0 bar for 20ps using the NPT MD simulations. The bending deformation was applied by controlling the rotation of the fixed thin slab with a thickness of 1 nm at the bottom of the bicrystal at an angular velocity of 0.05° ps^{-1} via the NVT ensemble.

The atomic structures of simulation results were analyzed using OVITO [148]. The common neighbor analysis modifier was used to identity the GB atoms (colored in white) and the atoms in the different crystal structures, i.e., the face-centered cubic, body centered cubic, and hexagonal close-packed crystal structures are colored in green, blue, and red, respectively.

Table 3.1 Applied strains, dimensions, and GB energy of bicrystal models

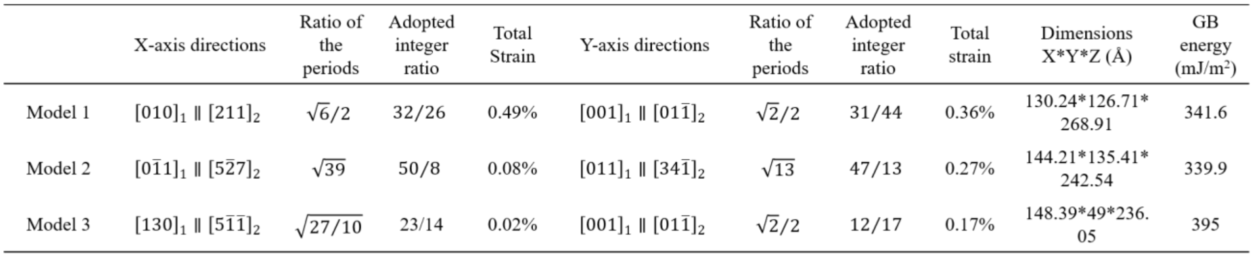

	X-axis directions	Ratio of the periods	Adopted integer ratio	Total Strain	Y-axis directions	Ratio of the periods	Adopted integer ratio	Total strain	Dimensions X*Y*Z (Å)	GB energy (mJ/m^2)
Model 1	$[010]_1 \parallel [211]_2$	$\sqrt{6}/2$	$32/26$	0.49%	$[001]_1 \parallel [01\bar{1}]_2$	$\sqrt{2}/2$	$31/44$	0.36%	130.24*126.71*268.91	341.6
Model 2	$[0\bar{1}1]_1 \parallel [5\bar{2}7]_2$	$\sqrt{39}$	$50/8$	0.08%	$[011]_1 \parallel [34\bar{1}]_2$	$\sqrt{13}$	$47/13$	0.27%	144.21*135.41*242.54	339.9
Model 3	$[130]_1 \parallel [5\bar{1}\bar{1}]_2$	$\sqrt{27/10}$	23/14	0.02%	$[001]_1 \parallel [01\bar{1}]_2$	$\sqrt{2}/2$	$12/17$	0.17%	148.39*49*236.05	395

4.0 Atomic-scale Observation of Dynamic Grain Boundary Structural Transformation during Shear-mediated Migration

This Chapter is based on our published work [149]. In this Chapter, the dynamic GB structural transformation during the shear-mediated migration of faceted tilt GBs will be revealed and the underlying atomistic mechanisms governing the transformation will be discussed. GB structural change is commonly observed during and after the stress-driven GB migration in nanocrystalline materials, but its exact transformation process at the atomic scale has not been explored experimentally. Here, employing in-situ high-resolution transmission electron microscopy combined with molecular dynamic simulations, we observed the dynamic GB structural transformation arising from reversible facet transformation and GB dissociation during the shear-mediated migration of faceted <110>-tilt GBs in Au nanocrystals. A reversible transformation was found to occur between $(002)/(111)$ and Σ11(113) GB facets, and be accomplished by the coalescence and detachment of $(\bar{1}\bar{1}1)/(002)$ type GB steps that mediated the GB migration. In comparison, the dissociation of $(002)/(111)$ GB into Σ11(113) and Σ3(111) GBs was accomplished via the reaction of $(111)/(11\bar{1})$ type steps that involved the emission of partial dislocations. It is further revealed that such transformations were loading-dependent and could be accommodated by GB junctions. This work provides atomistic insights into the dynamic structural transformation during GB migration.

4.1 Introduction

GB, as the ubiquitous interfacial structure in polycrystalline materials, influences greatly the properties and microstructural development of materials[150]. Grain growth and GB network evolution during plastic deformation in nanocrystalline materials has been widely reported [33, 34, 102, 151], wherein stress-driven GB migration is regarded as a major phenomenon[32]. Theoretical models, such as the dislocation glide mechanism for low-angle GBs[52, 53], the local conservative shuffling of atoms for high-angle GBs[152], and the unified disconnection-mediated mechanism[7, 153], have been proposed to describe the GB migration. However, these models do not consider the change of GB structure during and after the migration, which frequently happens in one of the most common GBs in polycrystalline materials, i.e., the asymmetrical tilt GBs (ATGBs)[154], especially in the GB with facets, and could affect their migration behaviors. For instance, Σ11 ATGBs[155] in Cu were found to show unique anisotropic mobility, which is associated with the transformation events at the facet nodes and incommensurate GB facets during the migration[156]. Although the shear coupling factor of ATGBs might be predicted based on the disconnection[7] or geometrical model[58, 59], there has been no direct experimental observation on the migration process or possible structural change at the atomic scale yet [7, 34, 35, 84, 105, 157].

The faceted morphology is a typical feature of ATGBs [154, 158], which are formed via GB facet transformation (also termed as GB faceting). Broadly speaking, GB faceting, dissociation, and structural phase transformation all belong to GB complexion transition, as they involve the change of GB structure units[93]. Previous studies have indicated that GB complex transition could affect GB migration. For example, GB faceting can significantly influence the thermally-induced ATGB migration[159, 160], GB structural phase transformation can facilitate

GB migration[161] or even alter the nature of GB migration[86], and the non-planar GB structure formed by GB dissociation shows unique mechanical responses[88, 162]. Nevertheless, experimental evidence on the dynamic GB structural transformation during shear-mediated migration is still lacking. Moreover, recent work revealed the absence of a correlation between GB velocity and curvature but a strong correlation between GB velocity and GB crystallography (e.g., misorientation and inclination) in Ni polycrystals[163], which further highlights the importance of investigating GB structural transformation during the migration and its impact on the kinetics of GB migration. With the help of the recently developed in-situ TEM platform[37], GB processing with controlled features and direct observation of the atomistic migration process under shear stress becomes attainable, which offers a great opportunity to explore this open area.

Here, in-situ interface processing with controlled crystal orientation and in-situ high-resolution transmission electron microscopy (HRTEM) shear testing were performed to study the ATGBs' migration behavior in gold (Au) nano bi-crystals. Two kinds of faceted ATGBs, which consist of $(002)/(111)$ATGB facets and $(\bar{1}\bar{1}1)/(002)$ or near $(111)/(11\bar{1})$ nanofacets were fabricated and studied. At equilibrium, $(002)/(111)$ATGB is a $[1\bar{1}0]$ tilt incommensurate GB with a misorientation angle of 54.74°, which is found to coexist with Σ11(113) STGB (with a misorientation angle of 50.48°)[164] or $(111)/(11\bar{1})$ GB (with a misorientation angle of 70.5°)[164, 165], and to be a common facet of Σ11 ATGB in face-centered cubic (FCC) metals[147]. A back-and-forth GB plane reorientation was observed during the migration process of the GB consisting of $(002)/(111)$ and $(\bar{1}\bar{1}1)/(002)$facets, which is attributed to the reversible facet transformation between the $(002)/(111)$ and $(\bar{1}\bar{1}1)/(002)$ ATGBs and the Σ11(113) STGB. Moreover, the dissociation of GB into a Σ11(113) STGB and a Σ3(111) STGB was found during the migration of the GB consisting of $(002)/(111)$and near $(111)/(11\bar{1})$ facets. The underlying atomistic mechanisms of these transformations were revealed with the atomistic molecular dynamic simulations. This work enriches our understanding of the atomistic migration mechanisms of high-angle ATGBs and offers direct evidence that dynamic GB structural transformation accommodates the stress-induced microstructural evolution in polycrystalline materials.

4.2 Experimental Results

4.2.1 Back-and-forth GB Plane Reorientation during Shear-mediated Migration

As shown in Figure 4.1a, a $[1\bar{1}0]$ tilt Au bi-crystal nano-junction with a diameter of ~10 nm and a misorientation angle of ~ 53.5° was fabricated by in-situ nano-welding inside a TEM. The as-fabricated GB is a faceted GB that consists of the $(002)_1/(111)_2$ ATGB facets and several interfacial defects (denoted as steps) connecting them (see section 4.2.3 for the identification of GB positions). The average GB plane has an inclination angle of ~11° to the $(002)_1/(111)_2$ ATGB. A closer observation of the core structure of these steps shows that they all have a height of one $(002)_1/(111)_2$ lattice spacing with $(\bar{1}\bar{1}1)_1$and $(002)_2$ planes as abutting planes (Figure 4.1i). Thereafter, these steps can be regarded as $(\bar{1}\bar{1}1)_1/(002)_2$ nanofacets to some extent. It is worth noting that these nanofacets accommodate the deviation of the misorientation angle of this bi-crystal from the ideal value of $(002)/(111)$ ATGB (i.e. 54.74°), the inclination of overall GB plane from the $(002)_1/(111)_2$ ATGB and the lattice misfit between $(002)_1$ and $(111)_2$ planes[166]. Similar structural features have also been observed in a Σ9 {221} tilt GB in copper, where ATGB facets are connected by steps or STGB facets [167]. A shear loading was then applied to the bottom grain of the bi-crystal (denoted as G2 in Figure 4.1a) at a constant rate (~0.001nm s^{-1}), and the loading direction (indicated by the white arrow in Figure 4.1a) was nearly parallel to the $(002)_1/(111)_2$ ATGB.

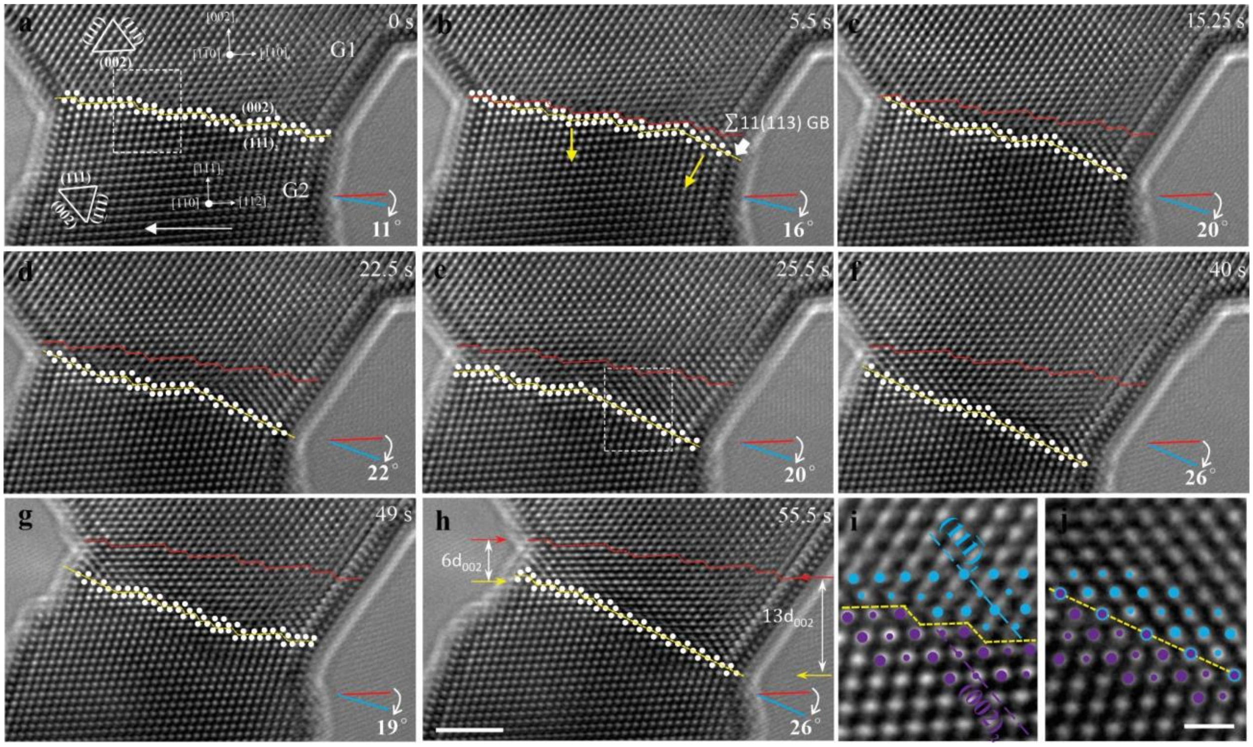

Figure 4.1 Stress-driven migration of a faceted grain boundary (GB) accompanied by back-and-forth GB plane reorientation and reversible facet transformation. (a) Structure of an as-fabricated Au bicrystal with a faceted GB consisting of $(\mathbf{002})/(\mathbf{111})$ ATGBs and several one-atomic-layer $(\bar{\mathbf{1}}\bar{\mathbf{1}}\mathbf{1})/(\mathbf{002})$ steps. The misorientation between the upper and bottom grains in this bicrystal is ~ 53.5°, close to the ideal misorientation angle (i.e., 54.74°) of $(\mathbf{002})/(\mathbf{111})$ ATGB. Shear stress nearly parallel to the $(\mathbf{002})/(\mathbf{111})$ ATGB was then applied to the bottom grain, as indicated by the white arrow. (b) The $(\mathbf{002})/(\mathbf{111})$ ATGB facets migrated via the lateral motion of $(\bar{\mathbf{1}}\bar{\mathbf{1}}\mathbf{1})/(\mathbf{002})$ steps until a Σ11 (113) STGB facet was formed at the right side of GB. The average GB plane has a clockwise rotation of ~5° during this process. The direction of GB migration is indicated by yellow arrows. (c) The $(\mathbf{002})/(\mathbf{111})$ ATGB and Σ11 (113) STGB facets migrated jointly until another STGB facet was formed at the left side of GB. Then the average GB inclination angle gradually increased to ~20°. (d-h) Sequential snapshots showing the back-and-forth GB plane reorientation and the reversible facet transformation between the STGB and the ATGB facets at the left end (d-f) and the right end (f-h) of GB in this bicrystal. The misorientation angle of the bicrystal in (h) is ~52.16°, indicating a slightly relative grain rotation during the deformation. (i, j) Closer observation of the core structure of $(\bar{\mathbf{1}}\bar{\mathbf{1}}\mathbf{1})/(\mathbf{002})$ steps and the structure of Σ11 (113) STGB. The red dash lines in (b-h) represent the initial position of the as-fabricated faceted GB. Scale bar: (a-h) 2 nm, (i,j) 0.5 nm

Under shear loading, some of the pre-existing steps began to move leftward along the $[\bar{1}\bar{1}2]$ direction of the bottom grain G2, causing the migration of the ATGB facets towards grain G2(Figure 4.1b). The migration behavior observed so far is similar to that of the disconnection-mediated GB migration reported in other studies[7, 37], except that a new GB facet, which is identified as an Σ11(113) STGB[168, 169], was formed at the right end of the GB in Figure 4.1b. The zoom-in view of the STGB facet and the superimposed schematic in Figure 4.1i confirms that the lattices at the two sides of this facet are in symmetrical relation to the (113) plane. Note that the serrated GB structure consisting of $(002)/(111)$ ATGB and Σ11(113) STGB facets has been observed in Au polycrystals before[170]. A slight clockwise rotation of the GB plane was found during this process, causing an increase in the average GB inclination angle (~5°). In the subsequent deformation, facet transformation and a back-and-forth GB plane reorientation were observed (Figure 4.1c-h). To quantify the GB plane reorientation and establish the relationship between the facet transformation and the back-and-forth GB plane reorientation, the average GB inclination angle and the normalized facet ratio are plotted as a function of time in Figure 4.2a. The change in the average inclination angle followed a “zig-zag” pattern with a minimum value of ~11° at the as-fabricated state and a maximum value of ~26°, which is close to the theoretical angle between (002) and (113) planes (i.e., 25.24°). The variation trend of the facet length ratio of Σ11(113) STGB is similar to that of the average inclination angle, while the $(002)_1/(111)_2$ ATGB and the steps exhibit the opposite trend (Figure 4.2a). This relation is further confirmed by the plot of the normalized facet length ratio versus inclination angle (Figure 4.2b). Specifically, the increase of the average inclination angle is associated with the ATGB-to-STGB facet transformation and subsequent STGB facet migration at the expense of ATGB facets (Figures 4.1b-d, 4.1e-f, 4.1g-h).

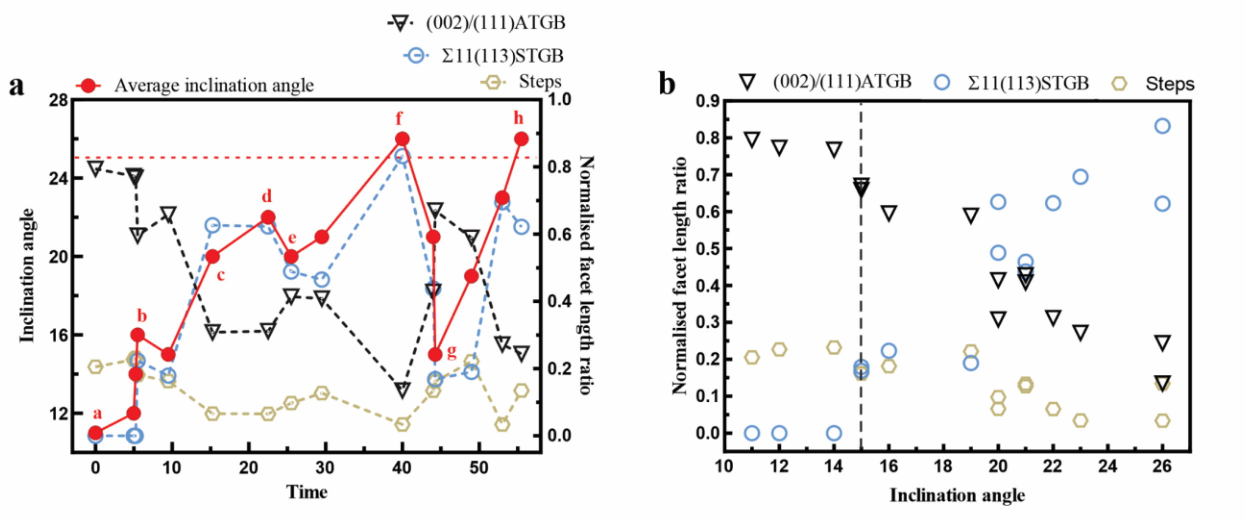

Figure 4.2 (a) Plots of the average GB inclination angle and the normalized facet ratio of the $(\mathbf{002})/(\mathbf{111})$ ATGB, the Σ11 (113) STGB and the $(\bar{\mathbf{1}}\bar{\mathbf{1}}\mathbf{1})/(\mathbf{002})$ steps versus time. (b) The plot of the normalized facet ratio versus average grain boundary inclination angle. The Σ11 (113) STGB facet exists only when the average inclination is larger than 15° (indicated by the dark dash line).

In contrast, the decrease in the average inclination angle is related to the backward facet transformation at either side of the GB (Figure 4.1d-e, 4.1f-g). The migration of the STGB facet is believed to follow the manner of nucleation and lateral motion of disconnections[37]. Moreover, two different dynamic processes were captured at the facet junctions of the ATGB and the STGB: one is that a one-layer ATGB step $((\bar{1}\bar{1}1)_1/(002)_2$nanofacet) was emitted from the facet node, causing the migration of the ATGB but keeping the STGB stationary (Figure 4.3a-b); The other is that the ATGB kept immobile but the STGB migrated several atomic layers (Figure 4.3b-d). These processes are likely to be attributed to the rearrangement of the localized atoms at the facet junctions. A slight grain rotation inevitably occurred during the shear loading, causing the misorientation angle of this bi-crystal to gradually decrease to ~52° in Figure 4.1g, which has accommodated the GB structural transformation during its migration (Figure 4.1a-h).

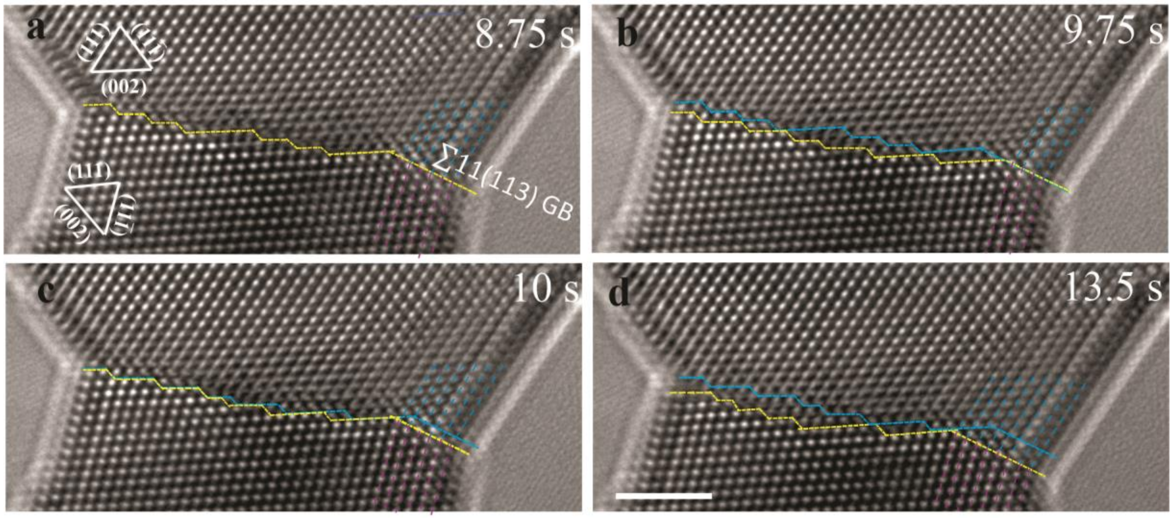

Figure 4.3 Sequential TEM snapshots showing the joint migration behaviors of the Σ11(113) STGB and the $(\mathbf{002})/(\mathbf{111})$ ATGB facets. (a) A faceted GB composed of the $(\mathbf{002})/(\mathbf{111})$ATGB, $(\bar{\mathbf{1}}\bar{\mathbf{1}}\mathbf{1})/(\mathbf{002})$ step and the Σ11(113) STGB. (b) A $(\bar{\mathbf{1}}\bar{\mathbf{1}}\mathbf{1})/(\mathbf{002})$ step emitted from the facet junction of $(\mathbf{002})/(\mathbf{111})$ATGB and Σ11(113) STGB. Σ11(113) STGB kept stationary. (c) Σ11(113) STGB migrated downwards while $(\mathbf{002})/(\mathbf{111})$ ATGB remained stationary. (d) Σ11(113) STGB kept migrating without $(\bar{\mathbf{1}}\bar{\mathbf{1}}\mathbf{1})/(\mathbf{002})$ step emitted from the facet junction. Scale bar: 2 nm

4.2.2 Reversible Facet Transformation between the ATGB and the STGB

As shown in Figure 4.1 and Figure 4.2, the facet transformation between the $(002)_1/(111)_2$ ATGB and the Σ11(113) STGB during the GB migration process were all accompanied by the annihilation or reappearance of $(\bar{1}\bar{1}1)_1/(002)_2$ steps connecting the ATGB facets. Therefore, it is suspected that these GB steps are highly involved in these processes. To verify this conjecture, a more detailed analysis of the atomistic deformation snapshots just before and after the formation of the STGB was conducted to explore the atomistic mechanism of ATGB-to-STGB transformation (Figure 4.4a-d). As shown in Figure 4.4a-c, a $(\bar{1}\bar{1}1)_1/(002)_2$ step was found to nucleate and laterally move along the GB until it met another step, causing the migration of ATGB towards the bottom grain. Afterward, those steps disappeared and were replaced by a

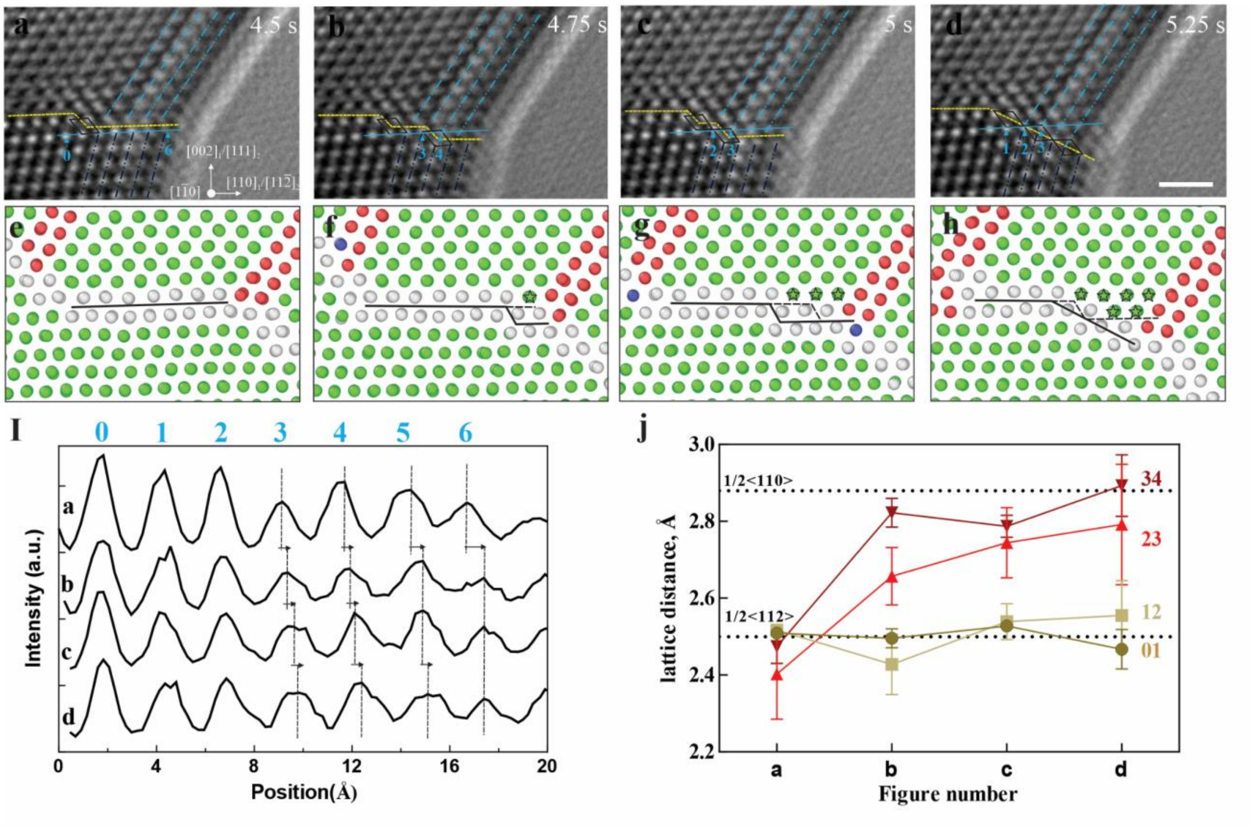

Figure 4.4 Atomistic mechanism of the $(\mathbf{002})/(\mathbf{111})$ ATGB to the Σ11(113) STGB facet transformation. (a) The $(\mathbf{002})/(\mathbf{111})$ATGB facets connected by a pre-existing $(\overline{\mathbf{11}}\mathbf{1})/(\mathbf{002})$ step. (b-d) Sequential snapshots showing the nucleation and lateral motion of another $(\overline{\mathbf{11}}\mathbf{1})/(\mathbf{002})$ step on the $(\mathbf{002})/(\mathbf{111})$ ATGB, and the formation of a Σ11(113) STGB facet at the right corner of GB. (e-h) Molecular dynamic (MD) simulation showing the same $(\mathbf{002})/(\mathbf{111})$ ATGB to Σ11(113) STGB facet transformation process as the experimental observation. In all MD simulation results, the green, red, and grey atoms indicate the face-centered cubic structure, hexagonal close-packed structure, and other coordination structure (i.e., GB structure), respectively. Dark dash lines in (f-h) represent the positions of GB in the previous snapshot. (i) The contrast intensity line profiles extracted from (a-d) at the same area as indicated by the blue solid line in (a). Atom columns are numbered from 0 to 6. J Plot of the lattice spacing between atom columns 0,1,2,3 and 4 in (a-d). Two dot lines indicate the ideal length of $\frac{1}{2}\langle\mathbf{110}\rangle$ (2.88 Å for Au) and $\frac{1}{2}\langle\mathbf{112}\rangle$ (2.5 Å for Au), respectively. Scale bar:1 nm

fully Σ11(113) STGB at the same area, where the lattices at both sides of the GB were in symmetrical relation about (113) plane (Figure 4.4d). Figure 4.4i shows the intensity profiles extracted along the blue solid lines in Figure 4.4a-d. The rightward shift of peaks in those intensity profiles indicates an increase of lattice spacing between the atom columns (numbered from 0 to 6) arising from the motion of the step. Tracking the change of spacing from columns 0 to 4 (denoted as 01,12,23, and 34), it is found that the lattice spacing of 01 and 12 fluctuated around 2.5Å (Figure 4.4j), which is the ideal value for $\left|\frac{1}{4}\langle 112\rangle\right|$ in Au. In contrast, the lattice spacing of 23 and 34 increased from ~2.5Å to ~2.88 Å (Figure 4.4j), the latter is the ideal value for $\left|\frac{1}{2}\langle 110\rangle\right|$ in Au. Such change in lattice spacing further confirms the $(111)_2$-to-$(002)_1$ plane transformation resulted from the motion of $(\bar{1}\bar{1}1)_1/(002)_2$ step. As shown in the trichromatic pattern in Figure 4.5, from the topological perspective, the $(111)_2$-to-$(002)_1$ plane transformation involves the movement of atoms both in and out of the projective plane (i.e., $(1\bar{1}0)$ plane), while only in-plane adjustment of localized atoms is needed to accomplish the steps-to-Σ11(113) STGB transformation.

Considering that HRTEM images are essentially phase-contrast images, deducing the position of the atoms at GBs from HRTEM images might bring some uncertainty. Hence, MD simulations were carried out to reproduce the facet transformation process and to validate that the motion and coalescence of $(\bar{1}\bar{1}1)_1/(002)_2$ steps led to the transformation. We constructed the "zig-zag" GB containing $\{002\}/\{111\}$ facets and traced its structural evolution under the shear deformation (see method). Note that stacking faults (SFs) exist at the as-constructed GB as a consequence of structural relaxation. The nucleation and subsequent motion of $(\bar{1}\bar{1}1)_1/(002)_2$ steps and the formation of a Σ11(113) STGB were captured at the "zig-zag" GB (Figure 4.4e-h), which agrees well with our experimental results and shows the formation of the STGB could be the product of the coalescence of $(\bar{1}\bar{1}1)/(002)$ type steps. It should be mentioned that the intersection of SF with GB in the simulations serves the same role as the intersection of free surface

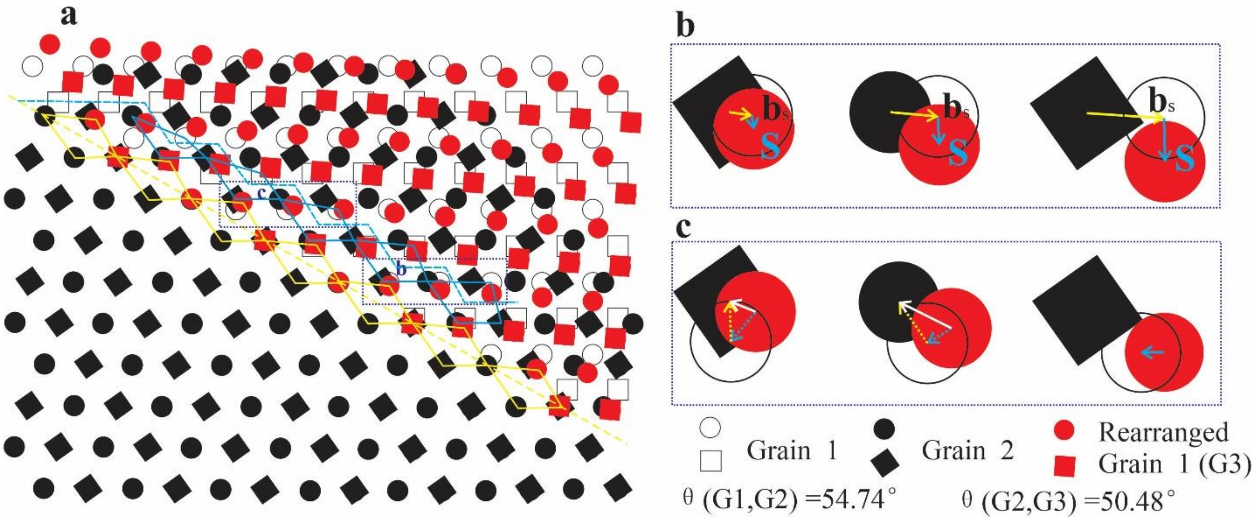

Figure 4.5 (a) Trichromatic pattern showing the rearrangement of the localized atoms during the reversible facet phase transformation between $(\mathbf{002})/(\mathbf{111})$ ATGB and Σ11(113) STGB, viewing direction is along <110>. The solid and hollow patterns indicate different {002} or {110} planes. The yellow dash line and rhombuses indicate the Σ11(113) STGB and its corresponding structure units, while the blue dash lines and irregular quadrilaterals indicate the stepped GB plane after the decomposition of Σ11(113) STGB and the core structures of those $(\bar{\mathbf{1}}\bar{\mathbf{1}}\mathbf{1})/(\mathbf{002})$ steps, respectively. (b) Selected area b to show the movement of atoms during the $(\mathbf{002})/(\mathbf{111})$ ATGB-to-Σ11(113) STGB facet phase transformation, the yellow arrows indicate the movement of atoms during the lateral motion of $(\bar{\mathbf{1}}\bar{\mathbf{1}}\mathbf{1})/(\mathbf{002})$ steps while the rearrangement of atoms along the blue arrows leads to the formation of Σ11(113) STGB. (c) Selected area c to show the movement of atoms leading to the backward facet phase transformation of Σ11(113) STGB into the $(\bar{\mathbf{1}}\bar{\mathbf{1}}\mathbf{1})/(\mathbf{002})$ steps and $(\mathbf{002})/(\mathbf{111})$ ATGB. The white solid arrows indicate the net movement of those atoms at the left side of this stepped GB, which could also be accomplished by the movement of atoms along with the blue and yellow dash arrows. The blue solid arrow indicates the movement of atoms at the right side of this stepped GB.

with the GB in the experiments since they both act as the nucleation sites of $(\bar{1}\bar{1}1)_1/(002)_2$ steps. A similar ATGB-to-STGB transformation was observed at the left side of the GB during the subsequent deformation in the experiment (not shown here). Moreover, the ATGB-to-STGB transformation via the coalescence of $(\bar{1}\bar{1}1)/(002)$ type steps are quite similar to the deformation faceting of Basal-Prismatic interface into the $\{10\bar{1}2\}$ twin boundary in hexagonal close-packed metals via the pile-up and relaxation of Prismatic-Basal type interfacial defects[137, 171, 172], wherein the deviation of the misorientation angle between the interfaces is also ~4°.

The as-formed Σ11(113) STGB did not always migrate jointly with the $(002)_1/(111)_2$ ATGB. It transformed back into the ATGB in some cases (Figure 4.6). Figure 4.6a shows a flat Σ11(113) STGB that was formed during the GB migration process. Under further shear loading, part of this STGB transformed into the serrated GB consisting of $(002)_1/(111)_2$ ATGB facets and $(\bar{1}\bar{1}1)_1/(002)_2$ steps (Figure 4.6b). These steps moved on the ATGB along the $[11\bar{2}]$ the direction of the bottom grain G2, causing the backward migration of ATGB towards the upper grain G1 and triggering the transformation of the rest of the STGB into the STGB (Figure 4.6c). Moreover, as shown in the intensity profiles in Figure 4.6g, a new intensity peak was found to emerge between peaks 4 and 5, indicating the appearance of a new atom column during the STGB-to-ATGB transformation. This change is believed to be caused by the $(002)_1$-to-$(111)_2$ plane transformation during the step motion since the structural repeat distance of $(002)/(111)$ATGB is ~1.88nm for Au, which means ~7 atomic columns in $(002)_1$ plane match ~8 atomic columns in $(111)_2$ plane as shown in Figure 4.6d. This process might involve the motion of kinks along the projection direction of the GB [105, 173] and warrants further study in the future. The change in alignment between the two grains is a direct consequence of the slight misorientation angle change during the transformation from 50.48° in the STGB to 54.74° in the ATGB, which is highlighted by the red dashed lines in Figure 4.6d. Additional analysis on the change of lattice spacing from column 2 to 6 (Figure 4.6h) further supports the $(002)_1$-to-$(111)_2$ plane transformation mediated by the motion of step: the lattice spacings of 23 and 34 in Figure 4.6a-c remain at the value of ~2.5Å, while the lattice spacing of 45 increases to a value far larger than 2.88 Å, and that of 56 fluctuates around 2.88 Å in Figure 4.6b (i.e., the formation of a step between atom columns 4 and

5). Then both of the lattice spacings of 45 and 56 dropped to ~2.5 Å in Figure 4.6c (i.e., the completion of $(002)_1$-to-$(111)_2$ plane transformation).

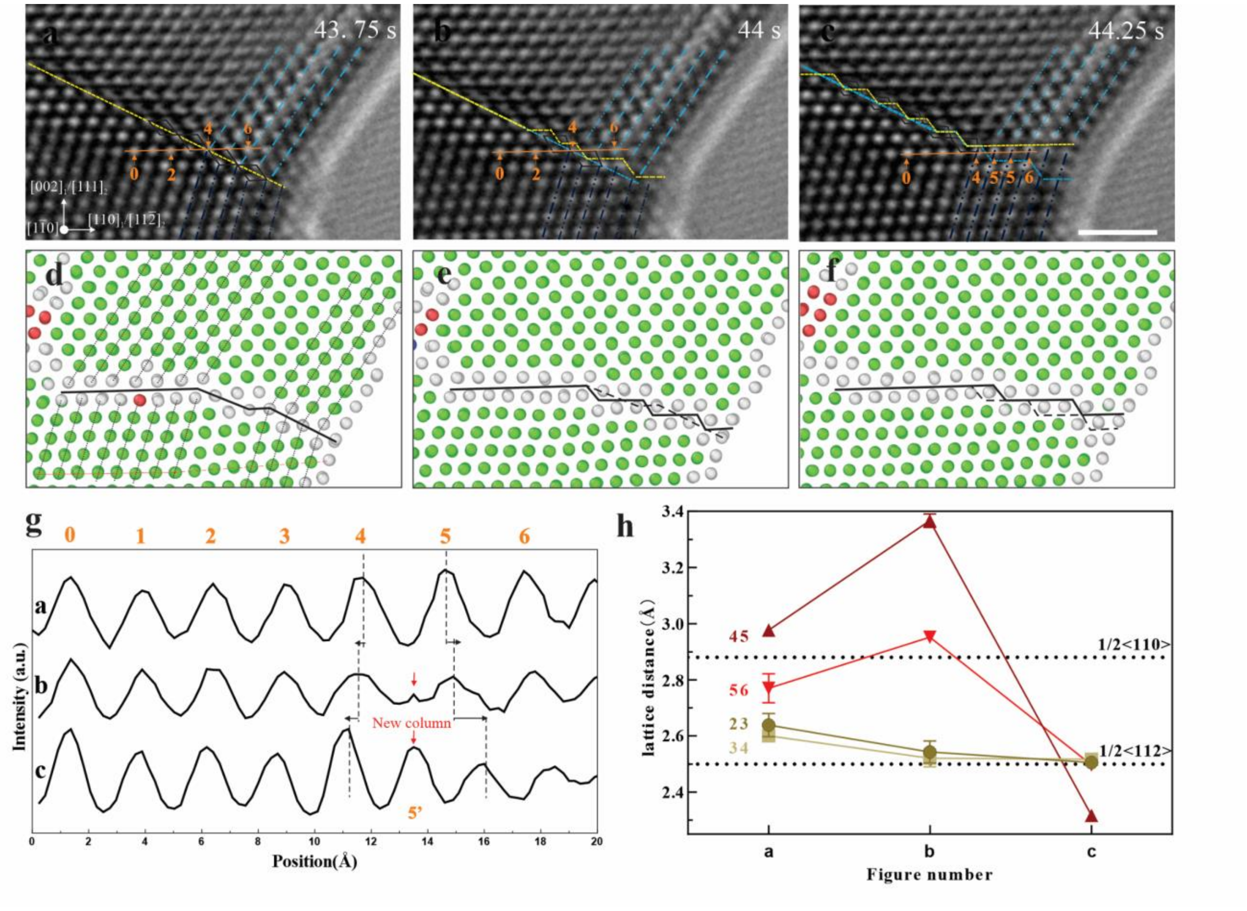

Figure 4.6 Atomistic mechanism of the backward facet transformation from the Σ11(113) STGB to the $(\mathbf{002})/(\mathbf{111})$ ATGB. (a) A long and flat Σ11(113) STGB facet, where the structure units are indicated by the rhombuses in the dark. (b) Part of the Σ11(113) STGB transformed into several $(\bar{\mathbf{1}}\bar{\mathbf{1}}\mathbf{1})/(\mathbf{002})$ steps connecting the $(\mathbf{002})/(\mathbf{111})$ ATGBs. (c) More $(\bar{\mathbf{1}}\bar{\mathbf{1}}\mathbf{1})/(\mathbf{002})$ steps were formed and GB migrated backward via the lateral motion of $(\bar{\mathbf{1}}\bar{\mathbf{1}}\mathbf{1})/(\mathbf{002})$ steps towards the free surface on the right. (d-f) Molecular dynamic simulation shows a similar backward facet transformation process as the experimental observation. Blue dash lines in (a, c) and dark dash lines in (e, f) represent the GB position in the last snapshot. (g) The contrast intensity line profiles extracted from (a-c) at the same area as indicated by the orange solid line in (a). Atom columns are numbered from 0 to 6. (h) Plot of lattice spacing between atom columns 2,3,4,5 and 6 in (a-d). Some error bars are too short to show in the plot. The lattice spacing of 45 and 56 in (c) means the average lattice spacing of 45' and 5'5, respectively. Scale bar 2 nm

This reversed facet transformation process was also observed in our MD simulations. As shown in Figure 4.6d, a disconnection was found on the STGB before the start of the transformation. Afterward, several step-connected $(002)_1/(111)_2$ ATGBs were formed and extended via the lateral motion of the steps (Figure 4.6e, f), which is consistent with our experimental results. It is worth mentioning that there is no appearance of new atom columns in the simulations because the movement of $(\bar{1}\bar{1}1)_1/(002)_2$ step in the simulations did not reach the structural repeat distance of $(002)_1/(111)_2$ ATGB[174].Topological analysis of the atomic motion during this process shows that the different movement behaviors of the neighboring atoms near the Σ11(113) STGB led to the facet transformation of the Σ11(113) STGB into the stepped $(002)_1/(111)_2$ ATGB (Figure 4.5c). A similar STGB-to-ATGB facet transformation was also observed at the other side of this bi-crystal (not shown here), which is believed to follow the same manner as described above. The reversed facet transformation and corresponding migration process should be in a metastable state during the GB migration process under this specific shear loading condition, as the GB migration direction is opposite to the overall migration direction of the entire process. Thereby, this reversed migration of $(002)_1/(111)_2$ ATGBs towards the upper grain G1 ceased soon and the GB migration returned via the lateral motion of $(\bar{1}\bar{1}1)_1/(002)_2$

steps along the $[\bar{1}\bar{1}2]$ direction of the bottom grain G2 or even transforming into the Σ11(113) STGB again (Figure 4.7).

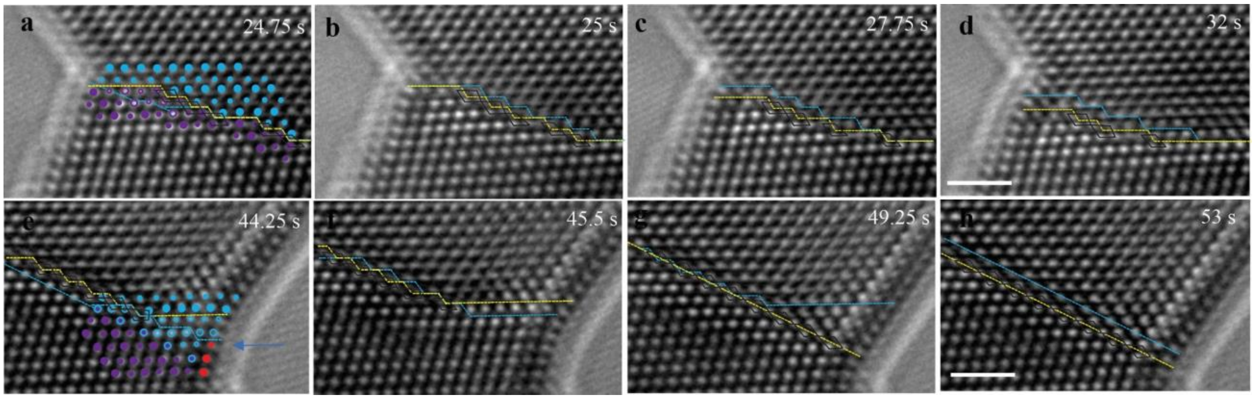

Figure 4.7 The motion behaviors of $(\bar{1}\bar{1}1)/(002)$ steps after decomposed from the Σ11 (113) STGB. (a) The steps moved rightwards first, then returned to their normal motion direction (leftwards) shortly. (b) Those steps are even transformed back into the Σ11 (113) STGB during the subsequent deformation. The blue and yellow dash lines indicate the position of the GB plane in the last snapshots and in the current state, respectively. Scale bar: 2 nm

4.2.3 Grain Boundary Dissociation during Migration

In addition to the faceted GB consisting of $(002)_1/(111)_2$ ATGB and $(\bar{1}\bar{1}1)_1/(002)_2$ steps as shown in Figure 4.1a, a $[\bar{1}10]$ tilt bi-crystal containing a faceted GB consisting of $(002)_1/(111)_2$ATGB and $(111)_1/(11\bar{1})_2$ facets were fabricated and tested (Fig. 4.8a). It is noted that there were several stacking faults (SFs) dissociated from the GB into grain 1 at the areas near the facet junctions, which might serve to accommodate the misorientation deviation of this bi-crystal from that of the ideal $(002)/(111)$ ATGB (i.e., 56° versus 54.74°)[155, 175]. Upon shearing, the $(111)_1/(11\bar{1})_2$ facets either decomposed into several $(111)_1/(11\bar{1})_2$ steps/nanofacets connecting the $(002)_1/(111)_2$ ATGBs or moved as a whole (Figure 4.8b, c), causing the migration of some ATGB facets. The pre-existing SFs seem to have little impact on the GB migration (Figure 4.8a, b) and even disappeared in the subsequent deformation (Figure

4.8c-f). One possible reason is that these SFs would contract into the GB before the movement of the $(111)_1/(11\bar{1})_2$ steps and even maintain the high-energy contracted state during the following migration [175].

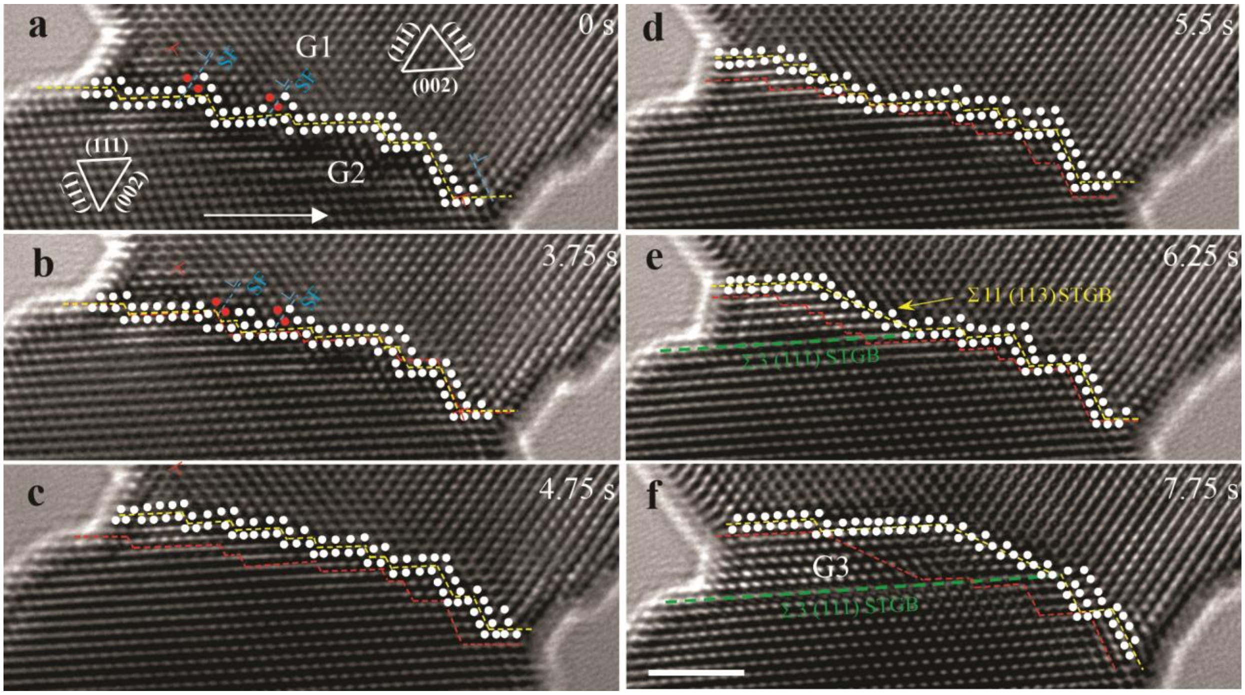

Figure 4.8 Shear-driven migration of another faceted GB coupled with GB dissociation. (a) The structure of an as-fabricated Au bicrystal with a faceted GB composed of $(\mathbf{002})/(\mathbf{111})$ ATGB and near $(\mathbf{111})/(\mathbf{11\bar{1}})$ GB facets. The misorientation angle between the upper and bottom grains in this bicrystal is ~ 56°. Shear stress nearly parallel to the $(\mathbf{002})/(\mathbf{111})$ ATGB facets was then applied to the bottom grain, as indicated with the white arrow. (b) The $(\mathbf{111})/(\mathbf{11\bar{1}})$ GB facets either decomposed into several one-atomic-layer $(\mathbf{111})/(\mathbf{11\bar{1}})$ steps or migrated via collective motion. (c) Further migration of the entire GB via the lateral motion of $(\mathbf{111})/(\mathbf{11\bar{1}})$ steps and collective motion of $(\mathbf{111})/(\mathbf{11\bar{1}})$ GB facets along the $(\mathbf{002})/(\mathbf{111})$ ATGB facets. (d) The $(\mathbf{111})/(\mathbf{11\bar{1}})$ steps nucleated at the free surface and moved into the bicrystal. (e) The faceted GB dissociated into a Σ11 (113) STGB and a Σ3 (111) STGB (or twin boundary (TB)). A sub-grain region (Grain 3) was then formed. (f) The sub-grain grew via the extension of $(\mathbf{002})/(\mathbf{111})$ ATGB facets and the migration of Σ11 (113) STGB. In figures (a-f), the yellow and the red dash lines represent the current position of mixed GB and their previous position in the last frame, and the green dash lines represent the newly formed Σ3 (111) STGB. Scale bar: 2nm

Moreover, new $(111)_1/(11\bar{1})_2$ steps were nucleated at the free surface to facilitate the GB migration (Figure 4.8d). More interestingly, a sub-grain (denoted as Grain 3) was then formed and bounded by a $(002)_1/(111)_3$ ATGB, the left-side free surface, and two newly-formed GBs (Figure 4.8e). These two GBs are identified as Σ11(113) STGB (between Grain 1 and Grain 3) and Σ3(111) STGB (between Grain 2 and Grain 3), which are both dissociated from the original faceted GB. The following growth of the sub-grain was via the extension of the $(002)_1/(111)_3$ ATGB and the migration of the Σ11(113) STGB (Figure 4.8f). A slight grain rotation occurred during this shear deformation, causing the misorientation angle to gradually increase to ~ 58°. Additionally, the misorientation angle between Grain 1 and Grain 3 is ~51.5°, close to that in Figure 4.1g and within the range of 50.48° to 54.74° (i.e., the misorientation angles for ideal Σ11(113) STGB and $(002)/(111)$ ATGB). Therefore, it is not surprising to observe a serrated GB consisting of $(002)_1/(111)_3$ ATGB and Σ11(113) STGB facets between Grain 1 and Grain 3.

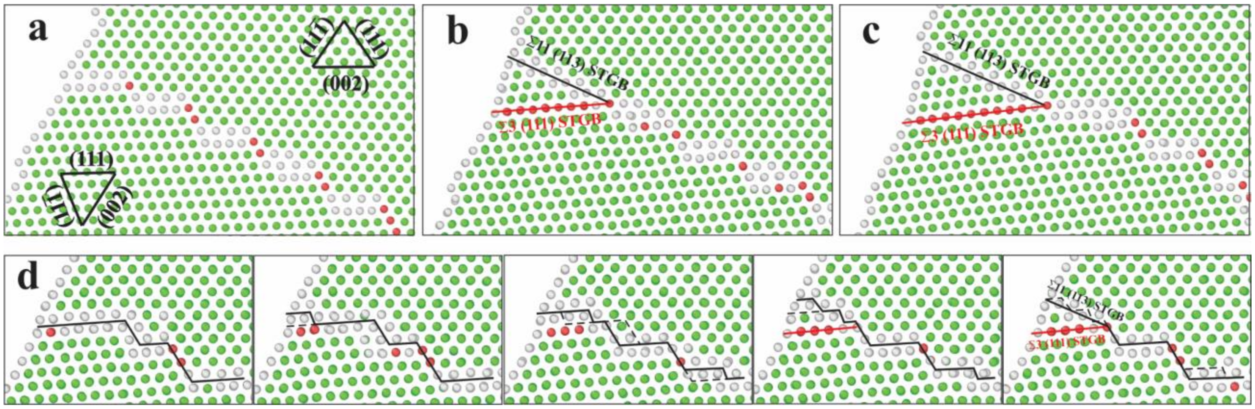

Figure 4.9 Molecular dynamic simulations showing the GB dissociation during the migration of the faceted GB. (a-c) Sequential snapshots of simulation results showing the same process as experimental observation in Figure 4.8 of the formation and growth of a sub-grain during the migration of a faceted GB consisting of $(\mathbf{002})/(\mathbf{111})$ ATGB and $(\mathbf{111})/(\mathbf{11\bar{1}})$ GB facets. (d) Detailed MD simulation results showing the dynamic GB dissociation process of the $(\mathbf{002})/(\mathbf{111})$ ATGB into a Σ 11 (113) STGB and a Σ3 (111) STGB.

Similar to the $(002)_1/(111)_2$ ATGB to Σ11(113) STGB facet transformation in Figure 4.4, the GB dissociation, in this case, is highly related to the coalescence of steps connecting the $(002)_1/(111)_2$ ATGB facets (Fig. 4.8d, e), except that these steps are of $(111)_1/(11\bar{1})_2$ type.

Although the Σ11(113) STGB was formed in both cases, the underlying mechanisms are believed

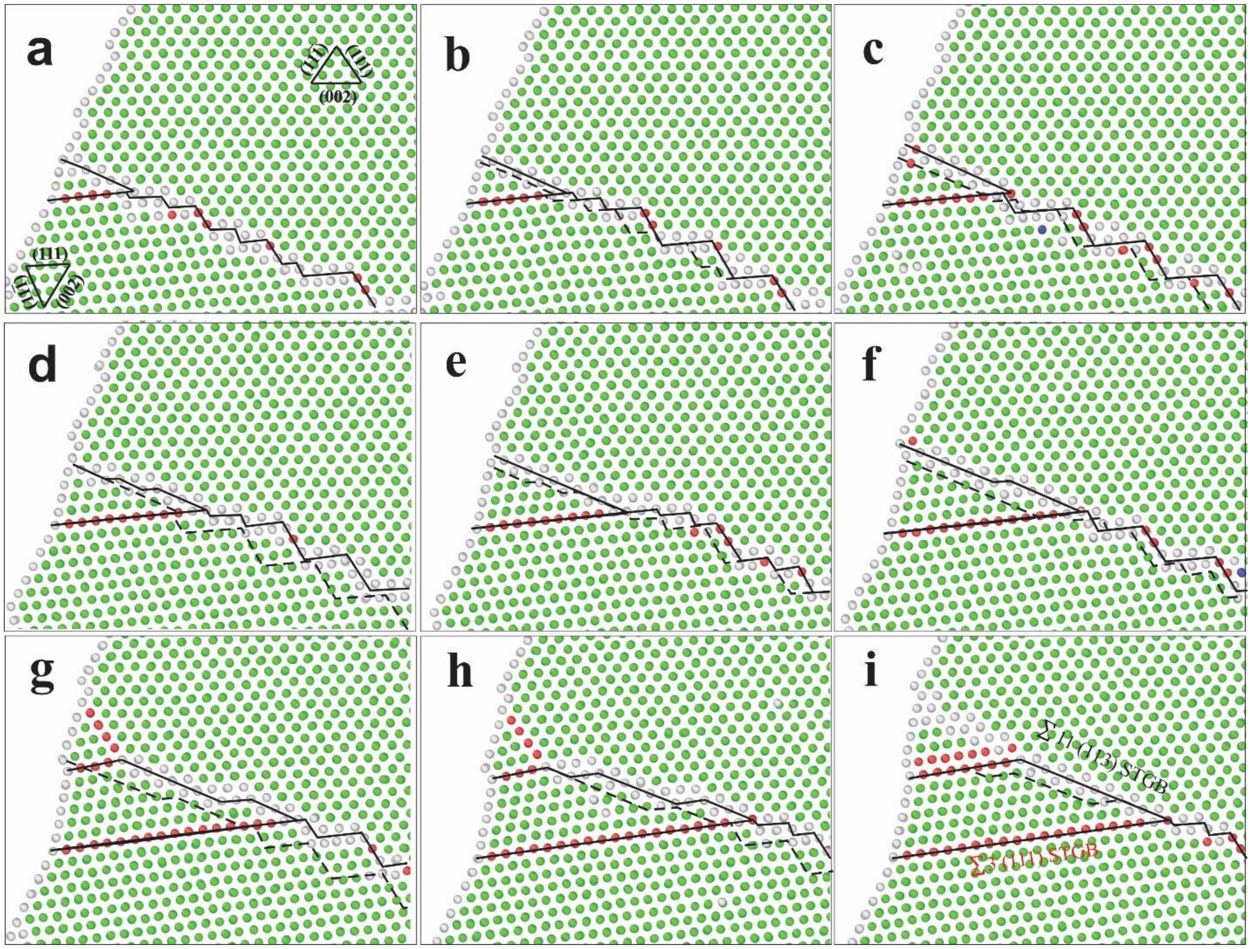

Figure 4.10 Sequential snapshots of MD simulations showing the GB migration assisted by the motion of a GB triple-junction. The GB triple-junction is the intersection point of Σ11(113) STGB, Σ3(111) STGB, and the original serrated GB consisting of $(\mathbf{002})/(\mathbf{111})$ ATGB and $(\mathbf{111})/(\mathbf{11\bar{1}})$ steps. Disconnections of Σ11(113) STGB and $(\mathbf{111})/(\mathbf{11\bar{1}})$ steps emitted from the GB triple-junction to assist GB migration (d-i). The solid dark lines indicate the current position of the GB plane while the dash dark lines mean the previous position of the GB plane in the last snapshot.

to be different and Shockley partial dislocations are expected to be involved in the formation of Σ3(111) STGB during the GB dissociation process. To explore the atomistic mechanism, MD simulations were carried out to reproduce this GB migration and dissociation process. The nucleation and growth of a sub-grain, which is enclosed by an Σ11(113) STGB and a Σ3(111) STGB that were dissociated from the original GB structure during the migration process, was captured (Figure 4.9a-c). Specifically, the GB dissociation process is not a one-step event. The formation of Σ3(111) STGB was found to be accompanied by the nucleation and motion of $(111)_1/(002)_3$ steps on the $(002)_1/(111)_3$ ATGB facet. Afterward, those $(111)_1/(002)_3$ steps coalesced and transformed into a Σ11(113) STGB (Figure 4.9d), the same as that in Figure 4.4. Additionally, the sub-grain growth is assisted by the motion of triple-junction, where the Σ3(111) STGB keeps stationary but the Σ11(113) STGB and the rest of the original serrated GB moved roughly rightward (Figure 4.10).

4.3 Discussion

GB faceting is believed to be a process to minimize the total GB free energy[176]. As a prevalent type of GB in polycrystalline materials, ATGBs are normally found to facet into low-energy STGBs or facets with at least one {111} low-index plane on two sides of the GB in face-centered cubic (FCC) metals[164, 176]. In our results, $(002)/(111)$ ATGB is found to mainly combine with $(\bar{1}\bar{1}1)/(002)$ATGB, $(111)/(11\bar{1})$ GB or Σ11(113) STGB to form a faceted GB structure. It is noted that $(111)/(11\bar{1})$ GB (i.e., coherent twin boundary) and Σ11(113) STGB are the two lowest-energy GBs among [110] tilt GBs, while $(002)/(111)$ ATGB has slightly higher energy than the Σ11(113) STGB[147]. During the shear loading, the two different types of faceted GB structure would undergo dynamic GB structural transformation, and both transform into the faceted GB consisting of $(002)/(111)$ ATGB and Σ11(113) STGB, either via the direct facet transformation (Figure 4.1) or GB dissociation (Figure 4.8).

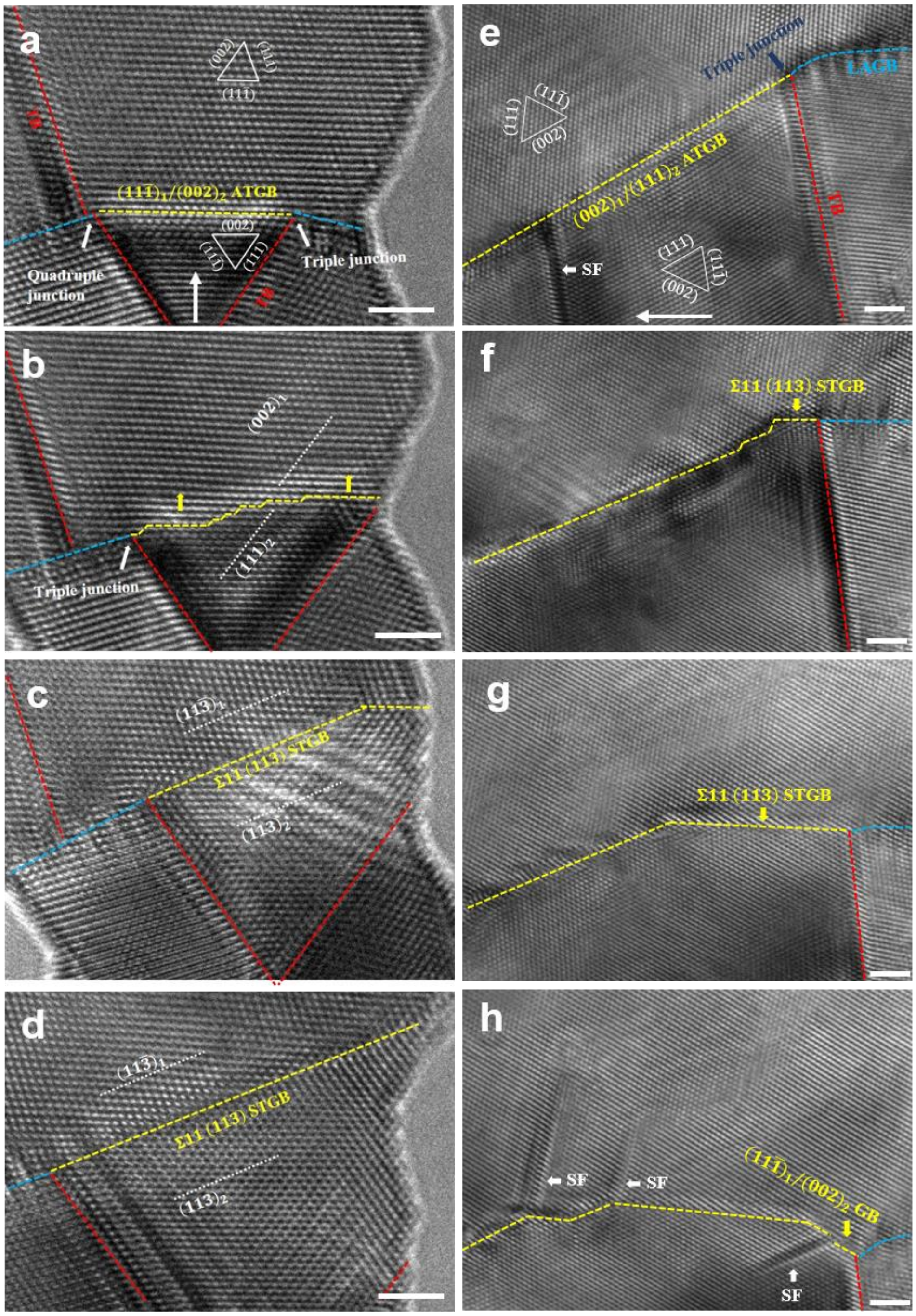
a
(002)
(111)
(111)
TB
$(11\bar{1})_1/(002)_2$ ATGB
(002)
(111)
(111)
Quadruple junction
Triple junction
TB
b
$(002)_1$
$(111)_2$
Triple junction
c
$(113)_1$
Σ11 (113) STGB
$(113)_2$
d
$(113)_1$
Σ11 (113) STGB
$(113)_2$
e
Triple junction
LAGB
(111)
$(11\bar{1})$
(002)
$(002)_1/(111)_2$ ATGB
TB
SF
(111)
$(11\bar{1})$
(002)
f
Σ11 (113) STGB
g
Σ11 (113) STGB
h
SF
SF
$(11\bar{1})_1/(002)_2$ GB
SF

Figure 4.11 Transformations of $\{002\}/\{111\}$ type ATGB into Σ11 (113) STGB under different loading conditions. (a-d) A flat $(\mathbf{11\bar{1}})/(\mathbf{002})$ ATGB bounded by two GB junctions transformed into the Σ11 (113) STGB under the compressive loading perpendicular to the ATGB. Similarly, the ATGB-to-STGB transformation is via the

nucleation and coalescence of $(\mathbf{002})/(\mathbf{111})$ steps. (e-h) $(\mathbf{002})/(\mathbf{111})$ ATGB-to- Σ11 (113) STGB transformation started from a GB triple junction. Shear loading with an inclination angle of ~30° was applied as indicated by the white arrow. Scale bar: 2 nm

Regarding the reversible facet transformation that occurred between $(002)/(111)$ ATGB and Σ11(113) STGB during the migration of faceted GB containing $(002)/(111)$ and $(\bar{1}\bar{1}1)/(002)$ facets (Figure 4.1). It is now clear that the ATGB-to-STGB facet transformation can be accomplished through the coalescence of $(\bar{1}\bar{1}1)/(002)$ steps (Figure 4.4) while the backward STGB-to-ATGB transformation happens via the detachment of $(\bar{1}\bar{1}1)/(002)$ steps from the STGB and the subsequent motion of these steps (Figure 4.6). The specific shear loading parallel to the $(002)_1/(111)_2$ ATGB in our experiment (Figure 4.1) seems to propel the transformation: on the one hand, it promotes the nucleation and motion of $(\bar{1}\bar{1}1)/(002)$ steps. Those steps are necessary for the ATGB-to-STGB transformation; on the other hand, it has a large inclination angle (~25°) with the as-formed STGB facets, making those STGB facets easy to decompose back into steps during subsequent migration. To better understand the influence of loading conditions on the facet transformation, we examined the mechanical responses of $(002)/(111)$ ATGB and Σ11(113) STGB under different loading conditions. The ATGB is found to easily transform to STGB under all tested loading conditions, including compressive loading perpendicular to the ATGB (Figure 4.11a-d), shear loading with an inclination angle of ~30° from the ATGB (Figure 4.11e-h), and shear loading nearly parallel to the ATGB as shown in Figure 4.1. The strong tendency of ATGB-to-STGB transformation is possible because it is a thermodynamically energy-favorable process. In comparison, whether the STGB-to-ATGB transformation happens or not depends on the angles between the shear loading and the STGB. Only when the angle is larger than ~14° (Figure 4.13), obvious STGB-to-ATGB transformation was observed during the migration (Figure 4.12i-p). Otherwise, the mechanical response of STGB would be simply disconnection-mediated migration[37] (Figure 4.12a-h). Likely, the relative magnitude of resolved shear stress on the STGB plane and the ATGB plane determines

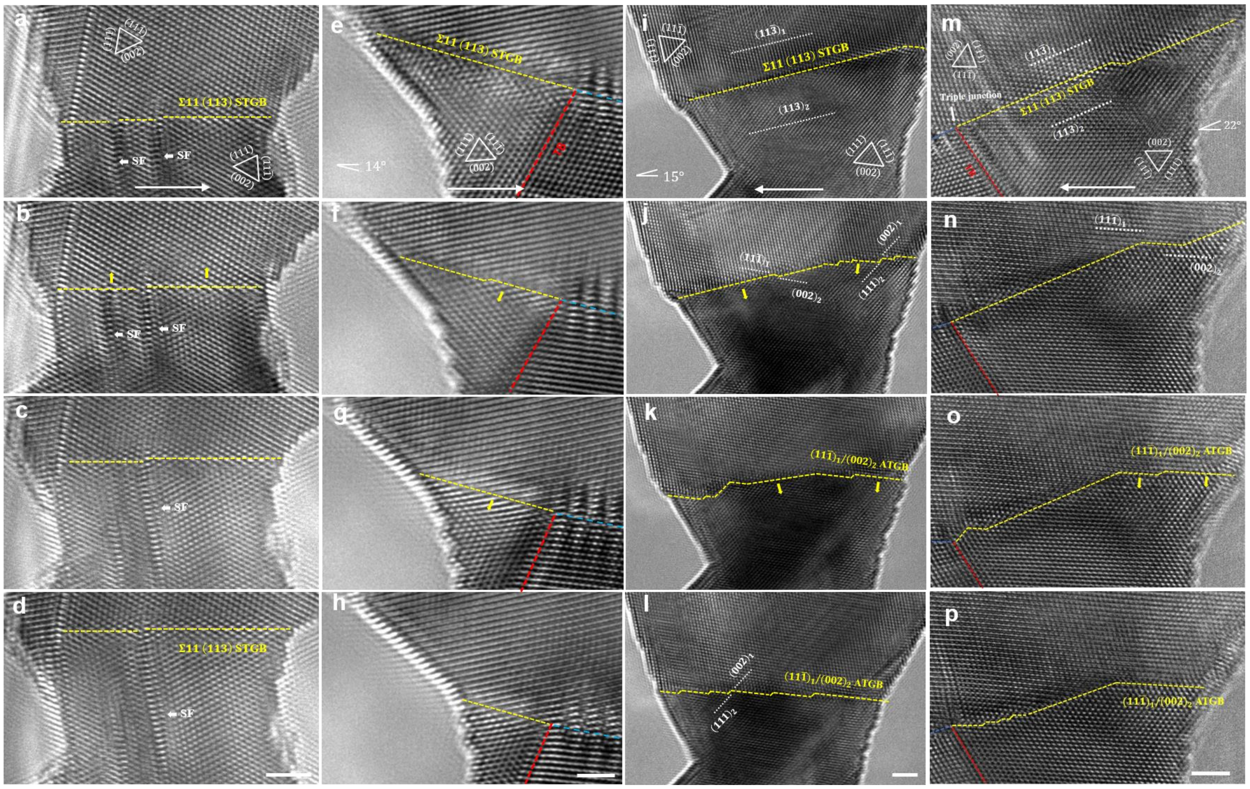

Figure 4.12 The loading-direction-dependence of Σ11 (113) STGB-to-$\{002\}/\{111\}$ ATGB transformation. (a-h) Conservative migration of Σ11 (113) STGB mediated by disconnections. Shear loading was near parallel (a-d) or had an inclination angle of ~14° (e-h) to the STGB, as indicated by the white arrow in (a,e). (i-p) STGB-to-ATGB transformation occurred when the STGB had an inclination angle of ~15° (i-l) or ~22° (m-p) with the shear loading direction. Scale bar: 2nm

whether the STGB-to-ATGB would happen, as the critical angle of ~14° is close to the half of the angle between STGB and ATGB (i.e., 25.2°). It needs to mention that the critical angle of loading dependence was determined in bi-crystals without the constraints from neighboring grains. In nanograined materials, the stress/strain state in the local region could be different from the external loading, thus the critical angle could be different.

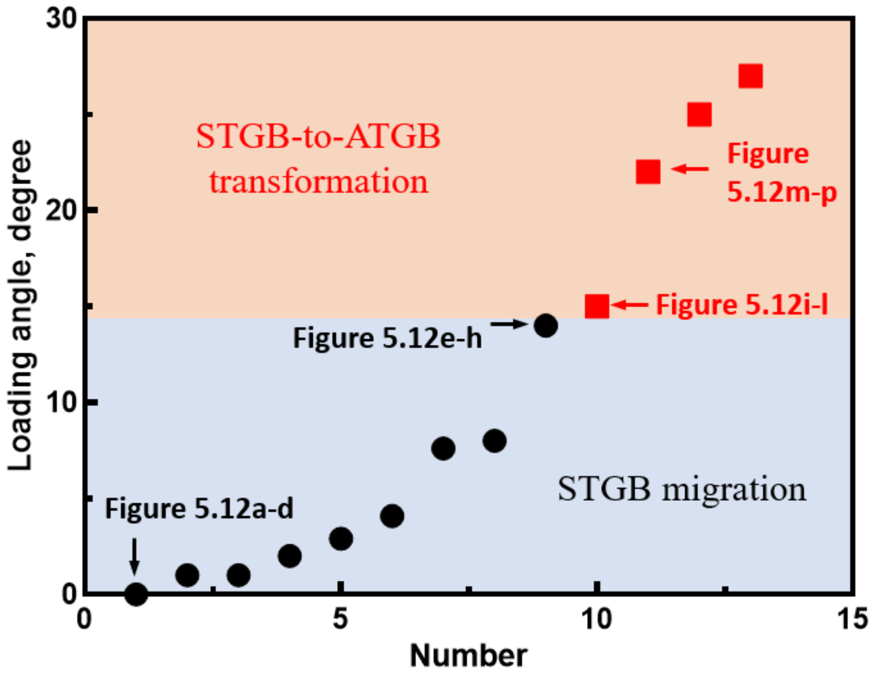

Figure 4.13 Plot of loading angle between STGB and applied shearing versus the experimental number. Black balls indicate the disconnection-mediated migration of STGB, while red cubes mean the STGB-to-ATGB transformation happened during the migration process.

We notice that the reversible facet transformation essentially starts from a faceting/de-faceting process at the atomic scale if we treat those steps as $(\bar{1}\bar{1}1)/(002)$ nanofacets (Figure 4.1i). Specifically, the ATGB-to-STGB facet transformation corresponds to a de-faceting process of a faceted GB consisting of equal-length $(002)/(111)$ and $(\bar{1}\bar{1}1)/(002)$nanofacets into a complete Σ11(113) STGB and the backward facet transformation is a faceting process starting from the STGB into the same faceted GB (Figure 4.14i). Revisiting the simulation results, we found that such faceting/de-faceting transformations took place frequently (Figure 4.14a-h) and should be a general phenomenon between Σ11(113) STGB and $(002)/(111)$ type nanofacets. More interestingly, this faceting/de-faceting process is analogous to the nucleation and annihilation of disconnection dipoles on Σ11(113) STGB (Figure 4.14j), as all the single-layer, double-layer, or four-layer disconnections reported in the literature contain the $(\bar{1}\bar{1}1)/(002)$ type nanofacets[37]. Hence, the loading condition dependence of STGB-to-ATGB transformation can be well explained: The external loading influences whether the $(\bar{1}\bar{1}1)/(002)$ nanofacets form after initial faceting moves on the Σ11(113) STGB or on the $(002)/(111)$ ATGB, which consequently determines if the Σ11(113) STGB undergoes the conservative migration (Figure 4.12a-h, Figure 4.14j) or the STGB-to-ATGB facet transformation (Figure 4.12i-p, Figure 4.14k).

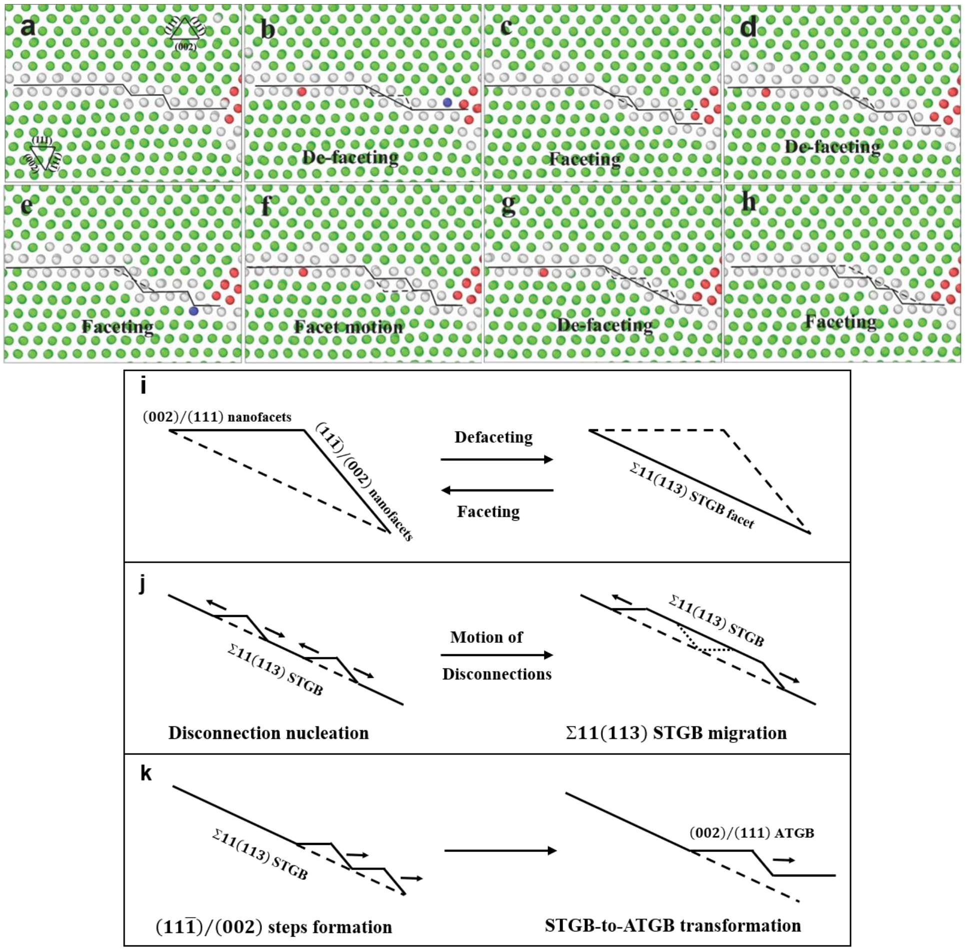
a
(002)
(111)
b
De-faceting
c
Faceting
d
De-faceting
e
Faceting
f
Facet motion
g
De-faceting
h
Faceting
i
(002)/(111) nanofacets
$(11\bar{1})/(002)$ nanofacets
Defaceting
Faceting
Σ11(113) STGB facet
j
Σ11(113) STGB
Motion of
Disconnections
Σ11(113) STGB
Disconnection nucleation
Σ11(113) STGB migration
k
Σ11(113) STGB
(002)/(111) ATGB
$(11\bar{1})/(002)$ steps formation
STGB-to-ATGB transformation

Figure 4.14 Atomistic mechanisms of the loading-direction-dependence of STGB-to-ATGB transformation. (a-h) MD simulation snapshots showing the frequent faceting/de-faceting transformation between the $\{\mathbf{002}\}/\{\mathbf{111}\}$ type nanofacets and the Σ11 (113) STGB. (i) Schematic illustration showing the faceting/de-faceting transformation. (j) Disconnection-mediated migration of Σ11 (113) STGB after initial faceting (i.e., nucleation and motion of

disconnection dipoles). (k) STGB-to-ATGB transformation via the motion of $(\mathbf{11\bar{1}})/(\mathbf{002})$ steps formed after initial faceting.

It is also noticed that the reversible facet transformation predominately occurred at the region near the edge free surface in our nano bi-crystals due to the lack of constrains (Figure 4.1). The edge free surface acts as the nucleation source of steps (Figure 4.4b) and accommodates the mutual transition between Σ11(113) STGB and $(002)/(111)$ ATGB (Figure 4.4a-d, Figure 4.6a-c). In polycrystalline materials, other nucleation sources and strain accommodation mechanisms are needed. As shown in Figure 4.11 and Figure 4.12m-p, GB junctions [37, 72] that commonly exist in polycrystalline materials can be effective sites that promote the nucleation of $(\bar{1}\bar{1}1)/(002)$ steps, and coordinate the ATGB-to-STGB (Figure 4.11) and the STGB-to-ATGB transformations (Figure 4.12i-p). The GB facet junction [106] and the intersection of stacking fault with GB (as evidenced by the simulation results in Figure 4.4e-h) can also play a similar role as GB junctions in polycrystalline materials. Moreover, only very localized atom adjustment is needed to accommodate the facet transformation (Figure 4.3, Figure 4.4, and Figure 4.5), which could be sufficiently accommodated by the lattice distortion of grains in polycrystalline materials. Given that Σ11(113) STGB and (002)/(111) ATGB are found to be preserved as much as possible in the GBs vicinal to these special geometrics, such as 52.9° [110] tilt GB[164], and GB faceting is also prevalent in various types of GBs[177, 178], it is thus reasonable to believe that the faceting/de-faceting process and resultant facet transformation mechanisms discussed here could have a general implication to the understanding of the structural evolution of faceted GBs during stress-driven migration in nanocrystalline or polycrystalline materials.

For the faceted GB constructed by $(002)/(111)$ ATGB and near $(111)/(11\bar{1})$ GB facets, GB dissociation, instead of direct facet transformation, was found during the migration process (Figure 4.8 and Figure 4.9). This distinction is originated from the different core structures of the steps in these two types of faceted GBs. In other words, there is no low-energy interface comparable to the Σ11(113) STGB that can be formed via the direct coalescence of $(111)/(11\bar{1})$ steps or de-faceting process in this case. Consequently, this kind of faceted GB tends to dissociate into the two lower-energy interfaces, i.e., Σ11(113) STGB and Σ3(111) STGB, during the migration process. Additionally, this GB dissociation behavior can be interpreted based on the coincidence site lattice (i.e., CSL) GB model. In cubic polycrystals, CSL GBs are classified by a Σ value, which means the reciprocal coincidence site density and the dissociation of CSL GBs are believed to follow the so-called "Σ combination rule"[179]. For instance, $\Sigma27 \rightarrow \Sigma3 + \Sigma9$ and $\Sigma9 \rightarrow \Sigma3 + \Sigma3$[180]. In our case, the faceted GB has a misorientation angle of ~58°, very close to the ideal value of Σ33 GB (i.e. 59°)[164]. Therefore, the GB dissociation reaction here is essential: Σ33 faceted GB → Σ3(111) STGB + Σ11(113) STGB. It should be mentioned that the existence of the free surface might promote GB dissociation[181] but it is not an indispensable condition because the GB dissociation behavior also happens in a restricted environment (i.e., region away from the free surface, not shown here), and shear-coupled GB migration accompanied by the formation of twins is also common during the deformation of FCC polycrystals[103]

Moreover, our findings may provide a plausible atomistic understanding of the co-increased proportion of Σ11 and Σ3 GB after the cyclic deformation of nanocrystalline FCC metals[102], as any ATGBs with a misorientation angle vicinal to 54.74° could contain the $(002)/(111)$ facets in their GB structure, which would directly transform into the Σ11(113) STGB (Figure 4.4) or dissociate into a Σ11(113) STGB and a Σ3(111) STGB (Figure 4.8) during the stress-driven GB migration process. Furthermore, our work enriches the understanding of the complexity of GB migration, as it clearly shows that GB structure is in a metastable state during the migration, where mutual transformations occur between the stable GB facets such as

$(002)/(111)$ type ATGBs, Σ11(113) STGB, and Σ3(111) STGB. Such transformations would cause a change in GB crystallography (i.e., misorientation and inclination) and affect the direction and speed of GB migration. In our case, the Σ11 (113) STGB migrates faster than the $(002)/(111)$ ATGB, which is supported by our observations that the right part of the GB moved more atomic layers than its left part in Figure 4.1a-h and the width of the sub-grain grows much faster than its height in Figure 4.8e-f. The dynamic GB structural transformation during the migration process and the resulting migration speed discrepancies between different GB facets may be the reason for stress-driven directional fast grain growth in nanocrystalline metals[31, 33, 34]. In addition, our work emphasizes the importance of the faceting/de-faceting mechanism on GB migration and facet transformations, thus could serve a role to bridge the disconnection-mediated GB migration and the GB structural transformation resulting from GB complexion transition.

4.4 Conclusion

In conclusion, the dynamic GB structural transformations during the stress-driven migration of two different faceted ATGBs both containing $(002)/(111)$ facets have been revealed using the in-situ HRTEM technique combined with MD simulations. A low-energy Σ11(113) STGB was found to form in both cases, via either facet transformation or GB dissociation. The core structure of steps, $(\bar{1}\bar{1}1)/(002)$ type or $(111)_1/(11\bar{1})_2$ type, connecting the $(002)/(111)$ facets determine which pathway it tends to follow. In addition, the facet/de-faceting transformation between Σ11(113) STGB and $(002)/(111)$ type nanofacets appears to be the origin of the reversible facet transformation. Whether the Σ11(113) STGB after initial faceting would migrate conservatively or transform into the $(002)/(111)$ ATGB depends on the loading condition. Given that any GBs vicinal to these two special geometrics potentially have a GB structure similar to what we have observed and GB faceting is commonly observed in various types of GBs, the GB structural transformation mechanisms proposed here should have a general implication to the deformation-induced GB structural evolution of faceted GBs. The discovery of dynamic GB structural transformation during the shear-mediated migration will enrich our understanding of the complexity of GB migration and have an impact on the development of nanocrystalline materials with microstructure control through thermal-mechanical processing.

5.0 Revealing Shear-coupled Migration Mechanism of a Mixed Tilt-twist GB at Atomic Scale

This Chapter is based on our published work[182].In this Chapter, the shear-coupled migration behavior of typical mixed tilt-twist grain boundaries will be investigated. Shear-coupled GB migration greatly influences the plasticity and creep resistance of nanocrystalline materials. However, the atomistic mechanisms underlying the shear-coupled migration of general mixed tilt-twist GBs (MGBs) remain largely elusive to date. Here, using in-situ HRTEM and MD simulations, we uncover the atomic-scale migration behavior of a typical MGB, i.e., $\langle 001\rangle\{200\}/\langle 0\bar{1}1\rangle\{\bar{1}11\}$ GB, during the room-temperature shear deformation of Au nano-bicrystals. Two distinct migration patterns showing the opposite signs of shear-coupling factor were observed and further revealed to be mediated by the motion of GB disconnections with different crystallographic parameters and exhibit different lattice correspondence relations, i.e., $\langle 001\rangle\{020\}$-to-$\langle 0\bar{1}1\rangle\{200\}$ and $\langle 001\rangle\{020\}$-to-$\langle 0\bar{1}1\rangle\{111\}$. Simulation results confirm that the two distinct migration patterns could be activated under different stress/strain states. Moreover, excess GB sliding and GB plane reorientation were found to accommodate the GB migration in both experiments and simulations, likely due to the necessity of establishing a point-to-point lattice correspondence during GB migration. These findings provide atomic-scale experimental evidence on the disconnection-mediated migration of MGBs and elaborate on the hitherto unreported complex shear response of MGBs, which have valuable implications for optimizing the ductility of metallic nanocrystals through controlling GB migration.

5.1 Introduction

Stress-induced grain boundary (GB) migration plays a critical role in the plastic deformation and microstructural evolution of nanocrystalline materials[32, 34, 183]. Promoting GB migration at room temperature can significantly improve the ductility of nanocrystalline materials[184] while inhibiting GB migration at high temperatures could largely enhance the creep resistance of nanocrystals[185]. Understanding the mechanisms of GB migration, especially at the atomic scale, provides important guidelines for tailoring the mechanical properties of nanocrystalline materials through GB engineering. Previous studies reveal that stress-induced GB migration is usually coupled to shear deformation (or GB sliding), namely shear-coupled GB migration [52, 53]. The shear-coupling factor [34, 53], as defined by $\beta = s/m$ where s is the magnitude of GB sliding and m is the distance of GB migration, is used to characterize the GB migration.

Numerous experimental[26, 27, 29, 30, 34, 37], simulation[53, 88, 91], and theoretical studies[58, 59, 186] have been conducted to investigate the shear-coupled GB migration behavior in face-centered cubic metals, with the main focus on simple tilt GBs. Despite that the GBs in these metals are generally mixed tilt-twist GBs (MGBs)[187], the shear-coupled migration behavior of general MGBs has not been fully described and the atomistic mechanisms of the shear-coupled migration of MGB remain largely elusive to date. One micro-scale experimental study revealed the concurrent GB migration and grain rotation during the shear-coupled migration of an MGB in an aluminum bicrystal, where it was deduced that only the tilt component of the MGB determines its shear-coupling factor[28]. Recently, a disconnection model was proposed to describe the GB migration[7]. For high-symmetry GBs such as Σ11(113) symmetrical tilt GB and Σ5(210) symmetrical tilt GB, the simply disconnection-mediated GB migration has been evidenced in both experiments [37, 157, 166] and simulations[70, 71, 96, 188]. In comparison, low-symmetry GBs such as the asymmetrical tilt GB and the MGB may show some special deformation behavior other than the disconnection-mediated GB migration, such as GB sliding[12], GB facet transformation [88, 149, 189], and GB dissociation [88, 149, 189]. Although simulations[105] suggest that thermal-driven migration of some MGBs could be mediated by the motion of step or kink flows, i.e., arrays of disconnections, experimental evidence on whether or how the shear-coupled migration of MGBs is mediated by the GB disconnection is still missing.

In this work, by performing in-situ high-resolution transmission electron microscopy (HRTEM) mechanical testing combined with molecular dynamics (MD) simulations, we investigate the shear-coupled migration behavior of a typical MGB, i.e., $\langle 001\rangle\{200\}/\langle 0\bar{1}1\rangle\{\bar{1}11\}$ GB, during the room-temperature shear deformation of custom-fabricated Au nanocrystals. Atomic-scale experimental evidence that the shear-coupled migration of MGBs is mediated by GB disconnections is presented. Compared to the migration of symmetrical tilt GBs mediated by a single type of GB disconnection [37, 88], the $\langle 001\rangle\{200\}/\langle 0\bar{1}1\rangle\{\bar{1}11\}$ MGB shows two distinct migration patterns that exhibit the opposite signs of shear-coupling factors and different lattice correspondence relations, which are attributed to the activation of GB disconnections with different Burgers vectors. Moreover, the shear-coupled migration of the MGB is cooperated by GB plane reorientation and excess GB sliding occurring at the identical MGB plane, as to establish a point-to-point lattice correspondence during GB migration. Consequently, our findings unprecedently reveal the underlying atomistic mechanisms of the shear-coupled migration of MGBs and the complex mechanical response of MGBs under shear loading, which offer important guidance towards developing metallic nanocrystalline materials with superior mechanical properties via controlling GB migration.

5.2 Experimental Results

5.2.1 Two Distinct Types of Migration Behavior of an Identical GB

Figure 5.1a presents the HRTEM image of the as-fabricated Au bicrystal with a diameter of ~14 nm at the neck region. Based on the HRTEM image and corresponding fast Fourier transform (FFT) pattern, it is confirmed that G1 is $< 001 >$-oriented, G2 is $< 0\bar{1}1 >$-oriented, and the (200) plane of G1 exactly matches the $(\bar{1}11)$ plane of G2 at the interface. Thus, this interface is identified as $\langle 001\rangle_1\,\{200\}_1/\langle 0\bar{1}1\rangle_2\,\{\bar{1}11\}_2$ GB, which is an incommensurate GB due to the irrational ratio of lattice spacing across the interface (i.e., the ratio is $\sqrt{6}/2$). In addition, it is an MGB since the rotation axis for the orientation relationship of this bicrystal is <0.2443, 0.5898, 0.7689> with a rotation angle of ~56.63°. The filtered inverse FFT (IFFT) pattern of the GB region, as inserted at the bottom of Figure 5.1a, is obtained by selecting the diffraction spots of $\{020\}_1$ and $\{111\}_2$ (enclosed by the red circles in the inserted FFT pattern). As shown in the filtered IFFT pattern, the GB structure shows the quasi-periodic feature with uniform distribution of GB misfit dislocations at an average distance of ~1.09 nm along the GB. The value of 1.09 nm is close to the ideal structural repeat distance of this GB, which is ~1.11nm and calculated by $\left[\left|\frac{1}{4}\langle 211\rangle\right|\left|\frac{1}{2}\langle 010\rangle\right|\right]/\left[\left|\frac{1}{4}\langle 211\rangle\right|-\left|\frac{1}{2}\langle 010\rangle\right|\right]$. It should be mentioned that the quasi-periodic feature of GB structure is commonly observed in various types of incommensurate interfaces [174, 190, 191].

Interestingly, performing shear tests on the Au bicrystals with the same orientation relationship as that shown in Figure 5.1a, we observed two distinct types of shear-coupled migration behavior of this MGB. Figures 5.1b-d and 5.1e-g present the sequential HRTEM snapshots showing the two distinct types of shear-coupled GB migration under the "same" shear loading condition (indicated by the white arrows). It is found that although the GBs in the two cases both migrate towards the $[100]$ direction of G1 and lead to the $[001](200)$-to-$[0\bar{1}1](\bar{1}11)$ plane transformation, one is from G1 into G2 (Figs. 5.1b-d, denoted as type-1 GB migration as follows) and the other is from G1 into a newly-formed grain G3 (Figs. 5.1e-g, type-2 GB migration) which is in twinning relationship with G2. Due to the mirror symmetry of the twin boundary, these two types of GB migration migrate towards the same direction under the "opposite" shear loading condition, which indicates the opposite signs of shear-coupling factors. Note that grain G2 rotates slightly by ~3° with the shear strain accumulating, which is likely responsible for the observed lattice distortion and few scattered lattice dislocations in G2 (Figs. 5.1d and 5.1g).

Moreover, the shear deformation of the bicrystals was not fully coupled to either type-1 or type-2 GB migration. Specifically, type-1 GB migration as shown in Figures 5.1b-d cooperated with the excess GB sliding (indicated by the blue arrow in Fig. 5.1d) that occurred on the identical $\langle 001\rangle_1\,\{200\}_1/\langle 0\bar{1}1\rangle_2\,\{\bar{1}11\}_2$ MGB plane to accommodate the overall shear deformation; while the shear deformation of the bicrystal in Figures 5.1e-g was accommodated by the type-2 GB migration along with the upward migration of the residual original MGB (i.e., type-1 GB migration). In addition, GB plane reorientation was observed after both types of GB migration (Figs. 5.1d and 5.1g). The above experimental results indicate that the shear-coupled migration of MGBs is more complicated than that of tilt GBs where the GB migration is usually conservative (i.e., GB structure and GB plane nearly keep the same during the migration) and fully coupled to shear deformation [37, 38].

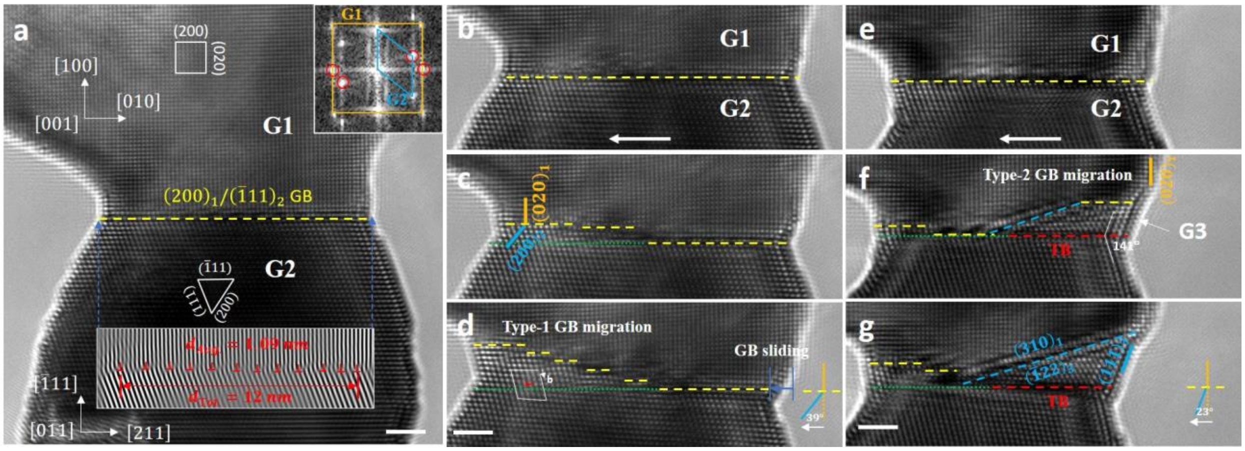
a
[100]
[010]
[001]
(200)
(020)
G1
G2
$(200)_1/(\bar{1}11)_2$ GB
$(\bar{1}11)$
$(1\bar{1}1)$
(200)
$d_{Avg} = 1.09$ nm
$d_{Tot} = 12$ nm
$[\bar{1}11]$
$[0\bar{1}1]$
[211]
b
G1
G2
c
$(020)_1$
d
Type-1 GB migration
GB sliding
39°
e
G1
G2
f
Type-2 GB migration
G3
TB
141°
g
$(310)_1$
TB
23°

Figure 5.1 Two distinct types of shear-coupled migration behavior of the $\langle 001\rangle\{200\}/\langle 0\bar{1}1\rangle\{\bar{1}11\}$ MGB in Au bicrystals. (a) As-fabricated Au bicrystal containing a flat $\{200\}/\{\bar{1}11\}$ MGB at the neck region. Fast Fourier transformation (FFT) pattern and filtered Inversed FFT (IFFT) pattern are inserted to show the crystallography of the bicrystal and the semi-coherent feature of the GB. **(b-d)** With the applied shear deformation (indicated by the white arrow), part of the GB migrated upwards along the [100] direction of grain 1 (denoted as G1) by transforming the $(200)_1$ plane of G1 into the $\{\bar{1}11\}_2$ plane of grain 2 (denoted as G2). **(e-f)** With the "same" shear loading, another type of GB migration behavior that also involves the transformation of (200) plane into $\{\bar{1}11\}$ plane was observed. This kind of GB migration is accompanied by the formation of new grain G3 that is in a twinning relationship with G2. Scale bar: 2nm

5.2.2 Atomistic Processes of the Two Distinct Types of GB Migration

To explore the atomistic mechanisms of the type-1 and type-2 GB migration, frame-by-frame analyses on the GB structural evolution during the migration were conducted and shown in Figures 5.2a-f and 5.2g-l, respectively. It is found that the type-1 GB migration is mainly via the nucleation and motion of GB disconnections with a step height of one atomic layer on the original $\{200\}_1/\{\bar{1}11\}_2$ GB (Figs. 5.2a-c). The directions of GB disconnection motion and GB migration are along [010] and [100] directions of G1, respectively. The inserts in Figures 5.2a and 5.2b indicate the lattice deformation after the glide of a GB disconnection, which clearly shows the displacement of atom columns on the $(\bar{1}11)$ plane of G2 by a maximum value of ~1.4Å during this process. The GB disconnections with the step height of two or three atomic layers were also observed (Figs. 5.2d and 5.2e), which are likely to be formed via the composition of one-layer GB disconnections (Figs. 5.2c-d) and can decompose back into one-layer disconnections in the subsequent deformation (Figs. 5.2e-f). Note that the serrated $\{200\}_1$ and $\{020\}_1$ edge surface morphology of G1 is replaced by the $\{111\}_2$ facet after the type-1 GB migration. It is believed that the $\{020\}_1$ planes of G1 are transformed into the $\{200\}_2$ planes of G2 during the GB migration.

In comparison, type-2 GB migration is not via the direct migration of original $\{200\}_1/\{\bar{1}11\}_2$ GB. It is enabled by the formation of a new grain G3 at the incipient stage of deformation (Fig. 5.2h), which could be a product of GB dissociation [149]. Grain G3 has its $\{\bar{1}11\}$ planes parallel to the $\{200\}$ plane of G1 and is in a twinning relationship with G2. It should be emphasized that the subsequent growth of G3 is not via twinning (i.e., the glide of twinning partials on the twin boundary) but via the migration of GBs between G1 and G3 (Figs. 5.2i-j), including an inclined GB (roughly the $\{3\bar{1}0\}_1/\{\bar{1}22\}_3$ GB) and the horizontal $\{200\}_1/\{\bar{1}11\}_3$ GB. Here, we focus on the migration of $\{200\}_1/\{\bar{1}11\}_3$ GB facet to make the direct comparison to type-1 GB migration. One-layer GB disconnections are also observed to mediate the migration of this GB (Figs. 5.2j and 5.2k). However, different from the process of type-1 GB migration, the motion of these GB disconnections appears to transform the $\{020\}_1$ planes into the $\{111\}_3$ planes, as evidenced by the clockwise rotation of the surface facet by an angle of ~23°.

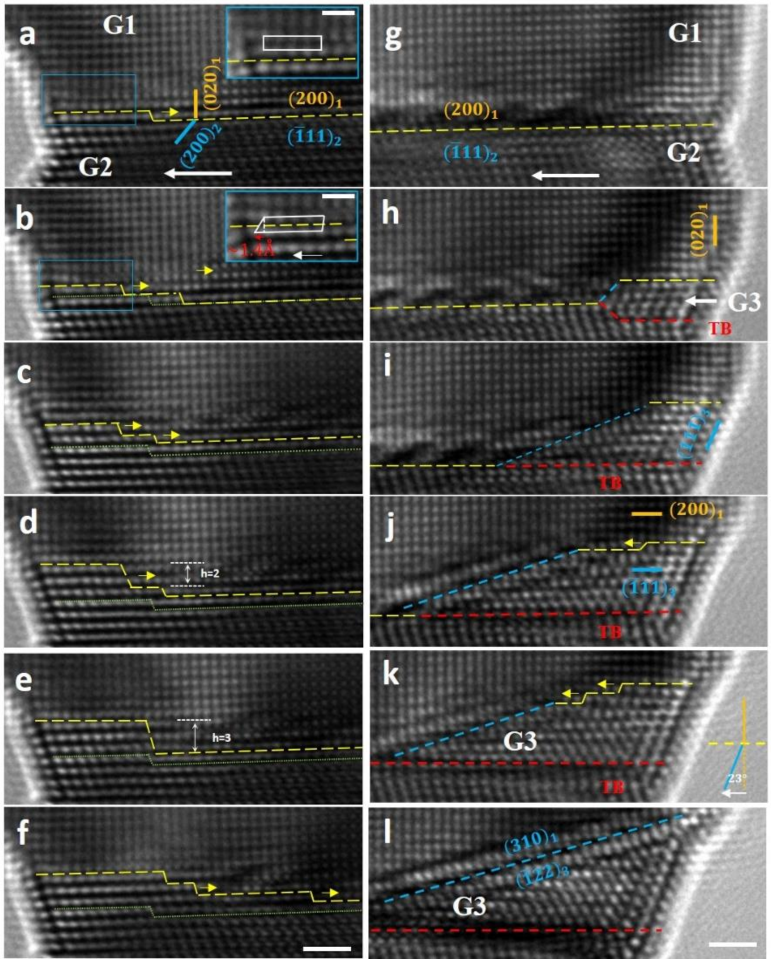

Figure 5.2 Sequential HRTEM snapshots showing the atomistic processes of the two types of GB migration behavior. (a-f) Type-1 GB migration via the continuous motion of GB steps/disconnections. These disconnections are primarily at the step height of the one-atomic layer, but the formation and de-composition of disconnections with a step height of two or three atomic-layer were also observed. Inserts in (a) and (b) show the lattice deformation during GB migration, indicating the transformation from $(\mathbf{020})_1$ plane into $(\mathbf{200})_2$ plane during the process. **(g-l)** Type-2 GB migration that was accompanied by the formation and growth of a new grain (denoted as G3). The growth of G3 was via the migration of GBs between G1 and G3 (indicated by the blue and the yellow dash lines). Some GB disconnections with the step height of one atomic layer can be identified on the $\{\mathbf{200}\}_1/\{\bar{\mathbf{1}}\mathbf{11}\}_3$ GB. Scale bar: **(a-l)**, 1nm; inserts in **(a,b)**, 0.5 nm.

5.2.3 Theoretical Analysis of the GB Disconnections

To elucidate the above experimental results that the two types of GB migration can both be mediated by the motion of one-layer GB disconnections, we conducted theoretical analysis of the crystallographic parameters of these GB disconnections. By comparing the GB disconnections as shown in Figure 5.3a, it is found that the two disconnections migrate towards the same direction under the "opposite" shear loading (Fig 5.3a$_2$ is flipped horizontally for direct comparison). It is thus inferred that the Burgers vectors of these disconnections are in opposite directions. According to the Pond's topological theory of bicrystallography[67, 68], the Burgers vectors of interfacial defects can be determined by carrying out the Volterra operation at the incompatible surface steps constructing the interfacial defects (Fig. 5.3b), which gives

$$\boldsymbol{b} = \boldsymbol{t}(\lambda) - \boldsymbol{P}\boldsymbol{t}(\mu) \tag{5-1}$$

Where $\boldsymbol{t}(\lambda)$ and $\boldsymbol{t}(\mu)$ are translation vectors defining the surface steps on the adjacent crystals (Fig. 5.3b), $\mathbf{P}$ is a transformation matrix re-expressing $\boldsymbol{t}(\mu)$ in the coordinate frame of λ. Because the $\langle 001\rangle_1\{200\}_1/\langle 0\bar{1}1\rangle_2\{\bar{1}11\}_2$ GB exhibits semi-coherent feature (Fig. 5.1a), the strained coherent dichromatic pattern (CDP) was used as the reference to analyze the Burgers vectors of disconnections [192]. The CDP could be obtained by applying biaxial strains to the two half-crystals in order to bring them into coherency at the interface. Here, the two half-crystals were equally strained to form the coherent reference state indicated by the dark unfilled symbols in Figure 5.3c. A unit cell of the coherent reference state at the interface is marked by the dark solid lines in Figure 5.3c, which shows the planar spacings along the two commensurate directions, i.e., $[001]_1$ and $[010]_1$, equal to $(\sqrt{6}+2)a/8$ and $(\sqrt{2}+2)a/8$, respectively. Accordingly, the coherent dichromatic pattern (CDP) for the analysis of disconnections of the

$\langle 001\rangle\{200\}/\langle 0\bar{1}1\rangle\{\bar{1}11\}$ GB can be obtained as shown in Figure 5.3d, where μ is the $\langle 001\rangle$-oriented G1 indicated by symbols in dark blue and λ is the $\langle 0\bar{1}1\rangle$-oriented G2 represented in light blue. The square and circle symbols indicate the atoms belonging to different $\{002\}_1$ or $\{0\bar{1}1\}_2$ planes along the out-of-paper direction. As shown in Figure 5.3d, for the translation vector $\boldsymbol{t}(\mu) = \frac{1}{2}\langle\bar{1}01\rangle_1$for the $\langle 001\rangle$-oriented G1, there are two types of admissible translation vector $\boldsymbol{t}(\lambda)$, i.e., $\frac{1}{4}\langle 2\bar{1}\bar{1}\rangle_2$ or $\frac{1}{2}\langle 011\rangle$, for the $\langle 0\bar{1}1\rangle$-oriented G2. Consequently, there are two different combinations of translation vectors to construct the one-layer disconnections, which would generate two different Burgers vectors (numbered as $\boldsymbol{b_1}$ and $\boldsymbol{b_2}$, Fig. 5.3d). Crystallographic parameters of these four admissible Burgers vectors are listed in Table 5.1. It is shown that $\boldsymbol{b_1}$ and $\boldsymbol{b_2}$ disconnections both contain the Burgers vector components perpendicular to the GB plane (denoted as $\boldsymbol{b}_p$), which is small ($|\boldsymbol{b}_p| = \frac{2\sqrt{3}-3}{6}a$, $a = 4.08$ Å is the lattice constant of Au) and should be efficiently accommodated by the disconnections themselves[193]. Moreover, $\boldsymbol{b_1}$ type disconnection has an edge component $\boldsymbol{b_e}$ ($|\boldsymbol{b}_e| = \frac{\sqrt{6}+2}{12}a$) and a screw component $\boldsymbol{b}_s$ ($|\boldsymbol{b}_s| = \frac{2+\sqrt{2}}{8}a$). In contrast, $\boldsymbol{b_2}$ type disconnection has only the edge component $\boldsymbol{b_e}$ ($|\boldsymbol{b}_e| = \frac{\sqrt{6}+2}{24}a$). In addition, the edge component of $\boldsymbol{b_1}$ is in the opposite direction of that of $\boldsymbol{b_2}$. It should be mentioned that the crystallographic parameters of these two admissible types of disconnections (Table 5.1) are deduced on the basis of a strained CDP which is a purely topological model. In addition, non-affine movement of atoms (i.e., shuffling) is believed to be indispensable to accomplish the GB migration. Therefore, it is hard to determine the exact values of the Burgers vectors of these disconnections at this point. Referring to the right-hand rule of determining the motion direction of a given dislocation under an applied shear stress, we find that the motion of $\boldsymbol{b_1}$ type disconnections mediates the type-1 GB migration (Figure 5.2a-f) while the $\boldsymbol{b_2}$ type disconnection accommodates the type-2 GB migration (Figure 5.2g-l). One further evidence is that the maximum lattice displacement generated by the glide of disconnection during type-1 GB migration is ~1.4Å (as measured in the inserts of Figure 5.2a-b), which reseaonably matches the magnitude of the edge component of $\boldsymbol{b_1}$ disconnection.

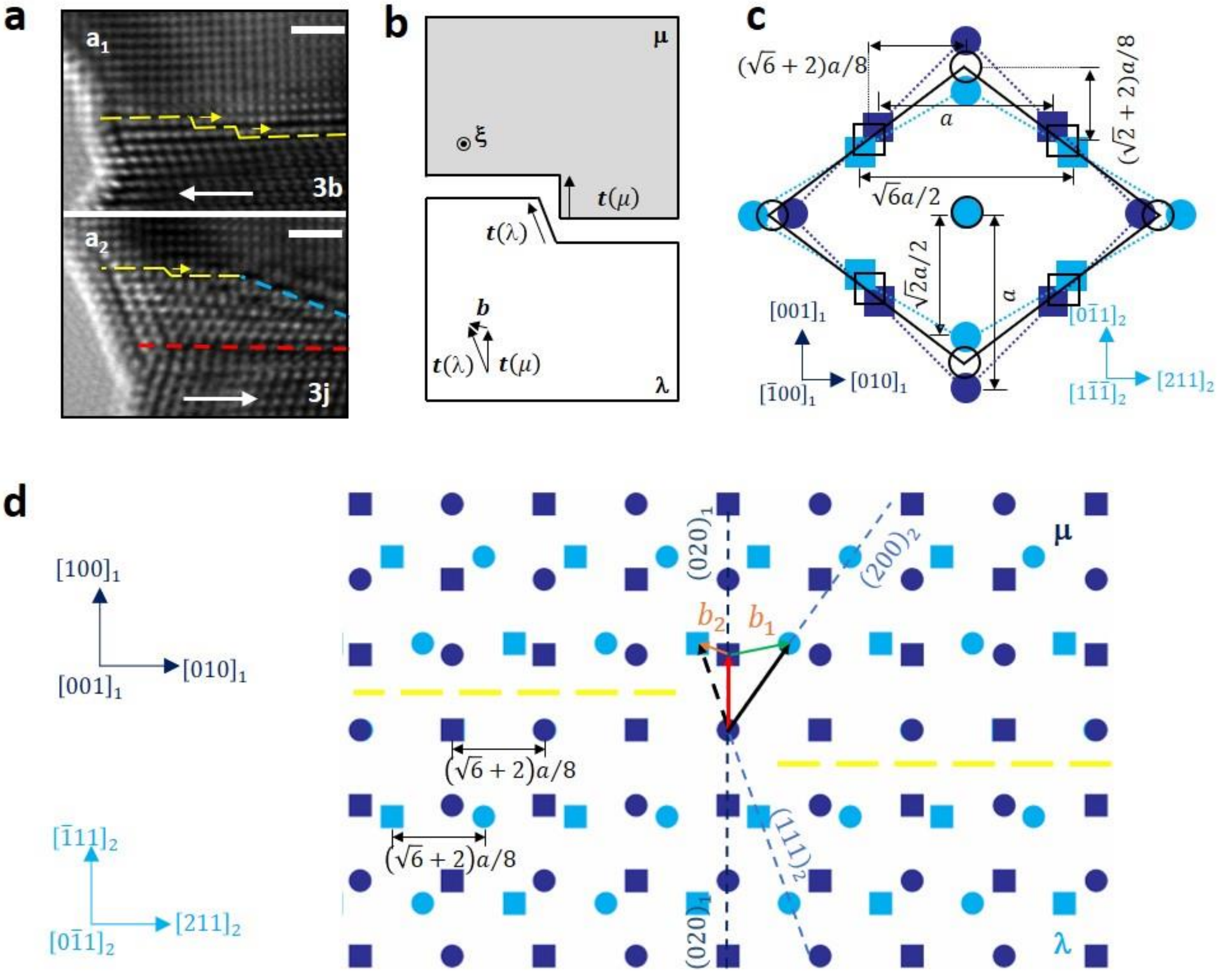

Figure 5.3 Theoretical analysis of the admissible GB disconnections of the $\langle\mathbf{001}\rangle\{\mathbf{200}\}/\langle\mathbf{0\bar{1}1}\rangle\{\mathbf{\bar{1}11}\}$ MGB. (a) Comparsion of the GB disconnections mediating the two types of GB migration. **(a$_1$)** was cropped from Figure 5.2b while **(a$_2$)** is taken from Figure 5.2j and flipped horizontally for comparison. **(b)** Schematic illustration showing the formation of a GB disconnection by bonding the two incompatible surface steps. The direction of the sense vector ξ is out-of-paper. **(c)** Schematic illustration showing the construction of a strained coherent reference state at the GB plane. The dark blue, light blue, and dark unfilled symbols indicate the unstrained $(\mathbf{200})$ plane of crystal μ, the unstrained $(\mathbf{\bar{1}11})$ plane of crystal λ, and the coherent reference state, respectively. The cubic and circle symbols indicate the atoms in different depths along the $[001]_1$ direction. **(d)** Coherent dichromatic pattern for the disconnection

analysis of $\langle \mathbf{001}\rangle\{\mathbf{200}\}/\langle \mathbf{0\bar{1}1}\rangle\{\mathbf{\bar{1}11}\}$ GB. The dark blue and light blue symbols in (d) indicate the strained crystal μ and crystal λ, separately**.** The yellow dash lines indicate the GB plane with a disconnection on it.

Table 5.1 Crystallographic parameters of two admissible one-layer disconnections. $\boldsymbol{b_e}$ and $\boldsymbol{b_s}$ represent the Burgers vectors of their edge and screw components, and $\boldsymbol{b_p}$ indicates the Burgers vector component that is perpendicular to the GB plane.

Disconnection type	$\boldsymbol{t(\lambda)}$	$\boldsymbol{t(\mu)}$	$\boldsymbol{b_e}$	$\boldsymbol{b_p}$	$\boldsymbol{b_s}$
$\boldsymbol{b_1}$	$\frac{1}{2}\langle 011\rangle$	$\frac{1}{2}\langle \bar{1}01\rangle$	$\frac{\sqrt{6}+2}{12}a$	$\frac{2\sqrt{3}-3}{6}a$	$\frac{\sqrt{2}+2}{8}a$
$\boldsymbol{b_2}$	$\frac{1}{4}\langle 2\bar{1}\bar{1}\rangle$	$\frac{1}{2}\langle \bar{1}01\rangle$	$\frac{\sqrt{6}+2}{24}a$	$\frac{2\sqrt{3}-3}{6}a$	0

Furthermore, one may find from Figure 5.3d that the two types of GB migration lead to different lattice correspondence relationships during GB migration as the movement of atoms is along different directions. In both cases, $(200)_1$ atomic plane would transform into $(\bar{1}11)_2$ atomic plane during disconnection-mediated GB migration as the two planes are parallel to the GB. This transformation process involves in-plane atom shuffling as shown in Figure 5.4b. However, for the other atomic planes that are not parallel to the GB, lattice correspondence relationships of the two types of GB migration are different. Specifically, the type-1 GB migration mediated by the $\boldsymbol{b_1}$ type disconnection would transform the $(020)_1$ plane of G1 into the $(200)_2$ plane of G2 (Fig. 5.4a). Except for the shuffling accompanying the $(200)_1$-to- $(\bar{1}11)_2$ transformation, an additional shear with a magnitude of $\frac{\sqrt{2}}{4}a$ (indicated by the orange arrow, which is parallel to $\langle 0\bar{1}1\rangle_2$ direction and contributed by the screw component of $\boldsymbol{b_1}$ type disconnections) and shuffling (indicated by the green arrow) within the $(020)_1$ plane are needed to accomplish the $(020)_1$-to-$(200)_2$ lattice transformation (Fig. 5.4c). While for the type-2 GB migration, the motion of $\boldsymbol{b_2}$ type disconnection would lead to the transformation of $(020)_1$ atomic plane into the $(111)_2$

atomic plane (Fig. 5.4a), during which only atom shuffling is needed (Fig. 5.4c). Note that the dashed purple circles in Figure 5.4c indicate the atoms in rearranged $(020)_1$ plane after the $(200)_1$-to- $(\bar{1}11)_2$ transformation, instead of the original $(020)_1$ plane. The crystallographic parameters of $\boldsymbol{b_1}$ type disconnections can thus be modified: the $\boldsymbol{b_1}$ type disconnection should have an edge component with the magnitude of $\frac{\sqrt{6}+2}{12}a$ and a screw component with the magnitude of $\frac{\sqrt{2}}{4}a$.Note that accurate crystallographic parameters of these GB disconnections can not be determined at this point due to the uncertain extent of atom shuffling.

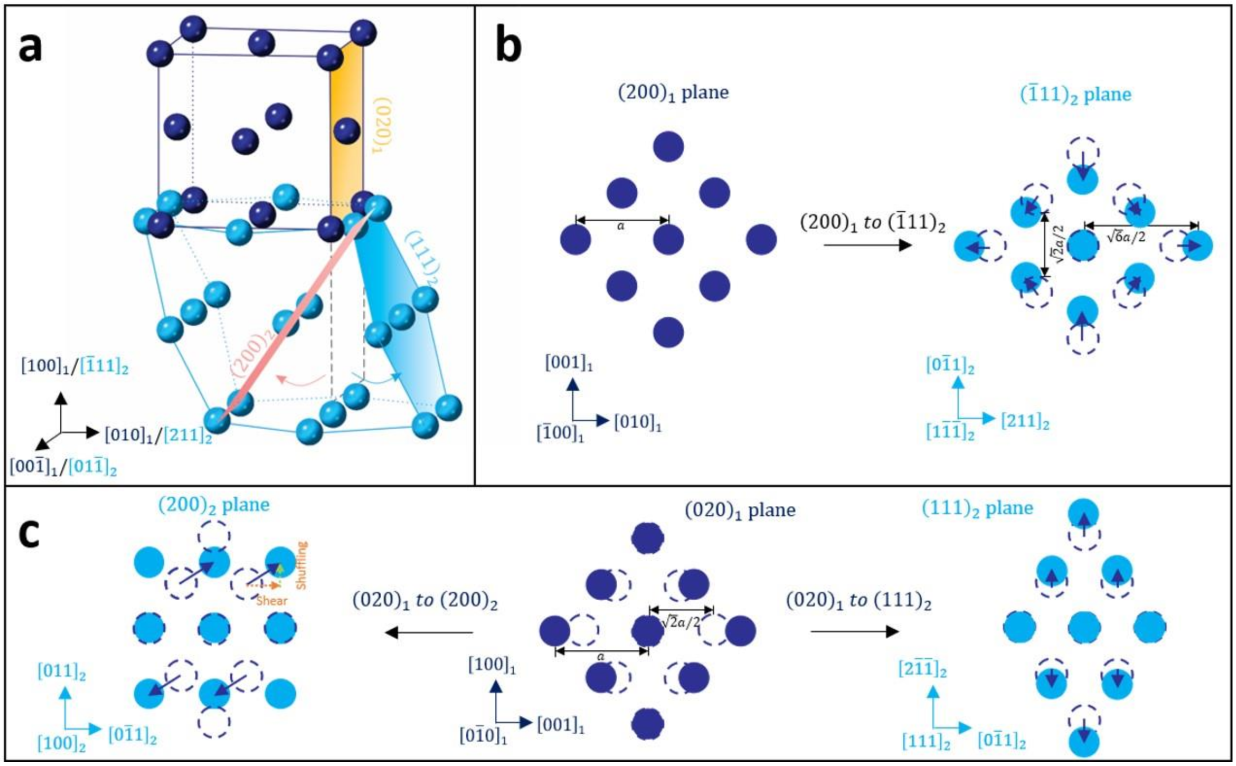
a
$(020)_1$
$(111)_2$
$(200)_2$
$[100]_1/[\bar{1}11]_2$
$[010]_1/[211]_2$
$[00\bar{1}]_1/[01\bar{1}]_2$
b
$(200)_1$ plane
$(\bar{1}11)_2$ plane
a
$(200)_1$ to $(\bar{1}11)_2$
$\sqrt{2}a/2$
$\sqrt{6}a/2$
$[001]_1$
$[\bar{1}00]_1$
$[010]_1$
$[0\bar{1}1]_2$
$[1\bar{1}\bar{1}]_2$
$[211]_2$
c
$(200)_2$ plane
Shuffling
Shear
$(020)_1$ to $(200)_2$
$(020)_1$ plane
$\sqrt{2}a/2$
a
$(020)_1$ to $(111)_2$
$(111)_2$ plane
$[011]_2$
$[100]_2$
$[0\bar{1}1]_2$
$[100]_1$
$[0\bar{1}0]_1$
$[001]_1$
$[2\bar{1}\bar{1}]_2$
$[111]_2$
$[0\bar{1}1]_2$

Figure 5.4 Topological analysis of the lattice transformation relations during GB migration. (a) Atomic models of the $\langle\mathbf{00\bar{1}}\rangle$-oriented G1 and the $\langle\mathbf{01\bar{1}}\rangle$-oriented G2 with the $(\mathbf{100})$ plane of G1 parrallel to the $(\mathbf{\bar{1}11})$ plane of G2. Atoms in G1 are colored purple while that in G2 are blue. **(b)** Schematic illustration showing the necessary localized atoms adjustment to complete the $(\mathbf{200})_\mathbf{1}$-to- $(\mathbf{\bar{1}11})_\mathbf{2}$ transformation. **(c)** Schematic illustration showing the two different lattice transformation relations: $(\mathbf{020})_\mathbf{1}$-to-$(\mathbf{200})_\mathbf{2}$ and $(\mathbf{020})_\mathbf{1}$-to-$(\mathbf{111})_\mathbf{2}$. The dash purple circles indicate the atoms arrangement of $(\mathbf{020})_\mathbf{1}$ plane after the shuffling during the $(\mathbf{200})_\mathbf{1}$-to- $(\mathbf{\bar{1}11})_\mathbf{2}$ transformation. The purple arrows in (b) and (c) indicate the movement of atoms during the transformations. The dash orange arrow and the green

arrow in (c) indicate the shear displacement contributed by the screw component of disconnection and the atoms shuffling to accompany the transformation, separately.

5.2.4 MD Simulation of Two Types of GB Migration

According to the theoretical analysis above, the GB disconnections in the two types of GB migration are deduced to have different crystallographic parameters and result in different lattice correspondence relations. Consequently, the activation of GB migration following different lattice correspondence relations would require different stress/strain states. Referring to the modified crystallographic parameters of the disconnections, the type-1 GB migration following the $(020)_1$-to-$(200)_2$ plane transformation (i.e., mediated by $\boldsymbol{b_1}$ type disconnection) is preferred when the shear loading has an angle between 43.6° with the $\langle 010 \rangle_1$ direction, while the type-2 GB migration following the $(020)_1$-to-$(111)_2$ plane transformation is activated when the shear loading is parallel to the $\langle 010 \rangle_1$ direction. Considering that HRTEM images are projective and phase-contrast images, exactly resolving the structure change along the beam direction and the lattice correspondence relations during GB migration from HRTEM images is difficult. Therefore, we constructed two MD simulation models, one has the shear direction parallel to the $\langle 010 \rangle_1$ direction but the one has the shear direction parallel to the $\langle 0\bar{1}1 \rangle_1$ direction, to further verify the two types of GB migration and underlying lattice correspondence relations.

Figure 5.5 presents the case of shearing parallel to the $\langle 010 \rangle_1$ direction. As shown in Figures 5.5a and 5.5b, after the shear deformation, the original flat $(200)_1/(\bar{1}11)_2$ GB in the bicrystal was replaced by a twin boundary and an inclined GB consisting of $(200)/(\bar{1}11)$ GB nanofacets, which exactly matches the GB deformation behavior in Figures 5.1e-f. The formation of the twin boundary is because that the shear direction $\langle 010 \rangle_1$ is parallel to the Burgers vector of one of the Shockley partial dislocations of the bottom grain G2. Thereafter, an analysis of the sequential snapshots of MD simulations was performed to view the atomistic process of GB migration. From the analysis, we noticed that the GB deformation along the $[001]_1$ direction of the bicrystal is complicated and not uniform. To better elucidate this non-uniform GB deformation, the front views of the bicrystal at different depths along the $[001]_1$ direction during the deformation are presented in Figures 5.5c-f (i.e., middle) and Figures 5.5g-j (i.e., side), and meanwhile the top views of a selected $(200)_1$ atomic plane (indicate by the red arrows in Figures 5.5c and 5.5g) during the deformation are shown in Figure 6k-n. Note that Figures 5.5c-f, .5.5g-j, and 5.5k-n are taken at the same time sequence. In addition, several $(020)_1$ atomic planes are colored in orange to show the transformations of these atomic planes during GB migration (Figures 5.5c-j).

At the incipient stage of deformation, there is a new grain (denoted as G3) that was formed at the region at the middle of the GB (Figure 5.5k) and near the right side free surface of the bicrystal (Figure 5.5c). The new grain G3 is in twinning relation with the bottom grain G2. While for the region near the front (and back) side of the bicrystal, the GB first migrated downward for several atomic layers through the collective motion of one-atomic-layer $\boldsymbol{b_2}$ type GB disconnections (Figures 5.5g and 5.5k). Then, a new grain G4 that is also in a twinning relationship with G2 was formed (Figures 5.5e and 5.5h) and the growth of G4 at subsequent deformation was via the collective migration of the $(200)_1/(\bar{1}11)_4$ GB nanofacets (Figure 5.5h-j). The collective migration of these $(200)_1/(\bar{1}11)_4$ GB nanofacets exactly followed the (020)-to-(111) type lattice correspondence relation (i.e., type-2 GB migration), as directly evidenced by the transformation of the vertical $(020)_1$ atomic planes (colored in orange) into the inclined $(111)_4$ atomic planes (Figures 5.5g-j). Back to the complex deformation at the middle-right region of GB, the new grain G3 did not grow like G4. Instead, the entire G3 glided along the $(200)_1/(\bar{1}11)_2$ GB, which was enabled by the motion of disconnections that are between G1 and G3. It requires that these disconnections (indicated by the solid and the dashed blue curves in Figures 5.5m and 5.5n) have different Burgers vectors, i.e., $\boldsymbol{b_2}$ type and $\boldsymbol{b_1}$ type. In fact, stacking faults (SFs) were formed in G3 before the glide of G3 as a whole. The formation of SFs can exactly compensate for the differences in the screw component between $\boldsymbol{b_1}$ type and $\boldsymbol{b_2}$ type disconnections.

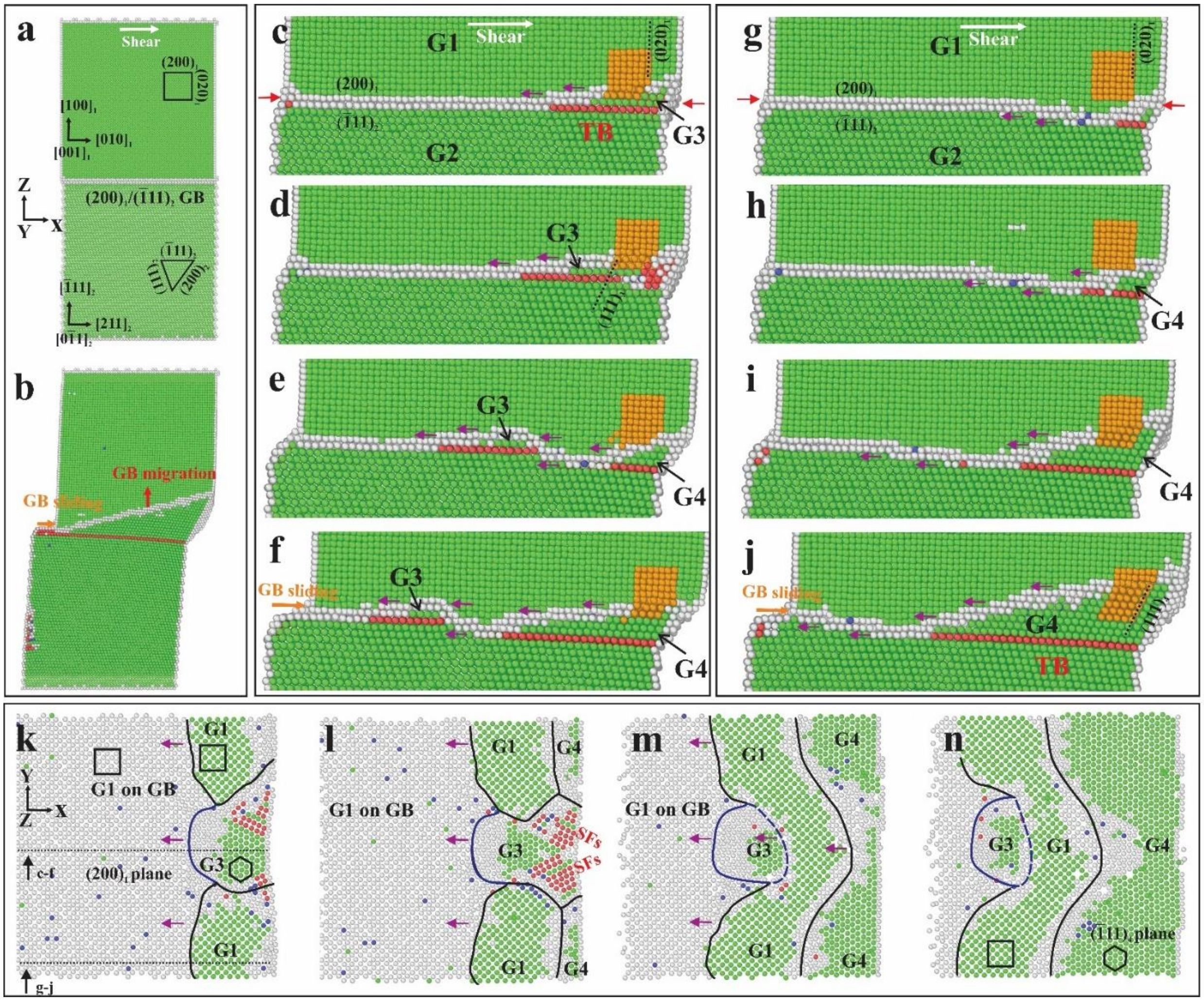
a
Shear
(200)₁
(020)₁
[100]₁
[010]₁
[001]₁
Z
Y
X
(200)₁/(1̄11)₂ GB
(1̄11)₂
(111)₂
(200)₂
[1̄11]₂
[211]₂
[01̄1]₂
b
GB migration
GB sliding
c
G1
Shear
(020)₁
(200)₁
(1̄11)₂
TB
G3
G2
d
G3
(111)₂
e
G3
G4
f
GB sliding
G3
G4
g
G1
Shear
(020)₁
(200)₁
(1̄11)₂
G2
h
G4
i
G4
j
GB sliding
G4
TB
(111)₂
k
G1
Y
X
Z
G1 on GB
G3
c-f
(200)₁ plane
G1
g-j
l
G1
G4
G1 on GB
G3
SFs
SFs
G1
G4
m
G1
G4
G1 on GB
G3
G1
G4
n
G3
G1
G4
(1̄11)₂ plane

Figure 5.5 MD results of GB migration following the $(020)_1$-to-$(111)_2$ type lattice transformation. (a, b) Au bicrystal before and after the shear deformation. Shear displacement was applied on the top fixed end along the $[010]_1$ direction. **(c-f, g-j)** Sequential snapshots showing the GB structures at different depths along the $[010]_1$ direction . The sliced positions are indicated by the dashed lines in k. Selected atom columns on $(020)_1$ atomic planes were colored orange to show the lattice transformation. New grains formed after twinning are denoted as G3 and G4,

separately. The purple arrows indicate the motion directions of GB disconnections. **(k-n)** Top views of a thin (indicated by the red arrows in c and g) atomic layer showing the atomic plane transformation during GB migration in c-f and g-h. The curved lines represent the disconnection lines between different grains. Green atoms represent the bulk face-centered cubic atoms while white ones indicate boundary atoms.

Figure 5.6 shows the case of shearing parallel to the $\langle 0\bar{1}1\rangle_1$ direction. In this case, the bicrystal was rotated 45° around the $[100]_1$ direction to present the lattice transformation during GB migration (Figure 5.6a). After shear deformation, the $(200)_1/(\bar{1}11)_2$ GB migrated downward (Figure 5.6b). The sequential snapshots of MD simulations results in Figures 5.6c-f show that the GB migration in this case followed the (020)-to-(200) type lattice correspondence relation (i.e., type-1 GB migration), as evidenced by the transformation of the inclined $(200)_2$ atomic planes (colored in dark green) into the vertical $(020)_1$ atomic planes. Meanwhile, the top views of the selected $(\bar{1}11)_2$ atomic plane (indicated by the red arrows in Figure 5.6c) captured at the same time sequence as that of Figures 5.6c-f clearly shows the $(\bar{1}11)_2$-to-$(200)_1$ plane transformation was mediated by the motion of GB disconnection (Figs. 5.6g-j).

The MD simulation results confirm the two different GB migration patterns and underlying lattice correspondence relations, i.e., (020)-to-(111) type and (020)-to-(200) type, of the $(200)_1/(\bar{1}11)_2$ GB. In addition, akin to experimental results in Figure 5.1b-g, GB sliding and GB plane reorientation are found to concurrently occur with the GB migration (Figs. 5.5b and 5.6b). Notably, the GB sliding also happened on the $(200)_1/(\bar{1}11)_2$ GB plane, as reflected in the surface steps that were formed after the shear deformation of the bicrystals (Figures 5.5b and 5.6b).

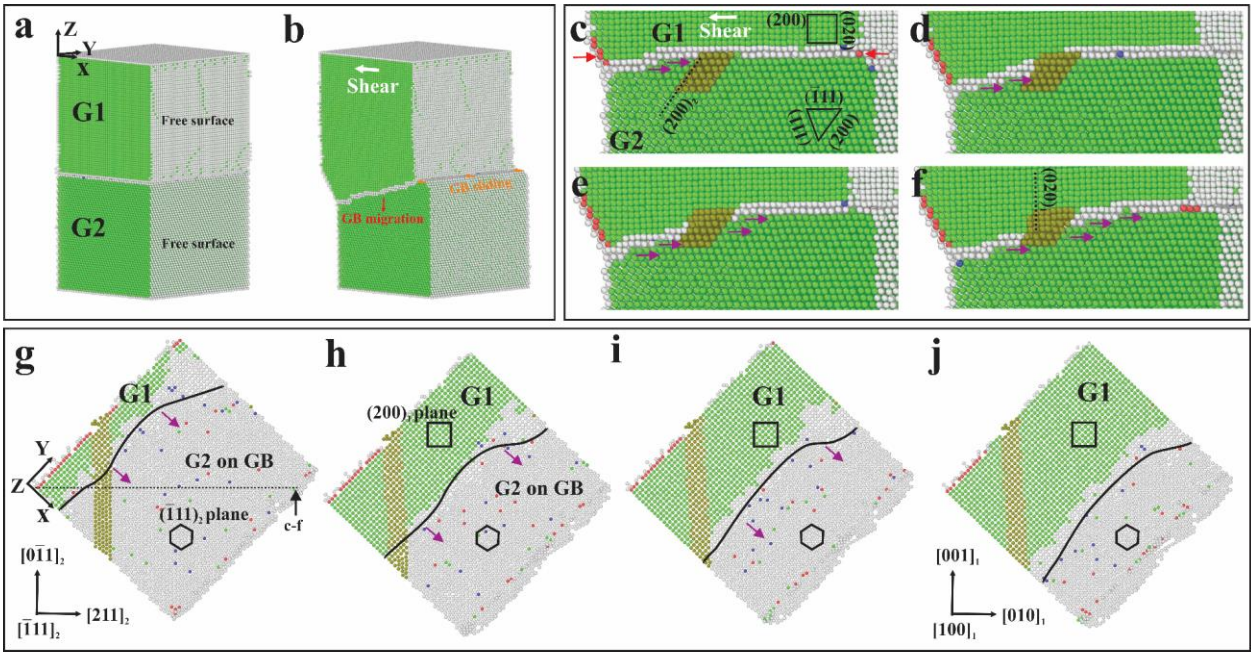
a
Z
Y
X
G1
Free surface
G2
Free surface
b
Shear
GB sliding
GB migration
c
G1
Shear
(200)
(020)
(200)₂
(111)
(111)
(200)
G2
d
e
f
(020)
g
G1
G2 on GB
Y
Z
X
(111)₂ plane
c-f
[01̄1]₂
[211]₂
[1̄11]₂
h
(200)₁ plane
G1
G2 on GB
i
G1
j
G1
[001]₁
[010]₁
[100]₁

Figure 5.6 MD results of GB migration following the $(200)_2$-to-$(020)_1$ lattice transformation. (a, b) Au bicrystal before and after the shear deformation. Shear displacement was applied on the top fixed end along the x-axis of the bicrystal, i.e., $[01\bar{1}]_1$ direction. **(c-f)** Sequential snapshots showing the $(200)_2$-to-$(020)_1$ lattice plane transformation during the GB migration. The sliced positions are indicated by the dashed lines in **g**. Atoms on $(200)_2$ atomic planes are selectively colored in dark green to trace the lattice transformation. The purple arrows indicate the motion directions of GB disconnections. **(g-j)** Top views of a thin slice perpendicular to the z-axis showing the $(\bar{1}11)_2$-to-$(200)_1$ atomic plane transformation during GB migration in **c-f**. The position of the thin slice is indicated by the red arrows in **c**.

5.2.5 Origin of Excess GB Sliding and GB Plane Reorientation

Given that both experimental (Figs. 5.1b-g) and simulational (Figs. 5.5 and 5.6) results indicate that excess GB sliding and GB plane reorientation accommodate the GB migration, additional theoretical analysis was performed to pinpoint the roots of these phenomena. In theory, GB migration is essentially the result of lattice transformation between the adjoining crystals [7, 53]. Therefore, disconnection-mediated shear-coupled GB migration has to establish a point-to-point lattice correspondence relation between the crystals. For the symmetrical tilt GBs such as the Σ11(113) symmetrical tilt GB, the atomic planes perpendicular to the GB are identical, e.g., $\{113\}$ planes, which makes the point-to-point lattice correspondence during GB migration easy to establish. In comparison, the non-symmetrical GBs such as asymmetrical tilt GBs and MGBs have different atomic planes adjoined at the GB plane. Different atomic planes have different planar packing fractions (PPFs), which makes the establishment of point-to-point lattice correspondence in non-symmetrical GBs more difficult than that in symmetrical tilt GBs. There must be some prerequisites for the GB disconnections so they can effectively mediate the shear-coupled migration of these non-symmetrical GBs. For instance, Pond et al. investigated the structure and mobility of various interfacial defects, i.e., disconnections, at a $\langle 110\rangle\, 90°\ (111)/(1\bar{2}1)$ asymmetrical tilt GB in Au using postmortem HRTEM and atomistic simulation, and they found that only the $\boldsymbol{b}_{3/1}$ disconnections ($3/1$ means three $(2\bar{4}2)$ atomic planes match one (111) atomic plane at the disconnections) can move conservatively under an applied shear strain, as to ensure the constant total number of atoms during GB migration [166].

Regarding the $\langle 001\rangle\{200\}/\langle 0\bar{1}1\rangle\{\bar{1}11\}$ MGB in our work, our results have shown that the dominant GB disconnections mediating the GB migration have a step height of one atomic layer, i.e., one (200) atomic plane matches one $(\bar{1}11)$ atomic plane at the disconnections (Figure 5.2), and have $b_p = \frac{2\sqrt{3}-3}{6}a$. As presented in ref [194], when a disconnection of a length L and step height h moves in a velocity of v, the diffusive flux during the motion can be expressed as:

$$I = Lv\left[h\Delta X + \ b_p X\right] \tag{5-2}$$

where ΔX indicates the difference in the number of atoms per unit volume between the two crystals μ and λ, e.g., X^{λ}-X^{μ}; X could be either X^{λ} or X^{μ}, depending on the direction of disconnection movement; b_p is the disconnection's Burgers vector component that is perpendicular to the interface, i.e., the climb component. In the present case, crystals μ and λ are Au crystals having the identical number of atoms per unit volume (i.e., $X^{\lambda}=X^{\mu}$), which makes ΔX=0. Then, equation (5.2) can be re-formulated as:

$$I = Lvb_pX \tag{5-3}$$

Therefore, the diffusive flux accompanying the motion of a disconnection is directly caused by the motion of the climb component of the disconnection, i.e. b_p. The diffusional flux of these one-atomic-layer disconnections is non-zero as $b_p = \frac{2\sqrt{3}-3}{6}a$, which suggests these disconnections cannot move conservatively. To further elaborate on this issue, we estimated the climbing velocity of these one-atomic-layer disconnections to explain the observed mobility of these disconnections. The estimation of climbing velocity was carried out using the method presented in Ref [157] and gave a value of $1.47\ \mu m\ s^{-1}$ which is higher by five orders of magnitude than the deformation speed applied in the experiments, i.e., $0.01\ nm\ s^{-1}$. Hence, it is believed that a high velocity of the moving climb component of these disconnections could result in the observed mobility of these disconnections.

As the motion of a one-atomic-layer disconnection alone cannot mediate the conservative migration of the MGB, excess GB sliding occurred simutaneously with GB migration. Moreover, to eventually achieve the conservative GB migration, the area ratio of the (200) and $(\bar{1}11)$ planes matched at the GB has to be inversely proportional to the PPFs ratio of these planes ($PPF\{111\}/PPF\{002\} = 1.154$), ensuring the constant total number of atoms during GB migration. The GB plane reorientation can exactly alter the area ratio of the matching (200) and $(\bar{1}11)$ planes at the GB and a simplified geometrical model is proposed as follows to elucidate it. Figure 5.7b illustrates the scenario that the $\langle 001\rangle\{200\}/\langle 0\bar{1}1\rangle\{\bar{1}11\}$ MGB plane rotated anticlockwise around the out-of-paper direction by a certain angle α. Assuming the length of the bicrystal along the out-of-plane direction is a constant, the rotated GB plane would have the area ratio of the matching (200) and $(\bar{1}11)$ planes equal to the length ratio of $l_{(200)1}$ and $l_{(\bar{1}11)2}$ as shown in Figure 5.7b. The relations between $l_{(200)1}$, $l_{(\bar{1}11)2}$, and the length of the projected GB plane, i.e., l_{GB}, are as follows:

$$l_{(200)1} = l_{GB}\cos\alpha \tag{5-4}$$

and

$$l_{(\bar{1}11)2} = l_{GB}\sin(109.5° - \alpha)/\sin\alpha \tag{5-5}$$

Then, the length ratio is

$$l_{(200)1}/l_{(\bar{1}11)2} = \sin\alpha\cos\alpha/\sin(109.5° - \alpha) \tag{5-6}$$

On the basis of Eqn. (5.6), the change of length ratio to the inclination angle α is plotted in Figure 5.7c. It clearly shows that the length ratio increases with the inclination angle, and equals the PPFs ratio of $(\bar{1}11)$ and (200) planes at the inclination angle of ~20°. It indicates that GBs with an inclination angle close to 20° could build up the point-to-point lattice correspondence and thus migrate conservatively. To verify this conjecture, both experimental and simulational studies were performed and shown in Figures 5.7d-m. Figures 5.7d-i present the experimental results that an Au bicrystal with the $\langle 001\rangle_1\{200\}_1/\langle 0\bar{1}1\rangle_2\{111\}_2$ GB was deformed by the applied shear strain (indicated by the white arrow in Figure 5.7d), where the shear direction has a rotated angle of ~23° to the original GB plane. At the incipient deformation stage, the GB plane was reoriented to be nearly parallel to the shear direction (Figure 5.7e). Then, the re-oriented GB migrated with no further GB plane reorientation observed (Figures 5.7f-i). The $\{\bar{1}11\}_2$ surface facet of the bottom grain changed into the $\{020\}_1$ surface facet of the upper grain under the shear loading, which accompanied the GB migration towards the bottom grain. Additionally, the shear-coupling factor during the steady state of GB migration (Figure 5.7f-i) is measured to be ~0.55±0.02, which reasonably matches the theoretical value of ~0.523 that is calculated based on the $\{\bar{1}11\}_2$-to-

$\{020\}_1$ lattice correspondence relationship ($\beta \approx \tan 39° - \tan 16°$). In addition, Figures 5.7j-m show the simulational results of the shear-coupled migration of a $\langle 001\rangle_1\,\{3\bar{1}0\}_1/\langle 0\bar{1}1\rangle_2\,\{255\}_2$ GB that has an inclination angle of ~19° to the $\langle 001\rangle_1\,\{200\}_1/\langle 0\bar{1}1\rangle_2\,\{111\}_2$ GB. The as-constructed $\langle 001\rangle_1\,\{3\bar{1}0\}_1/\langle 0\bar{1}1\rangle_2\,\{255\}_2$ GB had a faceted GB structure (Figure 5.7j) that later transformed into an array of $\langle 001\rangle_1\,\{200\}_1/\langle 0\bar{1}1\rangle_2\,\{111\}_2$ GB nanofacets connected by the GB disconnections during the subsequent shear deformation (Figures 5.7k-m). No substantial excess GB sliding and GB plane reorientation were observed during this process and the changes in the selected $(020)_1$ atomic planes (colored in orange) after the GB migration (Figure 5.7m) proves the GB migration followed the $\{020\}_1$-to-$\{\bar{1}11\}_2$ lattice correspondence relationship.

It needs to mention that Figure 5.7 only depicts the case of GB migration following the $\{020\}_1$-to-$\{\bar{1}11\}_2$ type lattice correspondence relationship (i.e., type-2 GB migration) as an example. GB migration following the $\{020\}_1$-to-$\{200\}_2$ type lattice correspondence relationship (i.e., type-1 GB migration) is also expected to reorient the GB plane to achieve the conservative GB migration (e.g., Figure 5.1b-d), but such GB plane reorientation should not only occur around the out-of-plane direction (i.e., $[001]_1$) as that in Figure 5.7 but occur around $[010]_1$direction since the GB disconnections mediating the $\{020\}_1$-to-$\{200\}_2$ type lattice transformation shall have an additional shear component parallel to the $[010]_1$direction. More delicate experimental or simulational studies are needed in the future to elucidate the exact criteria of conservative GB migration following $\{020\}_1$-to-$\{200\}_2$ type lattice correspondence relation.

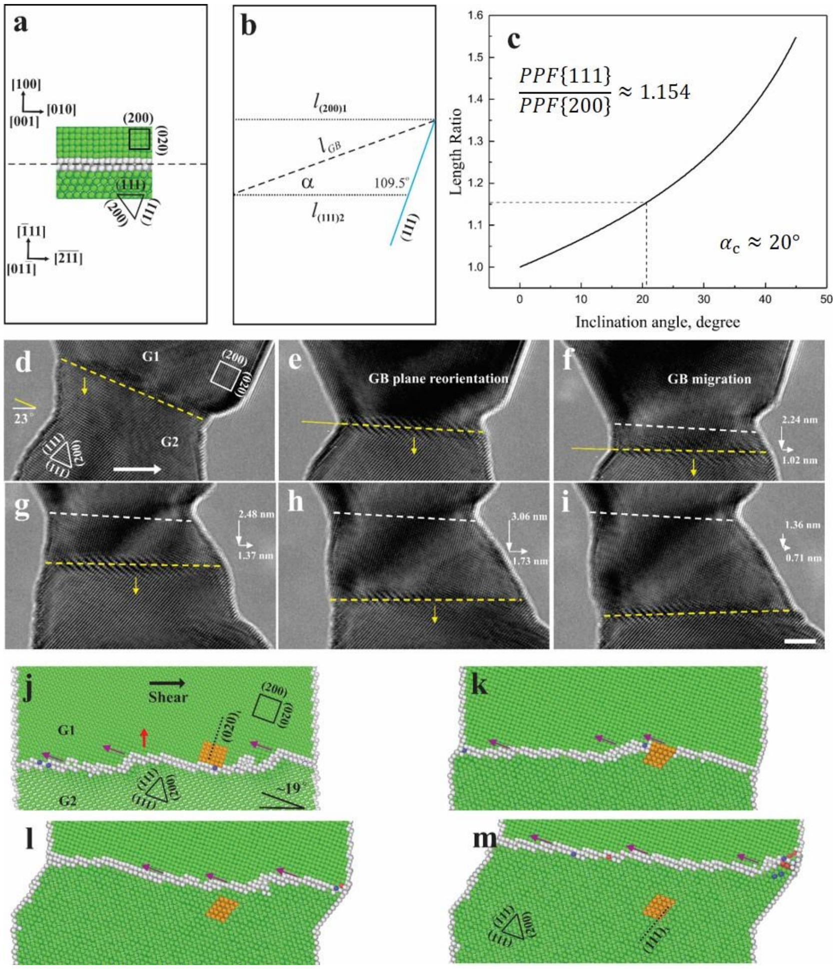
a
[100]
[010]
[001]
(200)
(020)
(111)
(200)
(111)
[$\bar{1}$11]
[2$\bar{1}\bar{1}$]
[01$\bar{1}$]
b
$l_{(200)1}$
l_{GB}
α
109.5°
$l_{(111)2}$
(111)
c
$\frac{PPF\{111\}}{PPF\{200\}} \approx 1.154$
$\alpha_c \approx 20°$
Length Ratio
Inclination angle, degree
1.0
1.1
1.2
1.3
1.4
1.5
1.6
0
10
20
30
40
50
d
G1
G2
(200)
(020)
(111)
(111)
(200)
23°
e
GB plane reorientation
f
GB migration
2.24 nm
1.02 nm
g
2.48 nm
1.37 nm
h
3.06 nm
1.73 nm
i
1.36 nm
0.71 nm
j
Shear
G1
G2
(200)
(020)
(020)
(111)
(111)
(200)
~19°
k
l
m
(111)
(111)
(200)
(111)

Figure 5.7 Geometrical analysis of the concurrent GB migration and GB sliding under shear deformation. (a, b) Schematics of bicrystals with a flat $\langle \mathbf{001} \rangle \{\mathbf{200}\}/\langle \mathbf{0\bar{1}1} \rangle \{\mathbf{\bar{1}11}\}$ GB **(a)** and with the GB plane reoriented by a certain inclination angle α **(b)**. The lengths of the atomic planes matching at the GB change with the reorientation of GB. **(b)** Plot of the length ratio between $(\mathbf{200})_{\mathbf{1}}$ and $(\mathbf{111})_{\mathbf{2}}$ planes that match at the reoriented GB plane. **(d-i)** Sequential HRTEM images showing the shear deformation of the Au bicrystal was dominated by GB migration after the GB plane reoriented to α = 23°. **(j-m)** MD simulation results showing the migration of a GB with α = 19° was accommodated by the coordinate migration of $\langle \mathbf{001} \rangle \{\mathbf{200}\}/\langle \mathbf{0\bar{1}1} \rangle \{\mathbf{\bar{1}11}\}$ GB facets. Scale bar. **(d-i)** 5 nm.

5.3 Discussion

MGBs have both tilt and twist components. A low-angle MGB is normally described as an array of edge and screw dislocations. The collective motion of these constituent dislocations accommodates the deformation of the low-angle MGB, wherein the edge dislocations contribute to GB migration whereas the screw ones cause grain rotation[28]. For the high-angle MGBs, previous simulation studies indicate that some special coincidence site lattice (CSL) MGBs, i.e., Σ3 [111] 60° boundary with {11 8 5} GB plane [195] and Σ7 [111] 38.21° MGBs[105], are faceted, stepped, or kinked at the atomic scale with the corresponding low-energy CSL symmetrical tilt GBs being the constituent GB facets or terraces. Based on the assumption that only the symmetrical tilt GB component contributes to the shear-coupled migration of MGBs, Han et. al. [7] proposed an unverified theoretical equation to predict the shear-coupling factors of MGBs. However, CSL MGBs only represent a special set of GBs. MGBs in reality are generally the non-CSL GBs with irrational GB planes [154, 160, 196]. In these general cases, the MGBs normally consist of low-energy GB facets comprised of at least one low-index plane, e.g., (100), (110), and (111) planes, instead of symmetrical tilt GB facets. Our work takes the $\langle 001\rangle\{200\}/\langle 0\bar{1}1\rangle\{\bar{1}11\}$ MGB as an case study to uncover the atomistic mechanims of the shear-coupled migration of the MGBs comprised of at least one low-index plane, and our results provide the atomic-scale experimental evidence that the migration of MGBs could be mediated by the motion of GB disconnections on the MGB plane itself instead of on its symmetrical tilt GB component.

As shown in our results, there are several striking features of the shear-coupled migration of MGBs. First, there exist distinct types of migration behavior showing the opposite signs of shear-coupling factors for the same $\langle 001\rangle\{200\}/\langle 0\bar{1}1\rangle\{\bar{1}11\}$ MGB deformed at room temperature, which arises from the activation of GB disconnections with different crystallographic parameters (Figure 5.2 and Table 5.1). As predicted by the disconnection theory, there is a broad spectrum of admissable GB disconnections with various choices of Burgers vectors and step heights for an arbitrary GB crystallographic (including the symmetrical tilt GBs) [64, 65, 67]. Although GB disconnections with different Burgers vectors and step heights for the same GB have also been observed in the migration of some symmetrical tilt GBs, these disconnections either belong to the same type with the identical shear-coupling factors [37, 88] or produce the opposite signs of shear-coupling factors but can only be activated at different temperatures [69, 86]. They are notably different from the two types of GB disconnections in MGBs that produce the opposite signs of shear-coupling factors at room temperature (Figure 5.2). Secondly, the revealed two lattice correspondence relationships, i.e., (020)-to-(111) type and (020)-to-(200) type, during the shear-coupled migration of $\langle 001\rangle_1\{200\}_1/\langle 0\bar{1}1\rangle_2\{\bar{1}11\}_2$ MGB involves the transformations between different atomic planes, which are different from what happens in symmetrical tilt GBs wherein the corresponding planes are normally identical atomic planes. For instance, shear-coupled migration of <001> tilt GBs involves the transformation of either {100} or {110} atomic planes of one lattice into the identical atomic planes of the other lattice, depending on the misorientation angle and the deformation temperature[53, 91]. Instead, they are similar to the Basal-Prismatic[137, 197] and Basal-Pyramidal[198, 199] transformations that have been extensively studied in hexagonal-close packed metals that commonly involve complex atoms shuffling. Thirdly, the unique transformation relations between different atomic planes during GB migration bring the results that the the $\langle 001\rangle\{200\}/\langle 0\bar{1}1\rangle\{\bar{1}11\}$ MGB cannot easily migrate conservatively like the symmetrical tilt GBs. GB plane reorientation and excess GB sliding shall be activated to accommdate the GB migration. The GB plane reorientation occurred via the stack of $\langle 001\rangle\{200\}/\langle 0\bar{1}1\rangle\{\bar{1}11\}$ GB nanofacets that migrated at different distances, regardless of which lattice correspondence relation the GB migration follows (Figures 5.2e-g, 5.5, and 5.7). Note that the GB plane reorientation is also found to occur during the shear-coupled migration of asymmetrical tilt GBs as reported in our recent work[149]. The excess GB sliding can be mediated by the motion of GB disconnections that have Burgers vectors but no step height [7, 200].

Admittedly, the free surface of the nano-bicrystals plays an important role in accommodating the GB migration in our cases. First, the intersection of free surface with the GB serves as the primary nucleation site for the GB disconnections (Figure 5.1). Secondly, the sample geometry (i.e., the large taper angle of free surface with the GB) could also propel the nucleation of GB disconnections or the twin [201]. In comparison, GB migration in nanocrystalline materials receives constraints from the neighboring grains. The nucleation of GB disconnections in nanocrystalline materials could either be via the homogeneous/heterogeneous nucleation of disconnection pairs[71], or occur at the GB triple-junctions[35], but not at the free surface in our case. Moreover, GB migration in nanocrystalline materials is commonly accommodated by GB junctions, the motion of which requires the net Burgers vector of disconnections into/out of the junctions to be zero [72, 100, 202]. Otherwise, other deformation mechanisms such as emission of lattice dislocations or twinning would be activated to dissipate the accumulated Burgers vectors [72, 203]. Therefore, shear-coupled GB migration in nanocrystalline materials depends largely on the local environment of the GB. For the typical case of $\langle 001\rangle_1\{200\}_1/\langle 0\bar{1}1\rangle_2\{\bar{1}11\}_2$ MGB studied here, there are multiple admissible combinations of active deformation modes in the polycrystalline environment: type-1 shear-coupled GB migration and excess GB sliding (Figures 5.1b-d, Figure 5.6); type-2 shear-coupled GB migration and excess GB sliding (Figure 5.5); and the concurrent type-1 and type-2 shear-coupled GB migration (Figures 5.1e-g). Note that cooperative GB sliding and GB migration have also been observed in the tensile deformation of an Au nanocrystalline thin film [204]. An example of MGB migration mediated by the GB triple-junction can be found in Figure 5.8. Moreover, akin to the twinning-assisted dynamic adjustment of GB mobility during the shear-coupled migration of <110> tilt GBs [40], twinning is also found to assist the transition between the two migration modes of the $\langle 001\rangle_1\ \{200\}_1/\langle 0\bar{1}1\rangle_2\ \{\bar{1}11\}_2$ type MGB (Fig. 5.9). Lastly, it is worth mentioning that temperature[75, 86], shear direction[200], and strain rate[205] could also affect the shear-coupled migration behavior of GBs. It is expected that other migration modes can be observed when these factors are varied, which undoubtedly warrant attention in future study.

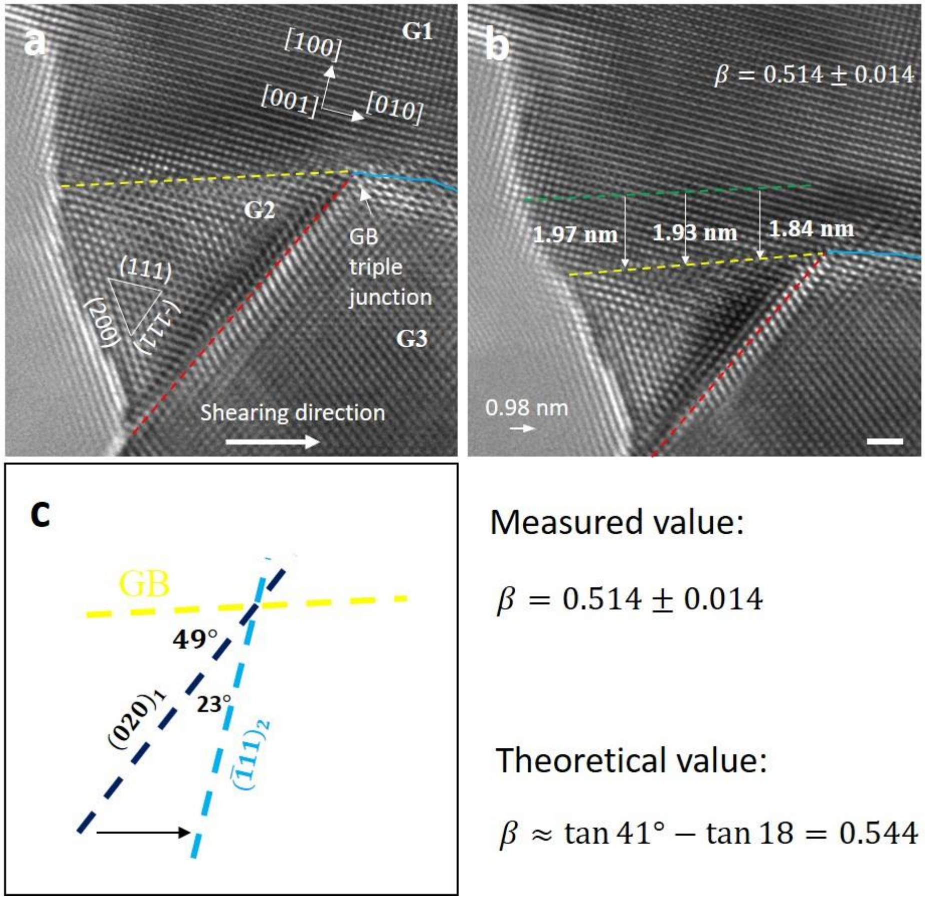
a
G1
[100]
[001]
[010]
G2
GB triple junction
(111)
(200)
(11-1)
G3
Shearing direction
b
$\beta = 0.514 \pm 0.014$
1.97 nm
1.93 nm
1.84 nm
0.98 nm
c
GB
49°
23°
$(020)_1$
$(\bar{1}11)_2$
Measured value:
$\beta = 0.514 \pm 0.014$
Theoretical value:
$\beta \approx \tan 41° - \tan 18 = 0.544$

Figure 5.8 A typical example of GB migration accommodated by the GB triple-juction. (a) as-fabricate sample with a mixed tilt twist GB$_{12}$ between $\langle\mathbf{001}\rangle$-oriented and $\langle\mathbf{01\bar{1}}\rangle$-oriented G2, and a mixed tilt-twist GB$_{13}$ between G1

and $\langle \mathbf{01\bar{1}} \rangle$-G3, and a twin boundary between G2 and G3. The misorientation relation between G1 and G2 is the same as the $\langle \mathbf{001} \rangle \{\mathbf{200}\}/\langle \mathbf{0\bar{1}1} \rangle \{\mathbf{\bar{1}11}\}$ GB, but differ at the GB plane orientation. **(b)** GB_{12} and G_{13} migrated downwards under the leftwards shear loading. The Shear -coupling factor of G_{12} is measured to be ~0.514±0.014. **(c)** Schematic illustration showing the lattice transformation relation and the calculation of corresponding theoretical value of the shear-coupling factor of G_{12}, which is $\beta \approx \boldsymbol{tan\,41° - tan\,18° = 0.544}$. Scale bar: 1 nm.

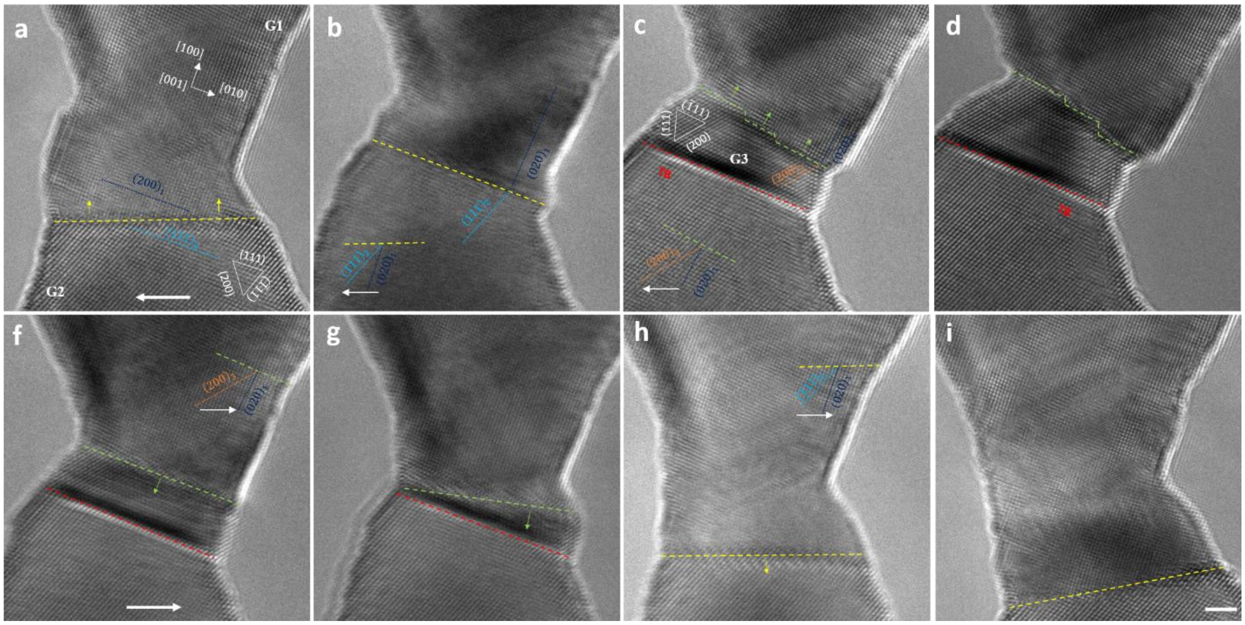

Figure 5.9 Twinning-assisted transition of lattice transformation relations during the GB migration. (a) As-fabricated Au bicrystal with a similar orientation relation to that in Figure 1. The GB plane has an inclination angle of ~20° with the $\langle \mathbf{001} \rangle \{\mathbf{200}\}/\langle \mathbf{0\bar{1}1} \rangle \{\mathbf{111}\}$ GB plane. **(b-d)** under the leftward shear loading, GB migration changed from following the $(\mathbf{020})_\mathbf{1}$-to- $(\mathbf{111})_\mathbf{2}$ type transformation relation into the $(\mathbf{020})_\mathbf{1}$-to- $(\mathbf{200})_\mathbf{3}$ transformation relation, assited by the twinning and formation of a new grain 3. **(f-i)** the reversed GB migration under the rightwards shear loading. GB migration changed from following the $(\mathbf{200})_\mathbf{3}$-to- $(\mathbf{020})_\mathbf{1}$ transformation relation into the $(\mathbf{111})_\mathbf{2}$-to- $(\mathbf{020})_\mathbf{1}$ transformation relation, assisted by the shrinkage and disappearance of G3. Scale bar: 2 nm.

5.4 Conclusion

By conducting in situ HRTEM shear testing and MD simulations, we have explored the shear-coupled migration behavior and underlying atomistic mechanisms of a typical MGB, i.e., $\langle 001\rangle_1\,\{200\}_1/\langle 0\bar{1}1\rangle_2\,\{\bar{1}11\}_2$ GB, in Au nanocrystals. The main conclusions are summarized as follows: Two distinct types of shear-coupled GB migration behavior having opposite signs of shear-coupling factors were observed at the room-temperature shear deformation of the $\langle 001\rangle_1\,\{200\}_1/\langle 0\bar{1}1\rangle_2\,\{\bar{1}11\}_2$ MGB. Both migration patterns can be mediated by the motion of one-atomic-layer GB disconnections on the MGB plane, but these disconnections have different Burgers vectors; Based on topological analysis of the crystallographic parameter of these GB disconnections, two completely different types of lattice correspondence relations, i.e., $\langle 001\rangle\{020\}$ -to- $\langle 0\bar{1}1\rangle\{200\}$ type and $\langle 001\rangle\{020\}$ -to- $\langle 0\bar{1}1\rangle\{111\}$ type, during the MGB migration, were proposed and then verified by the MD simulations. Except for the shear displacement of atoms, complex atom shuffling is needed in both cases to complete the lattice transformation; GB plane reorientation and excess GB sliding were observed to accommodate the shear-coupled migration of the MGB regardless of which lattice correspondence relation it follows. A simplified geometrical model, derived from the principle of point-to-point lattice correspondence during GB migration, is proposed to account for the necessity of these extra mechanisms to eventually achieve the conservative migration of this MGB; Our findings not only provide direct experimental evidence on the disconnection-mediated migration of MGBs and the atomistic understanding of the lattice transformation during the migration of MGBs, but also show that the shear response of MGBs is much more complex than that of symmetrical tilt GBs in a way that multiple deformation mechanisms, e.g., different shear-coupled migration modes, GB plane reorientation, and excess GB sliding, could be cooperatively activated. Given that MGBs comprised of at least one low-index plane wildly exist in face-centered cubic polycrystals, the observed phenomena and uncovered mechanisms should have general implications for a wide range of GBs and may provide guidance for tailoring the mechanical properties of nanocrystalline materials through GB engineering.

6.0 In-situ Observation of Formation and Annihilation of a HAGB in an Au Nanocrystal

In this Chapter, the dynamic process of the deformation-induced formation and annihilation of a typical HAGB will be investigated. Nanocrystalline materials prepared by severe plastic deformation often show superior strength owing to formation of a large number of deformation-induced grain boundaries (GBs), particularly high-angle GBs (HAGBs). To date, the dynamic process of HAGB formation and the deformation behavior of as-formed HAGB remain elusive. Here we performed in-situ HRTEM study to reveal the dynamic formation and annihilation process of a $(311)/(111)$ HAGB in a gold nanocrystal upon reciprocating bending deformation. Our results revealed that HAGB formation underwent the process of accumulation, alignment, and exhaustion of geometrically necessary dislocations. In comparison, HAGB annihilation was accomplished by synergic operation of GB structure reconstruction, emission of partial and full dislocations, and twinning. Such synergic mechanisms were further confirmed by MD simulations. This work provides atomistic insights on grain refinement mechanism and application of nanocrystals through mechanically controlled GB structure.

6.1 Introduction

Metallic nanocrystalline materials often show exceptional mechanical properties such as high strength and hence are very attractive for structural applications in the areas of transportation, medical implants, micro- and nano-electromechanical systems [107, 206, 207]. One fabrication approach of metallic nanocrystalline materials is to use severe plastic deformation to achieve intensive grain refinement in the bulk counterparts [208]. Consequently, comprehensive understanding of the grain refinement mechanisms is crucial for optimizing the fabrication strategies of nanocrystalline materials. Previous studies have utilized the post-mortem observation of deformed samples to deduce the microstructural evolution of metallic materials during severe plastic deformation [110, 112, 209], particularly on grain subdivision via the formation of deformation-induced grain boundaries [209]. It is well-recognized that the number of deformation-induced GBs and the fraction of high-angle GBs (HAGBs) in overall GBs would largely increase with strain accumulating [111, 113], implying the formation of low-angle GBs (LAGBs) first and subsequent LAGB-to-HAGB transformation during the deformation process. With the development of in-situ TEM techniques, the dynamic process of deformation-induced formation of LAGBs have been recently investigated at the atomic scale through the non-uniaxial deformation, e.g., bending, of fcc Ni [134] and Au [124, 133] nanowires. The LAGBs has been revealed to form either via pile-up of full dislocations [124, 134] or assisted by the formation of nanotwins[133]. Moreover, the formation process is fully reversible after loading release [124] or upon reciprocating shear load [133]. By contrast, how these LAGBs transform into HAGBs during accumulating deformation has not been fully studied yet. In addition, HAGBs could be preferable nucleation sites for dislocations[88, 117], deformation twinning[118], and phase transformation[119]. The annihilation mechanism of HAGB could be more complex than that of LAGB, which however has not been fully explored.

In present study, by performing in-situ HRTEM combined with MD simulations, we revealed the dynamic formation and annihilation processes of a $[0\bar{1}1]$ tilt $(311)/(111)$ 29.5° HAGB during the reciprocating bending deformation of a gold (Au) nanowire at the atomic scale. Our results indicate that the formation of the HAGB was via the accumulation and exhaustion of lattice dislocations, whereas the annihilation of the HAGB was not simply a reversal process of formation but accommodated by synergic operation of GB structure reconstruction, emission of partial dislocations, and deformation twinning.

6.2 Experimental Results

6.2.1 Dynamic Process of the Deformation-induced Formation of a HAGB

Figure 6.1a shows the HRTEM image of the pristine Au nanocrystal with the zone axis of $[0\bar{1}1]$. Upon mechanical loading on the nanocrystal along $[3\bar{1}\bar{1}]$ direction, plenty of geometrically necessary dislocations (GNDs) [210] with Burgers vectors of $\frac{1}{2}[0\bar{1}\bar{1}]$, $\frac{1}{2}[101]$, or $\frac{1}{2}[110]$ were generated to mediate the lattice rotation (Figs. 6.1b and 6.1c). Note that not all GNDs can be marked out due to the existence of lattice distortion. Hitherto, it is akin to what happened during the bending deformation of nickel nanowires that GNDs accommodate the lattice rotation [134]. When the lattice rotation resulted from the applied bending deformation approached ~20°, the GNDs collectively moved and were aligned to form a curved GB vicinal to the $(211)/(111)$ GB plane (Fig. 6.1d). It should be mentioned that the alignment of GNDs could reduce the total energy of the system by overlapping the stress fields of the GNDs and the dislocation-based <011> tilt GBs could stably exist in nanocrystals when the GB misorientation angle does not exceed 24°[38, 211]. Thereafter, as shown in Figures 6.1e and 6.1f, the subsequent bending deformation was accommodated by the nucleation and accumulation of additional GNDs in the upper grain G1, forming a severe-deformed transition region (enclosed by the yellow dashed lines in Fig. 6.1f). However, with the deformation further accumulating, this transition region suddenly shrank (Figs.

6.1g and 6.1j) and a nearly flat $(311)/(111)$ GB was formed when the lattice rotation angle of the bottom grain reached ~30° (Fig. 6.1i). Meanwhile, lattice strain was largely released after the GB formation, as evidenced by the transformation of curved lattice planes in Fig. 6.1h into straight ones in Fig. 6.1i. Therefore, the formation of $(311)/(111)$ GB underwent the dynamic process of accumulation (Figs. 6.1a-c), alignment (Fig. 6.1d), further accumulation (Fig. 6.1f), and later exhaustion (Figs. 6.1g-i) of GNDs, wherein the first two steps led to the LAGB formation while the following two steps caused the LAGB-to-HAGB transformation. The tendency to form $(311)/(111)$ GB instead of other GBs is likely due to its low GB energy, as compared with $(211)/(111)$ GB and other typical coincidence-site lattice GBs with close misorientation angles, e.g., $\mathit{\Sigma}19\ \{116\}\ STGB - 26.53°$ and $\mathit{\Sigma}27\ (115)\ STGB - 31.59°$ (see Table 6.1). Next, considering that the annihilation process of (311)/(111) GB was observed to be more complex than its formation process, the remaining parts would focus on the GB annihilation process.

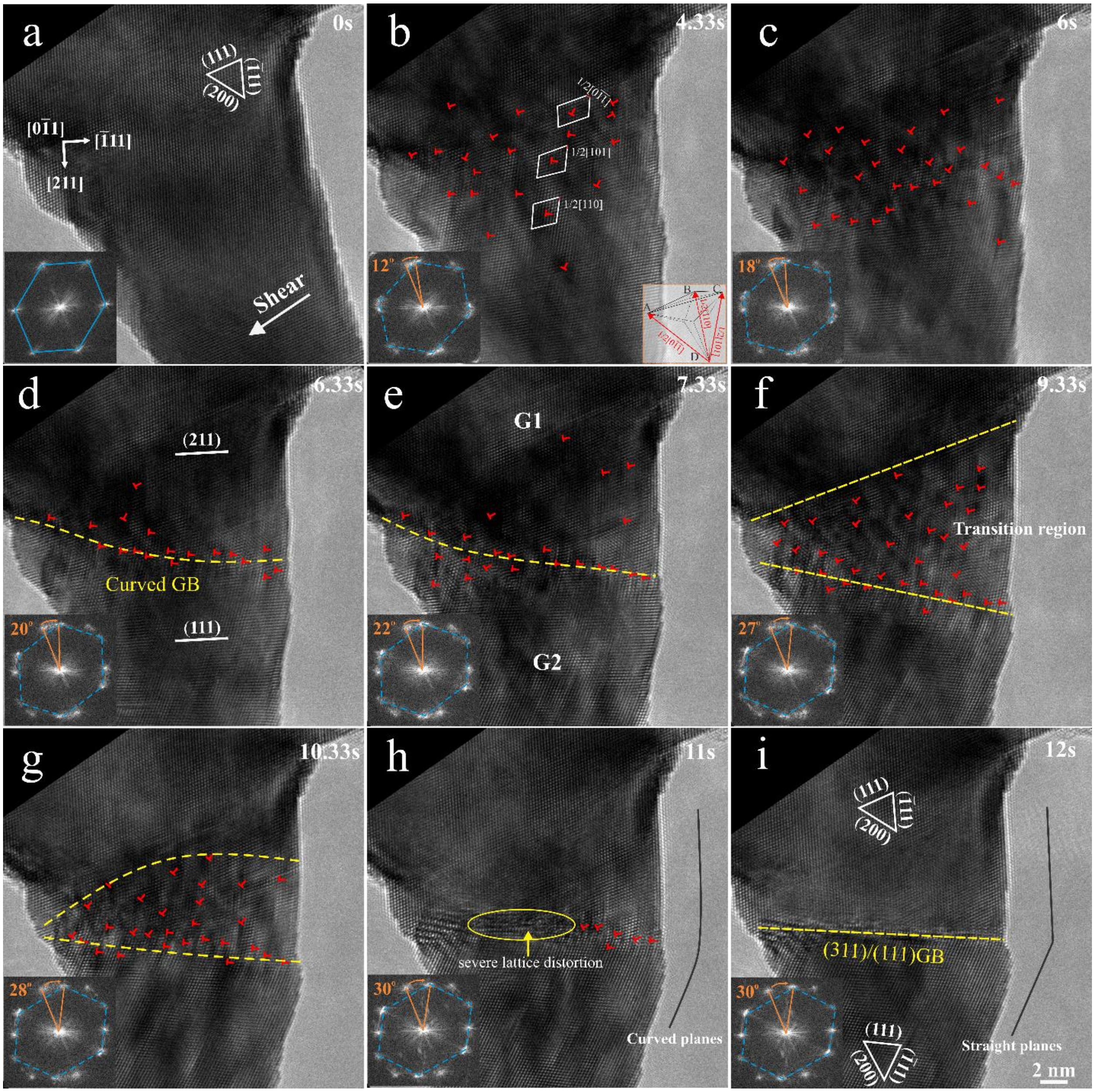
a
0s
(111)
(200)
(111)
[0$\bar{1}$1]
[$\bar{1}$11]
[211]
Shear
b
4.33s
1/2[0$\bar{1}$1]
1/2[101]
1/2[110]
12°
A
B
C
D
c
6s
18°
d
6.33s
(211)
Curved GB
(111)
20°
e
7.33s
G1
G2
22°
f
9.33s
Transition region
27°
g
10.33s
28°
h
11s
severe lattice distortion
Curved planes
30°
i
12s
(111)
(200)
(111)
(311)/(111)GB
Straight planes
30°
2 nm

Figure 6.1 Formation process of a $\langle 0\bar{1}1\rangle$-tilt $(311)/(111)$ GB in an Au nanowire upon bending deformation. (a) Pristine Au nanocrystal. (b, c) Nucleation and accumulation of GNDs to accommodate lattice rotation. (d) Alignment of GNDs to form a curved GB. (e, f) Additional GNDs formed during subsequent bending deformation. (g, f) The GNDs and the curved GB collapsed to form the (311)/(111) GB. Inserts in the left-bottom of (a-i) and the right-top of (b) are corresponding fast Fourier transformation (FFTs) patterns and the schematic of Thompson tetrahedron, respectively.

Table 6.1 Theoretically calculated GB energy of different GBs based on GB energy function for FCC metals*[212]*

GB type	GB energy (mJ/m^2)
$(311)/(111)$ ATGB-29.5°	286.5
$(211)/(111)$ ATGB-19.5°	394.1
$\Sigma 19\ (116)$ STGB-26.53°	356.6
$\Sigma 19\ (331)$ STGB-26.53°	435.2
$\Sigma 27\ (115)$ STGB-31.59°	343.8
$\Sigma 27\ (552)$ STGB-31.59°	437.2

6.2.2 Fully Annihilation of the As-formed HAGB Upon Reversal Deformation

To trigger the annihilation of $(311)/(111)$ HAGB, reversed mechanical loading was then applied on the as-deformed nanocrystal, as presented in Figure 6.2. At the incipient deformation stage, the lattice rotation was likely mediated by the GB structure reconstruction, which may involve the emission of lattice dislocations from the GB (will be discussed later in Fig. 6.3). As seen in Figures 2a and 2b, the lattice disorder at the GB region (Fig. 6.2a) was largely released when a $(311)/(111)$ HAGB was transformed into a (944)/(111) GB with a misorientation angle of ~23° (Fig. 6.2b). Thereafter, two chevron regions, enclosed by the intersected GB (yellow dashed lines) and twin boundary (red dashed lines), at the side surfaces and an extended GB region at the middle (as enclosed by the white dashed circle) of the bicrystal were formed when the misorientation angle was further reduced to ~20° (Fig. 6.2c). The chevron regions could be the product of GB dissociation [149], e.g., 19.5°(112)/(111) GB→ 90°(111)/(11-2) GB + 70.5° (11-

1)/(111) GB, and help to maintain the continuity of the nanowire [213]. In comparison, the extended GB region could result from the dissociation of GB dislocations, that is a full dislocation dissociated into two partial dislocations bonded by a stacking fault (SF)[38, 214]. Further bending deformation caused the formation of deformation twins at the compression region, SFs at the tensile region, and lattice dislocations with Burgers vectors of $\frac{1}{2}[0\bar{1}\bar{1}]$, $\frac{1}{2}[101]$, or $\frac{1}{2}[110]$ at the region near neutral plane of the nanowire (Fig. 6.2d). Those SFs were later eliminated and the number of lattice dislocations also reduced, accommodating the further decreasing of misorientation angle into ~4° (Fig. 6.2e). Note that there may remain residual SFs at the inclined $\{111\}$ planes in the inner of nanowire due to the movement of transverse partial dislocations [215], as reflected by the lattice displacement shown in the insert of Figure 6.2e. Thereafter, detwinning occurred and the nanowire changed back into its pristine crystal structure (Fig. 6.1a) with slight change on the surface morphology (Fig. 6.2f).

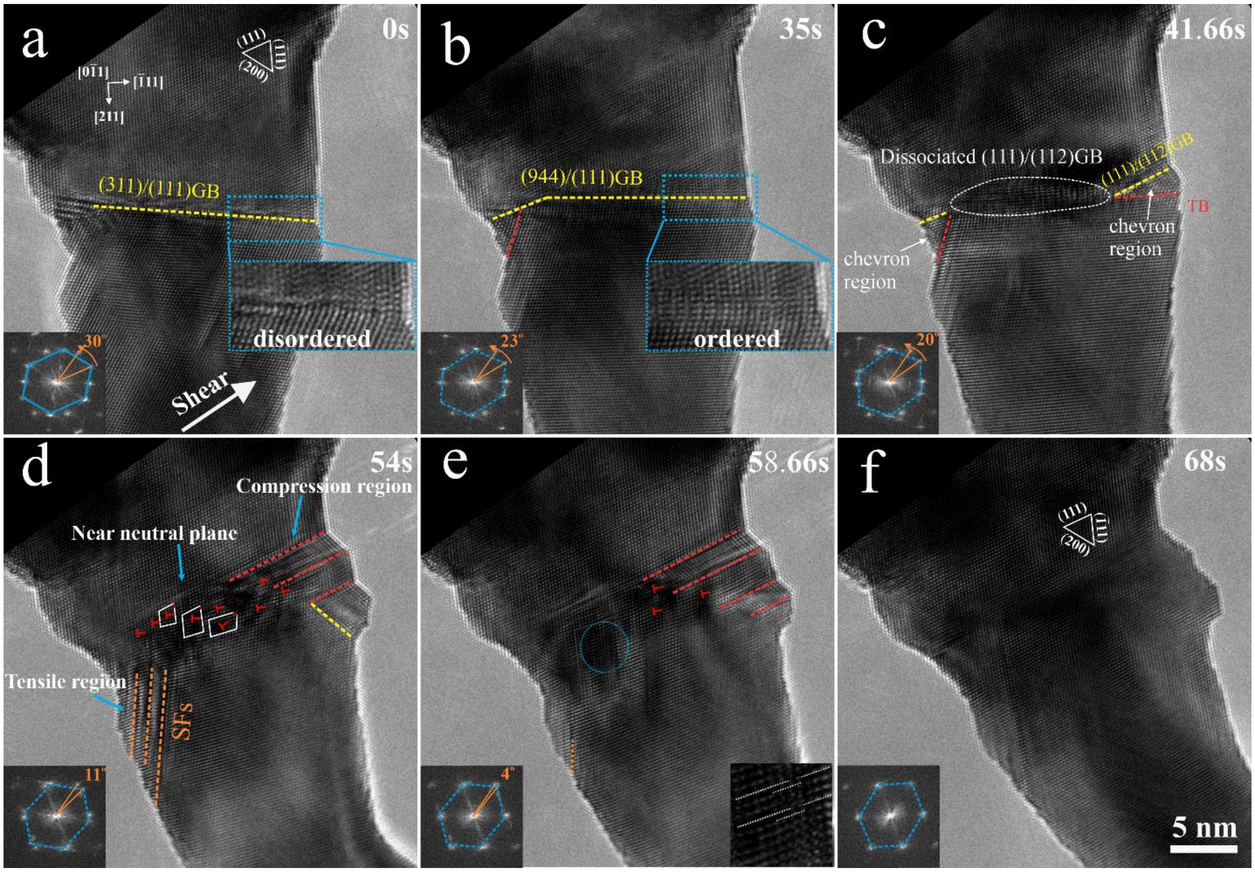
a
0s
[0$\bar{1}$1]
[$\bar{1}$11]
[211]
(111)
(200)
(311)/(111)GB
disordered
30°
Shear
b
35s
(944)/(111)GB
ordered
23°
c
41.66s
Dissociated (111)/(112)GB
(111)/(112)GB
TB
chevron region
chevron region
20°
d
54s
Compression region
Near neutral plane
Tensile region
SFs
11°
e
58.66s
4°
f
68s
(111)
(200)
5 nm

Figure 6.2 Annihilation process of a (311)/(111) GB in an Au nanowire upon reversed bending deformation. (a, b) Lattice rotation mediated by GB structure reconstruction until the GB transformed into a (**944**)/(**111**) GB (c) GB dissociation to form two chevron regions. (d) Further GB annihilation by emission of SFs, twinning, and GB structure reconstruction into GNDs. (e) The elimination of the SFs and GNDs. Residual SFs on inclined {111} plane may still exist, as shown in the enlarged view in the insert. (f) Fully annihilation of the GB. Inserts in the left-bottom of (a-f) are corresponding fast Fourier transformation (FFTs) patterns of the nanowire.

Unlike the annihilation of mechanically formed LAGBs that are mediated only by the movements of GB dislocations, the annihilation of HAGBs involves the synergic operation of multiple deformation mechanisms, e.g., GB structure reconstruction, emission of partial and full dislocations, and deformation twinning. To further clarify these deformation mechanisms, detailed analysis was performed as presented in Figures 6.3 and 6.4. Figure 6.3 shows the structural evolution during the (311)/(111) GB-to-(944)/(111) GB transformation (Figs. 6.2a and 6.2b).

As seen in Figures 6.3a-c, the lattice rotation at the incipient stage, i.e., 29° to 26°, was mainly mediated by GB structure reconstruction but was also accompanied by the interaction of residual dislocation with the GB. Subsequently, emission of dislocation from the lattice distortion region near the GB was detected, as evidenced by the disappearance of a surface step after the deformation (Figures 6.3d-f). Thereafter, as shown in Figures 6.4a and 6.4b, a deformation twin was emitted from a strain contrast region where may exist severe lattice distortion. The twinning process was accompanied by the shrinkage of the dissociated GB region (enclosed by the white dashed circle) and the emission of a SF (the orange dashed line) from the GB. It is believed that the emission of deformation twin and SF helped the release of accumulated lattice strain at the GB, which consequently led to the shrinkage of dissociated GB region. Comparison between Figures 6.4b and 6.4c reflects that further deformation caused the reconstruction of the dissociated GB into the GB consisting of lattice dislocations (Fig. 6.4c). Meanwhile, additional SFs were emitted from another lattice distortion region near GB, as that a more ordered lattice structure was observed in the lattice distortion region after the emission of SF (see inserts in Figs. 6.4c and 6.4d). The SFs were likely to be eliminated by the nucleation and movement of trailing partial dislocation during the subsequent deformation [139, 216, 217]. Moreover, given that the existing lattice dislocations are like-signed dislocations, the decrease of the number of these lattice dislocations is more likely due to the escape of these dislocations to the free surface instead of the annihilation of different-signed dislocations (Fig. 6.4f). The above analysis indicates that the as-formed HAGB could be the preferable nucleation site of partial dislocations and deformation twins due to local strain concentration, which agrees with previous studies reporting that the emission of partial dislocations [88, 117] and deformation twins [40, 218] from the GBs are commonly observed in deformation of low SF energy materials such as Au, Ag, and Cu.

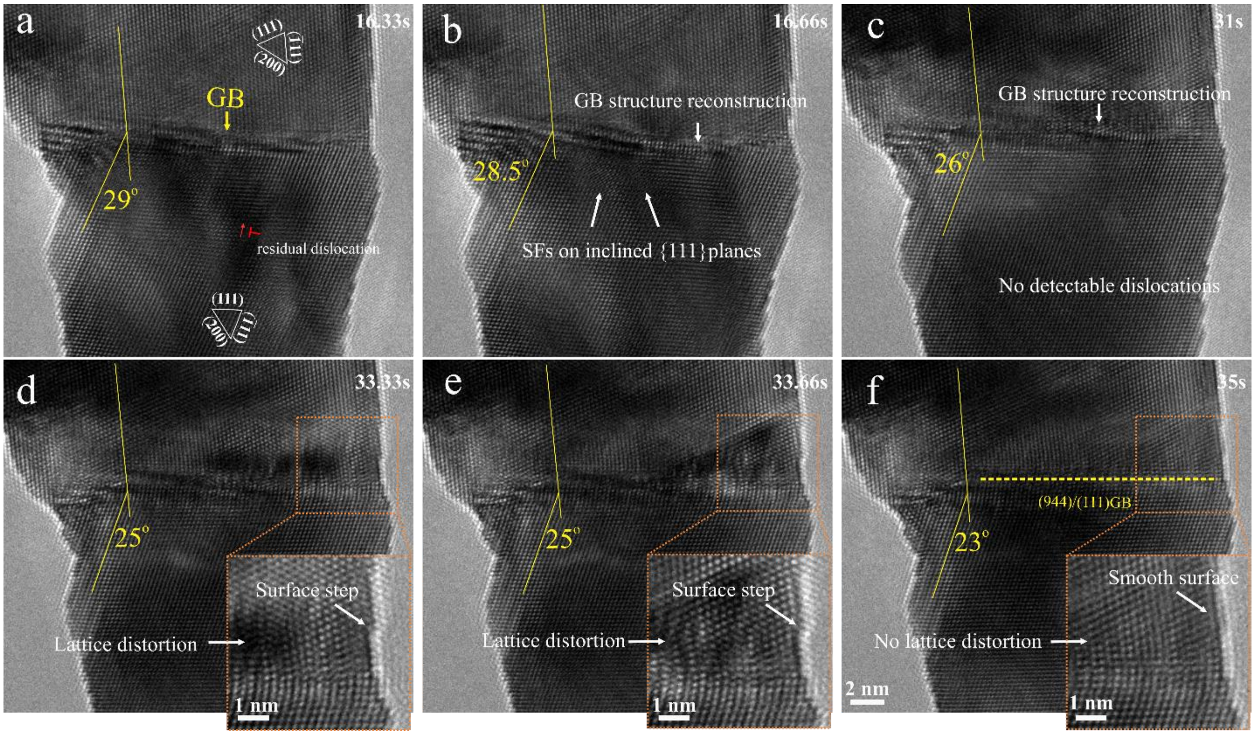
a
16.33s
(111)
(111)
(200)
GB
29°
residual dislocation
(111)
(200)
(111)
b
16.66s
GB structure reconstruction
28.5°
SFs on inclined {111}planes
c
31s
GB structure reconstruction
26°
No detectable dislocations
d
33.33s
25°
Surface step
Lattice distortion
1 nm
e
33.66s
25°
Surface step
Lattice distortion
1 nm
f
35s
(944)/(111)GB
23°
Smooth surface
No lattice distortion
2 nm
1 nm

Figure 6.3 HRTEM images showing the GB structure reconstruction and dislocation activity at the incipient stage of deformation. (a-c) GB structure reconstruction during the deformation, as reflected by the variance of GB structure. Residual dislocation in (a) also interacted with the GB. (d-f) Continuous GB structure reconstruction accompanied by the release of lattice distortion on the GB and a dislocation event occurred near the GB and the free surface. Inserts in (d-f) are enlarged views to show the occurrence of the dislocation event causing the disappearance of the surface step.

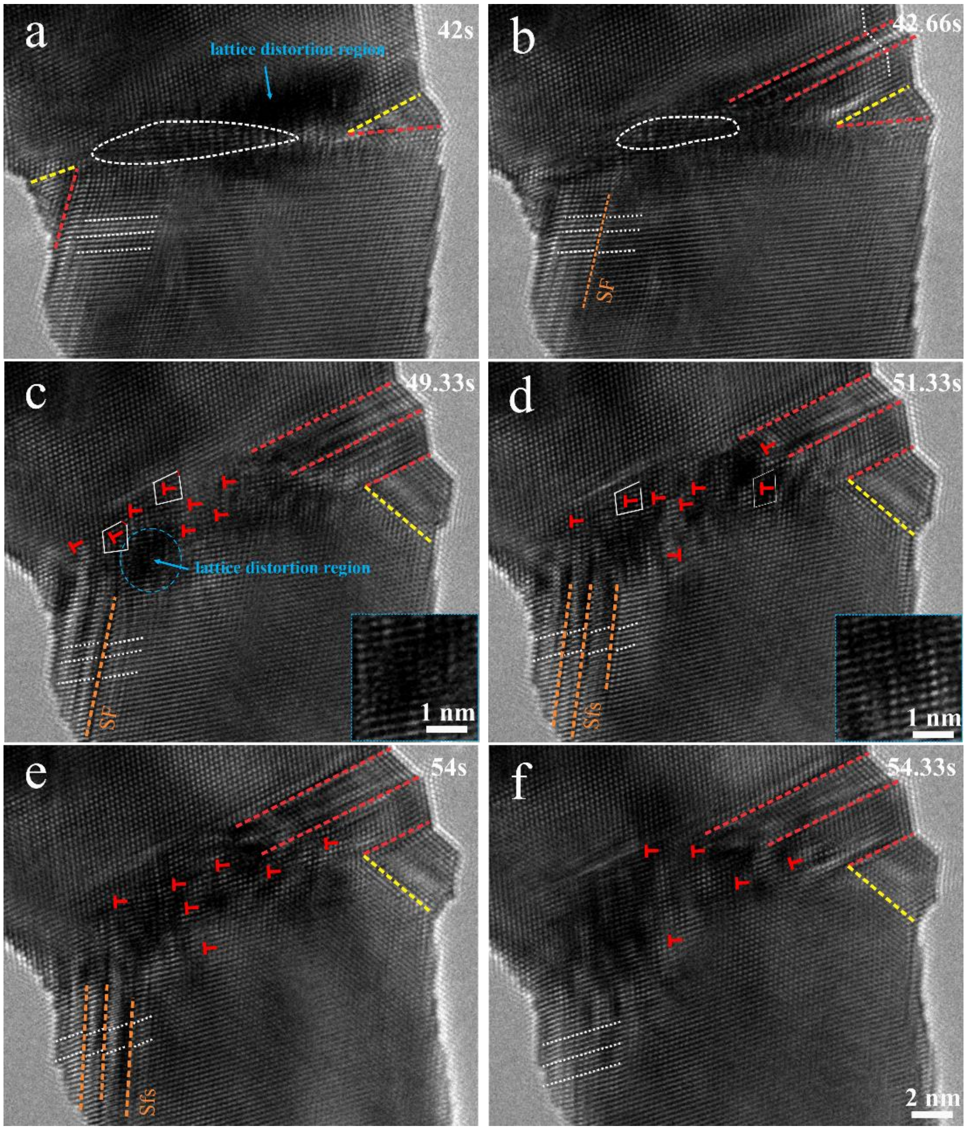
a
42s
lattice distortion region
b
42.66s
SF
c
49.33s
lattice distortion region
SF
1 nm
d
51.33s
SFs
1 nm
e
54s
SFs
f
54.33s
2 nm

Figure 6.4 HRTEM images showing the synergic mechanisms accommodating GB annihilation. (a, b) Nucleation of twin and SF from the GB, accompanied by the shrinkage of extended GB region. (c, d) Additional SFs nucleated from the GB and GB structure reconstructed into GNDs. (e, f) SFs eliminated during subsequent deformation, along with the decreasing quantity of GNDs. Inserts in (c, d) were enlarged from the lattice distortion region as enclosed by the blue dashed circle.

6.2.3 MD Simulation Results of HAGB Annihilation

It is noted that HRTEM images are phase-contrast two-dimensional views, which means the structural change within the nanowire would be hard to be resolved, especially when deformation occurs on inclined lattice planes. Therefore, we performed MD simulations to further gain insight into the atomistic process of GB annihilation. The visualization of MD results was performed in OVITO [148] using the common neighbor analysis modifier to identify the GB/surface atoms and the atoms in different atomic structures, i.e., the face-centered cubic, body centered cubic, and hexagonal close-packed crystal structures are colored in green, blue, and red, respectively. Figures 6.5a-c presents the MD snapshots in which a $(311)/(111)$ HAGB fully annihilated after the bending deformation. Consistent with the experimental results (Figs. 6.2, 6.3 and 6.4), the GB annihilation process was mediated by GB structure reconstruction (Figs. 6.5d-h), twinning/detwinning (Figs. 6.5i-m), and emission of SFs from the GB (Figs. 6.5n-p). As shown in Figures 6.5d-h, the GB at the tension region underwent the structure reconstruction from a relatively ordered structure (Fig. 6.5d) into a more disordered structure (Fig. 6.5e) and later into a slightly dissociated lattice dislocation (Figs. 6.5f-h). Meanwhile, leading partial dislocations were also emitted from the GB at the tension region, causing the formation of SFs on both inclined (SF1) and edge-on (SF2) {111} planes (Fig. 6.5o). The areas of those SFs were later reduced by the following emission of trailing partial dislocation from the GB and the cross-slip of one of the trailing partial dislocations led to the formation of deformation-induced SF tetrahedra (SFT) inside the nanowire (Fig. 6.5p)[219]. It needs to mention that the SFT was not detected in our experiments, the formation of which could be related to the high deformation speed employed in the MD simulations. In comparison, the deformation twin was found to form in the compression region via the well-known mechanism of twinning partial dislocations gliding on every {111} planes (Figs. 6.5i-k). Further lattice rotation arising from the bending deformation led to the occurrence of detwinning (Figs. 6.5k-m), which was mediated by the emission of twinning partial dislocations from the twin head, e.g., $(\bar{1}11)/(111)$ GB in Figure 6.5k. The above MD simulation results further confirm the synergic mechanism that mediates the HAGB annihilation.

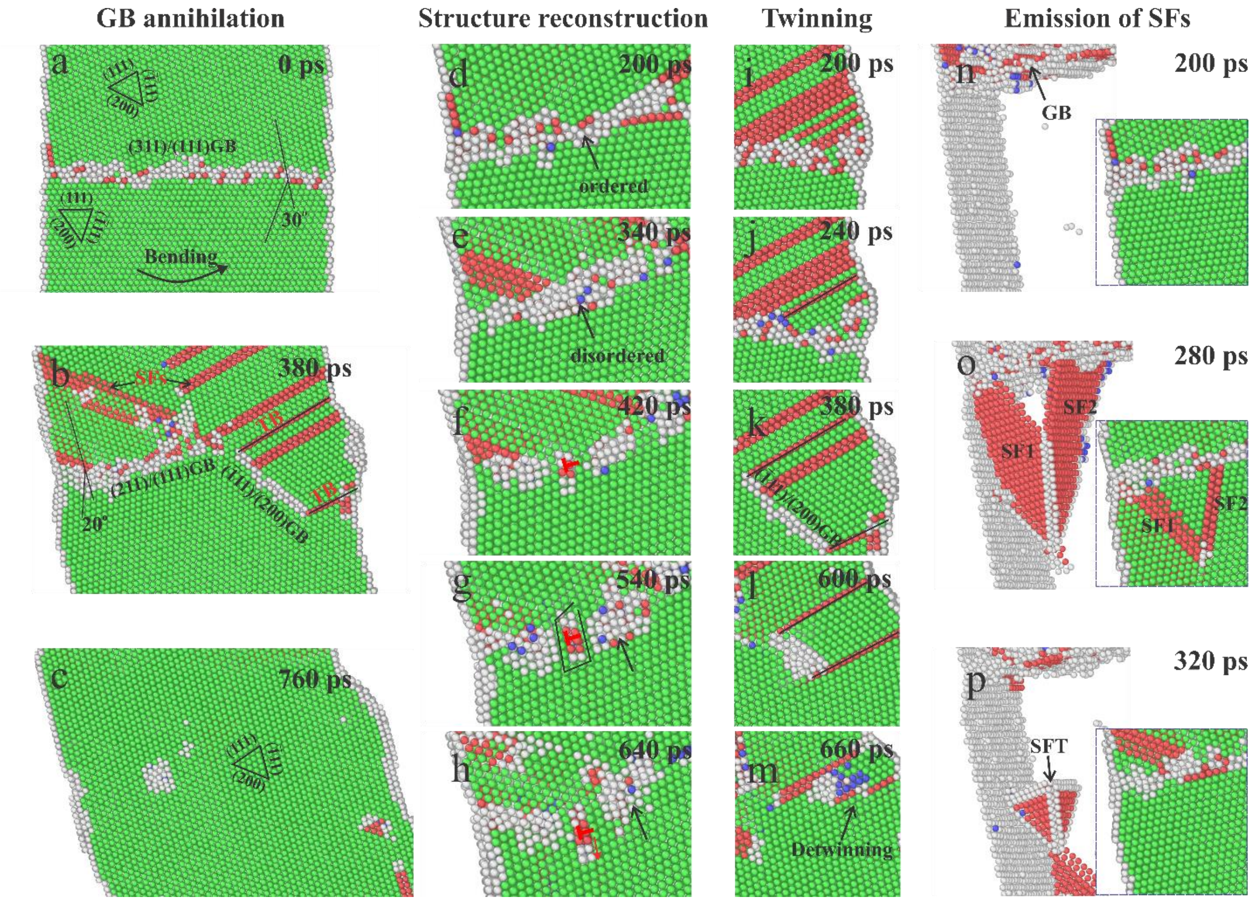

GB annihilation
Structure reconstruction
Twinning
Emission of SFs
a
0 ps
(111)
(111)
(200)
(311)/(111)GB
30°
Bending
b
380 ps
SFs
TB
(211)/(111)GB
(111)/(200)GB
20°
c
760 ps
(111)
(111)
(200)
d
200 ps
ordered
e
340 ps
disordered
f
420 ps
g
540 ps
h
640 ps
i
200 ps
j
240 ps
k
380 ps
(111)/(200)GB
l
600 ps
m
660 ps
Detwinning
n
200 ps
GB
o
280 ps
SF1
SF2
SF1
SF2
p
320 ps
SFT

Figure 6.5 MD simulation of $(311)/(111)$ GB annihilation in an Au nanowire upon bending deformation. (a-c) Typical snapshots showing the GB annihilation process. (d-h) Snapshots showing the GB structure reconstruction during GB annihilation. (i-m) Snapshots showing the twinning and detwinning process during GB annihilation. (n-p) Snapshots showing the nucleation, interaction, and elimination of SFs during GB annihilation. Note that FCC atoms (in green) in (n-p) were not shown and the sample was slightly tilt to visualize the SFs. Inserts in (n-p) show the crystal structure before modification.

6.3 Discussion

Based on the classical GB theory, LAGBs can be described by Frank-bilby dislocations [56, 220] while HAGBs are believed to be consisted of GB structural unit [221]. The reversible deformation-induced formation of LAGBs is known as being mediated by the reversible movement of component dislocations[124]. In comparison, the formation of HAGB observed here could exhaust the deformation-induced lattice dislocations and release the lattice strains (Figs. 1g-i), leading to the dynamic recovery of the sample. Unlike conventional dynamic recovery mechanisms that involve the dislocation collapse reactions and dislocation dipole climb collapse [222], the dynamic recovery observed here is likely to be mediated by the transformation of dislocation-based LAGB into structural-unit-based HAGB. Moreover, the dynamic recovery process is not continuous, but suddenly occurred when the misorientation angle reached ~30° where there exists a low-energy $(311)/(111)$ HAGB. Recent studies revealed that GB energy, instead of GB curvature, drives the thermal-induced GB migration in metallic materials [163, 223].Consequently, our results indicate that GB energy is an important factor affecting the mechanically-induced formation of HAGB. Therefore, optimizing the GB network by mechanically introducing more low-energy GBs might be a practical method to develop thermal-stable metallic nanocrystals in the future. In addition, it needs to mention that partial dislocations and deformation twinning are prevalent deformation modes in low-SF-energy materials. In contrast, deformation of materials with high SF energy such as Ni [134] and Pt [196] is commonly mediated by activities of full dislocation. Consequently, HAGB annihilation in high-SF-energy materials might be mediated by GB structure reconstruction combined with emission of full dislocations, which warrants further investigation. Moreover, it notes that the GB deformation in polycrystalline materials receives constraints from neighboring grains, how the GB annihilation process interacts with neighboring grains, e.g., dislocation-GB interaction and twin-GB interaction [39], should be considered. Lastly, arising from the different GB atomic structure, LAGBs and HAGBs may show different physical properties, including mechanical properties [1, 53, 224], electrical properties [211, 225, 226], and radiation resistance. For instance, the activation enthalpy of mechanical-driven GB migration experiences a conspicuous drop when the misorientation angles of the GBs increased to the HAGB region [224]; HAGBs usually have a higher electrical resistivity than LAGBs [211, 225, 227]. Therefore, this work would also provide guidelines on mechanically controlling the formation of GBs and the transformation between LAGBs and HAGBs to dynamically regulate the properties of nanocrystals, particularly that of nanowires, which may inspire the application of metallic nanocrystals in micro- and nano-electromechanical systems.

6.4 Conclusion

In summary, an atomic-scale observation on the formation and annihilation of the (311)/(111) HAGB in Au nanowire was conducted using in situ HRTEM mechanical testing. The GB formation process underwent the accumulation, alignment, and exhaustion of GNDs to eventually form the (311)/(111) HAGB. GB energy is an important factor affecting the formation of the HAGB. In comparison, HAGB annihilation is not simply a reverse process of formation but accommodated by the synergic operation of GB structure reconstruction, emission of partial and full dislocation, and twinning/detwinning, as further confirmed by the MD simulations. This work reveals the mechanisms of the mutual transformation between LAGB and HAGB, which provides new insights into the grain refinement mechanisms during severe plastic deformation and the application of metallic nanocrystals through mechanically controlled GB structure.

7.0 Summary and Conclusions

GBs are ubiquitous interfaces in polycrystalline and nanocrystalline materials and greatly influence the mechanical behavior of these materials. This dissertation employed in-situ HRTEM observation combined with MD simulation to reveal the atomic-scale dynamic process of the shear-coupled migration of faceted ATGBs and general MGBs, as well as the atomistic mechanism of the deformation-induced formation and annihilation of HAGB in FCC gold nanocrystals.

Regarding the case of faceted ATGBs, the shear-coupled GB migration was found to undergo the dynamic GB structural transformation during the migration. The dynamic GB structural transformation was either mediated by GB facet transformation or GB dissociation, depending on the core structure of steps/disconnections mediating the migration of the GB facets. Moreover, the origin of the reversible facet transformation was attributed to the facet/de-faceting transformation between different GB facets, which consequently determines the loading dependence of the facet transformation. The discovery of dynamic GB structural transformation during the shear-mediated migration will advance our understanding of the complexity of GB migration and provides insight into the development of nanocrystalline materials with microstructure control through thermal-mechanical processing.

Regarding the case of MGBs, the shear-coupled GB migration was confirmed to be mediated by the activation and motion of GB disconnections. GB disconnections with different crystallographic parameters could be activated and consequently led to the occurrence of distinct types of GB migration and lattice correspondence relations. Moreover, GB plane reorientation and excess GB sliding were observed to accommodate the shear-coupled migration of the MGB regardless of which lattice correspondence relation it follows. A simplified geometrical model, derived from the principle of point-to-point lattice correspondence during GB migration, is proposed to account for the necessity of these extra mechanisms to eventually achieve the conservative migration of this MGB. These findings not only provide direct experimental evidence on the disconnection-mediated migration of MGBs and the atomistic understanding of the lattice transformation during the migration of MGBs, but also show that the shear response of MGBs is much more complex than that of symmetrical tilt GBs in a way that multiple deformation mechanisms, e.g., different shear-coupled migration modes, GB plane reorientation, and excess GB sliding, could be cooperatively activated.

The deformation-induced formation and annihilation of GBs are closely related to grain refinement and grain growth during the plastic deformation of polycrystalline materials. However, compared to LAGBs, the deformation-induced formation and annihilation mechanism of HAGB remains largely unclear to date. Take the $(311)/(111)$ HAGB as the case study, it is found that the HAGB formation process underwent the accumulation, alignment, and exhaustion of GNDs to eventually form the $(311)/(111)$ HAGB. GB energy is found to determine the selection of the HAGB. In comparison, HAGB annihilation is not simply a reversal process of formation but accommodated by the synergic operation of GB structure reconstruction, emission of partial and full dislocation, and twinning/detwinning, as further confirmed by the MD simulations.

In summary, this dissertation advances the fundamental understanding of the shear-coupled migration behavior and mechanism of faceted ATGBs and MGBs as well as the deformation-induced formation and annihilation of HAGB in FCC gold nanocrystals. These findings provide insights into tailoring the mechanical properties of nanocrystalline materials through GB engineering.

8.0 Outlook

In this dissertation, the atomic-scale dynamic process of the shear-coupled GB migration and the deformation-induced formation and annihilation of HAGB in FCC gold nanocrystals were investigated. It needs to mention again that gold was selected as the model material for the in-situ HRTEM study due to its excellent oxidation resistance and moderate SF energy. In FCC crystals, SF energy is an important factor affecting the activation of partial dislocations and deformation twins, thus having potential effects on GB deformation behavior. There may exist different GB deformation behavior in other FCC metals with different SF energies, such as Ag and Pb which have lower SF energies as well as Ni, Al, and Pt which have higher SF energies than Au, which warrants further study in the future. Moreover, this dissertation focused on the room-temperature deformation of elemental gold. The effects of temperature and alloying have not been considered, which however are highly related to the performance of FCC metals in real applications. In this chapter, future directions in related fields and an example of current research will be discussed.

The GB structural transformation studied in the dissertation involves the change of GB crystallographic parameters, e.g., misorientation angle and/or inclination angle. In comparison, there exists another type of GB structural transformation that alters GB atomic structure but does not change its crystallographic parameters, which is defined as “congruent” GB structural transformation[93]. For a long time, the “congruent” GB structural transformation was believed to easily occur in alloys but rarely occur in elemental metals. For instance, segregation of Bi atoms in the GB was found to lead to the formation of a bilayer interfacial phase in a Bi-doped polycrystalline Ni and caused the GB embrittlement phenomena in this alloy [228]. It was further found that different segregation-induced GB superstructures could be formed in Bi-doped polycrystalline Ni, and types of formed GB superstructure depend on the features of GB planes [229]. Similar segregation-induced GB structure transformation was also observed in doped alumina [230], Au-doped Si[231], Ni-W alloys[232], and Cu-Ni alloys[233]. Recently, the "congruent" GB structural transformation was found to more commonly occur than what was previously believed. For example, by using MD simulations, the HAGBs, e.g., Σ5(310) GB, in FCC Cu was found to have multiple stable or metastable phases with different atomic structures with temperature increasing[95]. The coexistence of two different atomic structures at Σ19b GBs in Cu polycrystalline thin film was experimentally evidenced for the first time by employing atomic-resolution HAADF-STEM imaging on the GB structure[234]. Nevertheless, the dynamic process of such structural transformation remains unclear to date, as limited by current postmortem observation. Moreover, less is known about the potential effect of such GB structural transformation on deformation-induced GB migration. Therefore, more endeavors are needed to engage in this field. The in-situ HRTEM technique employed in this dissertation actually offers a great opportunity to explore this open area. Firstly, different HAGBs, e.g., Σ5(310) GB and Σ5(210) GB, in different FCC metals, e.g., Ag, Au, Pt, can be directly fabricated inside the TEM, which largely eliminated the potential effect of impurity segregation. Secondly, the capability of imposing electrical field on the as-fabricated samples with the Nanofactory TEM holder could introduce Joule heating on the samples to elevate the testing temperature, which could consequently trigger the "congruent" GB structural transformation. Thirdly, the capability of imposing both negative and positive bias voltages on the sample side would be helpful to decouple the effect of electrical field on the GB structural transformation. Lastly, in-situ mechanical testing on different GBs under gradient level of electrical field could be performed to unveil the effect of GB structural transformation on shear-coupled GB migration.

Severe plastic deformation of metallic materials not only causes the deformation-induced formation of GBs, but can also lead to twinning, phase transformation, and/or amorphization. For instance, the dominant deformation mechanism of CrCoNo-based FCC HEAs was found to gradually transform from dislocation motion into twinning, phase transformation, and eventually amorphization with increasing degrees of deformation [235], i.e., stress/strain and strain rate. In elemental FCC metals, a recent in-situ HRTEM study on the bending deformation of Pt, Ag, and Au nanocrystals revealed the continuous and reversible FCC-BCT phase transformation in Pt [236], the FCC-BCT-HCP-FCC phase transformation mediated twinning in Ag [237], and the strain-induced local amorphization in Au [238]. The results shown in Chapter 6 mention the formation of an extended GB region during the GB annihilation process. A similar extended GB region was observed during the bending-deformation of another Au nanowire with different axial and bending directions, as shown in Figure 8.1. Notably, this extended GB region, denoted as ‘thick” GB here, consisted of BCT Au. Different from previous studies, the BCT Au observed here was not formed either at a small local region [236] or as an intermediate stage of phase transformation [237]. Instead, it serves the role of GB, which has not been reported yet. The effect of such type of GB on the deformation behavior of FCC metals remains unclear and needs to be explored in the future.

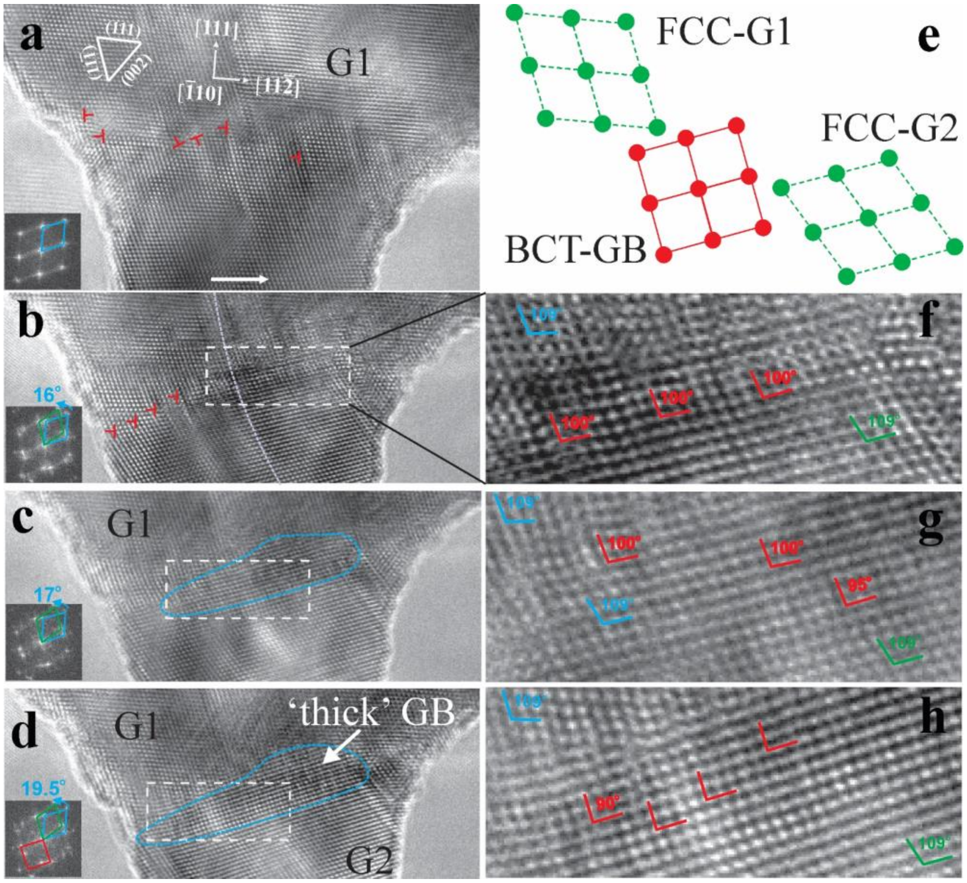
a
(111)
(002)
[111]
[1̄10]
[112̄]
G1
FCC-G1
e
FCC-G2
BCT-GB
b
16°
f
109°
100°
100°
100°
100°
109°
c
G1
17°
g
109°
100°
100°
109°
95°
109°
d
G1
'thick' GB
19.5°
G2
h
109°
90°
109°

Figure 8.1 Bending-induced formation of a 'thick' GB region consisted of BCT Au in FCC Au nanocrystal. (a-d) Sequential HRTEM images showing the formation process. **(e)** Schematic of the atomic structure of FCC Au in grain 1 (G1) and grain 2 (G2) and BCT Au in GB. **(f-h)** Enlarged views of selected GB regions in **(b-d).**

Bibliography

1. Hirth, John P, *The influence of grain boundaries on mechanical properties*. Springer. 1972

2. Guo, Xin and Rainer Waser, *Electrical properties of the grain boundaries of oxygen ion conductors: acceptor-doped zirconia and ceria.* Progress in Materials Science, 51(2): 151-210. 2006.

3. Greuter, Felix and Gianni Blatter, *Electrical properties of grain boundaries in polycrystalline compound semiconductors.* Semiconductor Science and Technology, 5(2): 111. 1990.

4. Gao, Nan, Yu Guo, Si Zhou, Yizhen Bai, and Jijun Zhao, *Structures and magnetic properties of MoS2 grain boundaries with antisite defects.* The Journal of Physical Chemistry C, 121(22): 12261-12269. 2017.

5. Wachowicz, E, T Ossowski, and A Kiejna, *Cohesive and magnetic properties of grain boundaries in bcc Fe with Cr additions.* Physical Review B, 81(9): 094104. 2010.

6. Gottstein, Gunter and Lasar S Shvindlerman, *Grain boundary migration in metals: thermodynamics, kinetics, applications*. CRC press.2009

7. Han, Jian, Spencer L. Thomas, and David J. Srolovitz, *Grain-boundary kinetics: A unified approach.* Progress in Materials Science, 98: 386-476. 2018.

8. Hansen, Niels, *Hall–Petch relation and boundary strengthening.* Scripta Materialia, 51(8): 801-806. 2004.

9. Farkas, Diana, H Van Swygenhoven, and Pm Derlet, *Intergranular fracture in nanocrystalline metals.* Physical Review B, 66(6): 060101. 2002.

10. Schiøtz, Jakob and Karsten W. Jacobsen, *A Maximum in the Strength of Nanocrystalline Copper.* Science, 301(5638): 1357-1359. 2003.

11. Jacobsen, Karsten W. and Jakob Schiøtz, *Nanoscale plasticity.* Nature Materials, 1(1): 15-16. 2002.

12. Wang, Lihua, Yin Zhang, Zhi Zeng, Hao Zhou, Jian He, Pan Liu, Mingwei Chen, Jian Han, David J. Srolovitz, Jiao Teng, Yizhong Guo, Guo Yang, Deli Kong, En Ma, Yongli Hu, Baocai Yin, Xiaoxu Huang, Ze Zhang, Ting Zhu, and Xiaodong Han, *Tracking the sliding of grain boundaries at the atomic scale.* Science, 375(6586): 1261-1265. 2022.

13. Van Swygenhoven, H. and P. M. Derlet, *Grain-boundary sliding in nanocrystalline fcc metals.* Physical Review B, 64(22). 2001.

14. Raj, Rishi and Mf Ashby, *On grain boundary sliding and diffusional creep.* Metallurgical transactions, 2(4): 1113-1127. 1971.

15. Liu, P., S. C. Mao, L. H. Wang, X. D. Han, and Z. Zhang, *Direct dynamic atomic mechanisms of strain-induced grain rotation in nanocrystalline, textured, columnar-structured thin gold films.* Scripta Materialia, 64(4): 343-346. 2011.

16. Liu, L., J. Wang, S. K. Gong, and S. X. Mao, *High resolution transmission electron microscope observation of zero-strain deformation twinning mechanisms in Ag.* Phys Rev Lett, 106(17): 175504. 2011.

17. Sharon, J. A., P. C. Su, F. B. Prinz, and K. J. Hemker, *Stress-driven grain growth in nanocrystalline Pt thin films.* Scripta Materialia, 64(1): 25-28. 2011.

18. Ames, Markus, Jürgen Markmann, Rudolf Karos, Andreas Michels, Andreas Tschöpe, and Rainer Birringer, *Unraveling the nature of room temperature grain growth in nanocrystalline materials.* Acta Materialia, 56(16): 4255-4266. 2008.

19. Ma, E., *Instabilities and ductility of nanocrystalline and ultrafine-grained metals.* Scripta Materialia, 49(7): 663-668. 2003.

20. Li, Choh Hsien, E. H. Edwards, J. Washburn, and E. R. Parker, *Stress-induced movement of crystal boundaries.* Acta Metallurgica, 1(2): 223-229. 1953.

21. Fukutomi, Hiroshi and Ryo Horiuchi, *Stress induced migration of symmetric tilt boundaries in aluminum.* Transactions of the Japan Institute of Metals, 22(9): 633-642. 1981.

22. Winning, M., G. Gottstein, and L. S. Shvindlerman, *Stress induced grain boundary motion.* Acta Materialia, 49(2): 211-219. 2001.

23. Winning, M., G. Gottstein, and L. S. Shvindlerman, *On the mechanisms of grain boundary migration.* Acta Materialia, 50(2): 353-363. 2002.

24. Winning, Myrjam, *Motion of 〈1 0 0〉-tilt grain boundaries.* Acta Materialia, 51(20): 6465-6475. 2003.

25. Yoshida, Hidehiro, Kenji Yokoyama, Naoya Shibata, Yuichi Ikuhara, and Taketo Sakuma, *High-temperature grain boundary sliding behavior and grain boundary energy in cubic zirconia bicrystals.* Acta Materialia, 52(8): 2349-2357. 2004.

26. Molodov, D. A., V. A. Ivanov, and G. Gottstein, *Low angle tilt boundary migration coupled to shear deformation.* Acta Materialia, 55(5): 1843-1848. 2007.

27. Gorkaya, Tatiana, Dmitri A. Molodov, and Günter Gottstein, *Stress-driven migration of symmetrical 〈100〉 tilt grain boundaries in Al bicrystals.* Acta Materialia, 57(18): 5396-5405. 2009.

28. Gorkaya, Tatiana, Konstantin D. Molodov, Dmitri A. Molodov, and Günter Gottstein, *Concurrent grain boundary motion and grain rotation under an applied stress.* Acta Materialia, 59(14): 5674-5680. 2011.

29. Molodov, Dmitri A., Tatiana Gorkaya, and Günter Gottstein, *Migration of the Σ7 tilt grain boundary in Al under an applied external stress.* Scripta Materialia, 65(11): 990-993. 2011.

30. Brandenburg, Jann-Erik and Dmitri A. Molodov, *On shear coupled migration of low angle grain boundaries.* Scripta Materialia, 163: 96-100. 2019.

31. Gianola, D. S., S. Van Petegem, M. Legros, S. Brandstetter, H. Van Swygenhoven, and K. J. Hemker, *Stress-assisted discontinuous grain growth and its effect on the deformation behavior of nanocrystalline aluminum thin films.* Acta Materialia, 54(8): 2253-2263. 2006.

32. Rupert, T. J., D. S. Gianola, Y. Gan, and K. J. Hemker, *Experimental Observations of Stress-Driven Grain Boundary Migration.* Science, 326(5960): 1686-1690. 2009.

33. Legros, Marc, Daniel S. Gianola, and Kevin J. Hemker, *In situ TEM observations of fast grain-boundary motion in stressed nanocrystalline aluminum films.* Acta Materialia, 56(14): 3380-3393. 2008.

34. Mompiou, F., D. Caillard, and M. Legros, *Grain boundary shear–migration coupling—I. In situ TEM straining experiments in Al polycrystals.* Acta Materialia, 57(7): 2198-2209. 2009.

35. Rajabzadeh, A., M. Legros, N. Combe, F. Mompiou, and D. A. Molodov, *Evidence of grain boundary dislocation step motion associated to shear-coupled grain boundary migration.* Philosophical Magazine, 93(10-12): 1299-1316. 2013.

36. Wang, Lihua, Tianjiao Xin, Deli Kong, Xinyu Shu, Yanhui Chen, Hao Zhou, Jiao Teng, Ze Zhang, Jin Zou, and Xiaodong Han, *In situ observation of stress induced grain boundary migration in nanocrystalline gold.* Scripta Materialia, 134: 95-99. 2017.

37. Zhu, Q., G. Cao, J. Wang, C. Deng, J. Li, Z. Zhang, and S. X. Mao, *In situ atomistic observation of disconnection-mediated grain boundary migration.* Nat Commun, 10(1): 156. 2019.

38. Zhu, Qi, Qishan Huang, Cao Guang, Xianghai An, Scott X. Mao, Wei Yang, Ze Zhang, Huajian Gao, Haofei Zhou, and Jiangwei Wang, *Metallic nanocrystals with low angle grain boundary for controllable plastic reversibility.* Nature Communications, 11(1): 3100. 2020.

39. Zhu, Q., S. C. Zhao, C. Deng, X. H. An, K. X. Song, S. X. Mao, and J. W. Wang, *In situ atomistic observation of grain boundary migration subjected to defect interaction.* Acta Materialia, 199: 42-52. 2020.

40. Huang, Qishan, Qi Zhu, Yingbin Chen, Mingyu Gong, Jixue Li, Ze Zhang, Wei Yang, Jian Wang, Haofei Zhou, and Jiangwei Wang, *Twinning-assisted dynamic adjustment of grain boundary mobility.* Nature Communications, 12(1): 6695. 2021.

41. Zhu, Qi, Qishan Huang, Haofei Zhou, and Jiangwei Wang, *Inclination-governed deformation of dislocation-type grain boundaries.* Journal of Materials Research, 36(6): 1306-1315. 2021.

42. Randle, Valerie, *The coincidence site lattice and the 'sigma enigma'.* Materials Characterization, 47(5): 411-416. 2001.

43. Balluffi, R. W., A. Brokman, and A. H. King, *CSL/DSC Lattice model for general crystalcrystal boundaries and their line defects.* Acta Metallurgica, 30(8): 1453-1470. 1982.

44. Pond, Rc and W Bollmann, *The symmetry and interfacial structure of bicrystals.* Philosophical Transactions of the Royal Society of London. Series A, Mathematical and Physical Sciences, 292(1395): 449-472. 1979.

45. Ranganathan, S, *On the geometry of coincidence-site lattices.* Acta Crystallographica, 21(2): 197-199. 1966.

46. Wan, Liang, Weizhong Han, and Kai Chen, *Bi-crystallographic lattice structure directs grain boundary motion under shear stress.* Scientific Reports, 5(1): 13441. 2015.

47. Babcock, Se and R_W Balluffi, *Grain boundary kinetics—I. In situ observations of coupled grain boundary dislocation motion, crystal translation and boundary displacement.* Acta Metallurgica, 37(9): 2357-2365. 1989.

48. Babcock, Se and Rw Balluffi, *Grain boundary kinetics—II. In situ observations of the role of grain boundary dislocations in high-angle boundary migration.* Acta Metallurgica, 37(9): 2367-2376. 1989.

49. Clarebrough, Lm and Ct Forwood, *Secondary grain-boundary dislocation nodes at the junction of three grains.* Philosophical Magazine A, 55(2): 217-225. 1987.

50. Wan, Liang and Ju Li, *Shear responses of-tilt {1 1 5}/{1 1 1} asymmetric tilt grain boundaries in fcc metals by atomistic simulations.* Modelling and Simulation in Materials Science and Engineering, 21(5): 055013. 2013.

51. Wan, Liang and Shaoqing Wang, *Shear response of the Σ9⟨110⟩{221} symmetric tilt grain boundary in fcc metals studied by atomistic simulation methods.* Physical Review B, 82(21): 214112. 2010.

52. Cahn, John W. and Jean E. Taylor, *A unified approach to motion of grain boundaries, relative tangential translation along grain boundaries, and grain rotation.* Acta Materialia, 52(16): 4887-4898. 2004.

53. Cahn, John W., Yuri Mishin, and Akira Suzuki, *Coupling grain boundary motion to shear deformation.* Acta Materialia, 54(19): 4953-4975. 2006.

54. Cahn, J. W., Y. Mishin, and A. Suzuki, *Duality of dislocation content of grain boundaries.* Philosophical Magazine, 86(25-26): 3965-3980. 2006.

55. Read, William T and Wjpr Shockley, *Dislocation models of crystal grain boundaries.* Physical Review, 78(3): 275. 1950.

56. Frank, Fc, *Report of the symposium on the plastic deformation of crystalline solids.* Carnegie Institute of Technology, Pittsburgh, 150. 1950.

57. Sutton, Adrian P, *Interfaces in crystalline materials.* Monographs on the Physice and Chemistry of Materials: 414-423. 1995.

58. Caillard, D., F. Mompiou, and M. Legros, *Grain-boundary shear-migration coupling. II. Geometrical model for general boundaries.* Acta Materialia, 57(8): 2390-2402. 2009.

59. Mompiou, F., M. Legros, and D. Caillard, *SMIG model: A new geometrical model to quantify grain boundary-based plasticity.* Acta Materialia, 58(10): 3676-3689. 2010.

60. Mompiou, F., M. Legros, and D. Caillard, *Direct observation and quantification of grain boundary shear-migration coupling in polycrystalline Al.* Journal of Materials Science, 46(12): 4308-4313. 2011.

61. Bollmann, W., *General Geometrical Theory of Crystalline Interfaces*, in *Crystal Defects and Crystalline Interfaces*, W. Bollmann, Editor., Springer Berlin Heidelberg: Berlin, Heidelberg. 143-185. 1970

62. Ashby, M. F., *Boundary defects, and atomistic aspects of boundary sliding and diffusional creep.* Surface Science, 31: 498-542. 1972.

63. Hirth, J. P. and R. W. Balluffi, *On grain boundary dislocations and ledges.* Acta Metallurgica, 21(7): 929-942. 1973.

64. Hirth, J. P., *Dislocations, steps and disconnections at interfaces.* Journal of Physics and Chemistry of Solids, 55(10): 985-989. 1994.

65. Hirth, J. P., J. Wang, and C. N. Tomé, *Disconnections and other defects associated with twin interfaces.* Progress in Materials Science, 83: 417-471. 2016.

66. Anderson, Peter M, John P Hirth, and Jens Lothe, *Theory of dislocations*. Cambridge University Press.2017

67. Pond, R. C. and J. P. Hirth, *Defects at Surfaces and Interfaces*, in *Solid State Physics*, H. Ehrenreich and D. Turnbull, Editors., Academic Press. 287-365. 1994

68. Pond, Rc and Ds Vlachavas, *Bicrystallography.* Proceedings of the Royal Society of London. A. Mathematical and Physical Sciences, 386(1790): 95-143. 1983.

69. Combe, Nicolas, Frédéric Mompiou, and Marc Legros, *Disconnections kinks and competing modes in shear-coupled grain boundary migration.* Physical Review B, 93(2): 024109. 2016.

70. Khater, H. A., A. Serra, R. C. Pond, and J. P. Hirth, *The disconnection mechanism of coupled migration and shear at grain boundaries.* Acta Materialia, 60(5): 2007-2020. 2012.

71. Combe, N., F. Mompiou, and M. Legros, *Heterogeneous disconnection nucleation mechanisms during grain boundary migration.* Physical Review Materials, 3(6). 2019.

72. Thomas, S. L., C. Wei, J. Han, Y. Xiang, and D. J. Srolovitz, *Disconnection description of triple-junction motion.* Proc Natl Acad Sci U S A, 116(18): 8756-8765. 2019.

73. Schönfelder, B, D Wolf, Sr Phillpot, and M Furtkamp, *Molecular-dynamics method for the simulation of grain-boundary migration.* Interface Science, 5(4): 245-262. 1997.

74. Runnels, Brandon and Vinamra Agrawal, *Phase field disconnections: A continuum method for disconnection-mediated grain boundary motion.* Scripta Materialia, 186: 6-10. 2020.

75. Fensin, S. J., M. Asta, and R. G. Hoagland, *Temperature dependence of the structure and shear response of a Σ11 asymmetric tilt grain boundary in copper from molecular-dynamics.* Philosophical Magazine, 92(34): 4320-4333. 2012.

76. Sansoz, F. and J. F. Molinari, *Mechanical behavior of Σ tilt grain boundaries in nanoscale Cu and Al: A quasicontinuum study.* Acta Materialia, 53(7): 1931-1944. 2005.

77. Zhang, Hao, Mikhail I. Mendelev, and David J. Srolovitz, *Mobility of Σ5 tilt grain boundaries: Inclination dependence.* Scripta Materialia, 52(12): 1193-1198. 2005.

78. Zhang, Hao and David J Srolovitz, *Simulation and analysis of the migration mechanism of Σ5 tilt grain boundaries in an fcc metal.* Acta Materialia, 54(3): 623-633. 2006.

79. Mishin, Y, A Suzuki, Bp Uberuaga, and Af Voter, *Stick-slip behavior of grain boundaries studied by accelerated molecular dynamics.* Physical Review B, 75(22): 224101. 2007.

80. Zhang, Hao, David J. Srolovitz, Jack F. Douglas, and James A. Warren, *Atomic motion during the migration of general [001] tilt grain boundaries in Ni.* Acta Materialia, 55(13): 4527-4533. 2007.

81. Ivanov, V. A. and Y. Mishin, *Dynamics of grain boundary motion coupled to shear deformation: An analytical model and its verification by molecular dynamics.* Physical Review B, 78(6): 064106. 2008.

82. Zhang, H., D. Du, and D. J. Srolovitz, *Effects of boundary inclination and boundary type on shear-driven grain boundary migration.* Philosophical Magazine, 88(2): 243-256. 2008.

83. Wang, J., A. Misra, and J. P. Hirth, *Shear response of*$\Sigma 3\{112\}$*twin boundaries in face-centered-cubic metals.* Physical Review B, 83(6). 2011.

84. Trautt, Z. T., A. Adland, A. Karma, and Y. Mishin, *Coupled motion of asymmetrical tilt grain boundaries: Molecular dynamics and phase field crystal simulations.* Acta Materialia, 60(19): 6528-6546. 2012.

85. Homer, Eric R., Stephen M. Foiles, Elizabeth A. Holm, and David L. Olmsted, *Phenomenology of shear-coupled grain boundary motion in symmetric tilt and general grain boundaries.* Acta Materialia, 61(4): 1048-1060. 2013.

86. Frolov, T., *Effect of interfacial structural phase transitions on the coupled motion of grain boundaries: A molecular dynamics study.* Applied Physics Letters, 104(21): 211905. 2014.

87. Zhang, Liang, Cheng Lu, Guillaume Michal, Kiet Tieu, and Kuiyu Cheng, *Molecular dynamics study on the atomic mechanisms of coupling motion of [0 0 1] symmetric tilt grain boundaries in copper bicrystal.* Materials Research Express, 1(1): 015019. 2014.

88. Zhang, Liang, Cheng Lu, Kiet Tieu, Xing Zhao, and Linqing Pei, *Shear Response of Copper Bicrystal with* $\Sigma 11$ *Symmetric and Asymmetric Tilt Grain Boundaries by Molecular Dynamics Simulation.* Nanoscale, 7. 2015.

89. Niu, Liang-Liang, Ying Zhang, Xiaolin Shu, Fei Gao, Shuo Jin, Hong-Bo Zhou, and Guang-Hong Lu, *Shear-coupled grain boundary migration assisted by unusual atomic shuffling.* Scientific Reports, 6(1): 23602. 2016.

90. Wan, Liang, Akio Ishii, Jun-Ping Du, Wei-Zhong Han, Qingsong Mei, and Shigenobu Ogata, *Atomistic modeling study of a strain-free stress driven grain boundary migration mechanism.* Scripta Materialia, 134: 52-56. 2017.

91. Li, Bin and Janel Leung, *Lattice transformation in grain boundary migration via shear coupling and transition to sliding in face-centered-cubic copper.* Acta Materialia, 215: 117127. 2021.

92. Cheng, Kuiyu, Liang Zhang, Cheng Lu, and Kiet Tieu, *Coupled grain boundary motion in aluminium: the effect of structural multiplicity.* Scientific Reports, 6(1): 25427. 2016.

93. Cantwell, Patrick R., Ming Tang, Shen J. Dillon, Jian Luo, Gregory S. Rohrer, and Martin P. Harmer, *Grain boundary complexions.* Acta Materialia, 62: 1-48. 2014.

94. Cantwell, Patrick R., Timofey Frolov, Timothy J. Rupert, Amanda R. Krause, Christopher J. Marvel, Gregory S. Rohrer, Jeffrey M. Rickman, and Martin P. Harmer, *Grain Boundary Complexion Transitions.* Annual Review of Materials Research, 50(1): 465-492. 2020.

95. Frolov, Timofey, David L. Olmsted, Mark Asta, and Yuri Mishin, *Structural phase transformations in metallic grain boundaries.* Nature Communications, 4(1): 1899. 2013.

96. Rajabzadeh, A., F. Mompiou, M. Legros, and N. Combe, *Elementary mechanisms of shear-coupled grain boundary migration.* Phys Rev Lett, 110(26): 265507. 2013.

97. Larranaga, M, F Mompiou, M Legros, and N Combe, *Role of sessile disconnection dipoles in shear-coupled grain boundary migration.* Physical Review Materials, 4(12): 123606. 2020.

98. Chen, Dengke, Shuozhi Xu, and Yashashree Kulkarni, *Atomistic mechanism for vacancy-enhanced grain boundary migration.* Physical Review Materials, 4(3). 2020.

99. Farkas, Diana, Anders Frøseth, and Helena Van Swygenhoven, *Grain boundary migration during room temperature deformation of nanocrystalline Ni.* Scripta Materialia, 55(8): 695-698. 2006.

100. Aramfard, Mohammad and Chuang Deng, *Influences of triple junctions on stress-assisted grain boundary motion in nanocrystalline materials.* Modelling and Simulation in Materials Science and Engineering, 22(5): 055012. 2014.

101. Basak, Anup and Anurag Gupta, *Simultaneous grain boundary motion, grain rotation, and sliding in a tricrystal.* Mechanics of Materials, 90: 229-242. 2015.

102. Panzarino, Jason F., Zhiliang Pan, and Timothy J. Rupert, *Plasticity-induced restructuring of a nanocrystalline grain boundary network.* Acta Materialia, 120: 1-13. 2016.

103. Thomas, S. L., K. Chen, J. Han, P. K. Purohit, and D. J. Srolovitz, *Reconciling grain growth and shear-coupled grain boundary migration.* Nat Commun, 8(1): 1764. 2017.

104. Lim, A. T., M. Haataja, W. Cai, and D. J. Srolovitz, *Stress-driven migration of simple low-angle mixed grain boundaries.* Acta Materialia, 60(3): 1395-1407. 2012.

105. Hadian, R., B. Grabowski, C. P. Race, and J. Neugebauer, *Atomistic migration mechanisms of atomically flat, stepped, and kinked grain boundaries.* Physical Review B, 94(16). 2016.

106. Hadian, R., B. Grabowski, M. W. Finnis, and J. Neugebauer, *Migration mechanisms of a faceted grain boundary.* Physical Review Materials, 2(4). 2018.

107. Ovid'ko, I. A., R. Z. Valiev, and Y. T. Zhu, *Review on superior strength and enhanced ductility of metallic nanomaterials.* Progress in Materials Science, 94: 462-540. 2018.

108. Zheng, Si-Xue, Xue-Mei Luo, Dong Wang, and Guang-Ping Zhang, *A novel evaluation strategy for fatigue reliability of flexible nanoscale films.* Materials Research Express, 5(3): 035012. 2018.

109. Tjong, S. C. and Haydn Chen, *Nanocrystalline materials and coatings.* Materials Science and Engineering: R: Reports, 45(1): 1-88. 2004.

110. Li, Bl, A Godfrey, and Q Liu, *Subdivision of original grains during cold-rolling of interstitial-free steel.* Scripta Materialia, 50(6): 879-883. 2004.

111. Kamikawa, N., T. Sakai, and N. Tsuji, *Effect of redundant shear strain on microstructure and texture evolution during accumulative roll-bonding in ultralow carbon IF steel.* Acta Materialia, 55(17): 5873-5888. 2007.

112. Estrin, Yuri and Alexei Vinogradov, *Extreme grain refinement by severe plastic deformation: A wealth of challenging science.* Acta Materialia, 61(3): 782-817. 2013.

113. Tsuji, Nobuhiro, Reza Gholizadeh, Rintaro Ueji, Naoya Kamikawa, Lijia Zhao, Yanzhong Tian, Yu Bai, and Akinobu Shibata, *Formation mechanism of ultrafine grained microstructures: various possibilities for fabricating bulk nanostructured metals and alloys.* Materials Transactions, 60(8): 1518-1532. 2019.

114. Zheng, Si-Xue, Xue-Mei Luo, and Guang-Ping Zhang, *Cumulative shear strain–induced preferential orientation during abnormal grain growth near fatigue crack tips of nanocrystalline Au films.* Journal of Materials Research, 35(4): 372-379. 2020.

115. Wang, L., J. Teng, P. Liu, A. Hirata, E. Ma, Z. Zhang, M. Chen, and X. Han, *Grain rotation mediated by grain boundary dislocations in nanocrystalline platinum.* Nat Commun, 5: 4402. 2014.

116. Bachurin, D. V., A. A. Nazarov, and J. Weissmüller, *Grain rotation by dislocation climb in a finite-size grain boundary.* Acta Materialia, 60(20): 7064-7077. 2012.

117. Rittner, J. D., D. N. Seidman, and K. L. Merkle, *Grain-boundary dissociation by the emission of stacking faults.* Physical Review B, 53(8): R4241-R4244. 1996.

118. Luo, Xue-Mei, Xiao-Fei Zhu, and Guang-Ping Zhang, *Nanotwin-assisted grain growth in nanocrystalline gold films under cyclic loading.* Nature Communications, 5(1): 3021. 2014.

119. Wang, Meimei, Zhiming Li, and Dierk Raabe, *In-situ SEM observation of phase transformation and twinning mechanisms in an interstitial high-entropy alloy.* Acta Materialia, 147: 236-246. 2018.

120. Li, Yat, Fang Qian, Jie Xiang, and Charles M. Lieber, *Nanowire electronic and optoelectronic devices.* Materials Today, 9(10): 18-27. 2006.

121. Hu, Liangbing, Han Sun Kim, Jung-Yong Lee, Peter Peumans, and Yi Cui, *Scalable Coating and Properties of Transparent, Flexible, Silver Nanowire Electrodes.* Acs Nano, 4(5): 2955-2963. 2010.

122. Despont, M., J. Brugger, U. Drechsler, U. Dürig, W. Häberle, M. Lutwyche, H. Rothuizen, R. Stutz, R. Widmer, G. Binnig, H. Rohrer, and P. Vettiger, *VLSI-NEMS chip for parallel AFM data storage.* Sensors and Actuators A: Physical, 80(2): 100-107. 2000.

123. Husain, A., J. Hone, Henk W. Ch Postma, X. M. H. Huang, T. Drake, M. Barbic, A. Scherer, and M. L. Roukes, *Nanowire-based very-high-frequency electromechanical resonator.* Applied Physics Letters, 83(6): 1240-1242. 2003.

124. Zheng, H., J. Wang, J. Y. Huang, A. Cao, and S. X. Mao, *In situ visualization of birth and annihilation of grain boundaries in an Au nanocrystal.* Phys Rev Lett, 109(22): 225501. 2012.

125. Lee, Subin, Jiseong Im, Youngdong Yoo, Erik Bitzek, Daniel Kiener, Gunther Richter, Bongsoo Kim, and Sang Ho Oh, *Reversible cyclic deformation mechanism of gold nanowires by twinning–detwinning transition evidenced from in situ TEM.* Nature Communications, 5(1): 3033. 2014.

126. Park, Harold S., Ken Gall, and Jonathan A. Zimmerman, *Shape Memory and Pseudoelasticity in Metal Nanowires.* Physical Review Letters, 95(25): 255504. 2005.

127. Lao, Jijun and Dorel Moldovan, *Surface stress induced structural transformations and pseudoelastic effects in palladium nanowires.* Applied Physics Letters, 93(9): 093108. 2008.

128. Mcdowell, Matthew T, Austin M Leach, and Ken Gall, *Bending and tensile deformation of metallic nanowires.* Modelling and Simulation in Materials Science and Engineering, 16(4): 045003. 2008.

129. Ni, C., H. Ding, C. Li, L. T. Kong, and X. J. Jin, *Pseudo-elasticity and ultra-high recoverable strain in cobalt nanowire: A molecular dynamics study.* Scripta Materialia, 68(3): 191-194. 2013.

130. Nöhring, Wolfram G., Johannes J. Möller, Zhuocheng Xie, and Erik Bitzek, *Wedge-shaped twins and pseudoelasticity in fcc metallic nanowires under bending.* Extreme Mechanics Letters, 8: 140-150. 2016.

131. Yang, Yang, Suzhi Li, Xiangdong Ding, Jun Sun, and Ekhard Kh Salje, *Interface driven pseudo‐elasticity in a‐Fe nanowires.* Advanced Functional Materials, 26(5): 760-767. 2016.

132. Rezaei, Reza and Chuang Deng, *Pseudoelasticity and shape memory effects in cylindrical FCC metal nanowires.* Acta Materialia, 132: 49-56. 2017.

133. Li, Shuang, Nanjun Chen, Aashish Rohatgi, Yulan Li, Cynthia A. Powell, Suveen Mathaudhu, Arun Devaraj, Shenyang Hu, and Chongmin Wang, *Nanotwin assisted reversible formation of low angle grain boundary upon reciprocating shear load.* Acta Materialia, 230: 117850. 2022.

134. Wang, Lihua, Deli Kong, Yin Zhang, Lirong Xiao, Yan Lu, Zhigang Chen, Ze Zhang, Jin Zou, Ting Zhu, and Xiaodong Han, *Mechanically Driven Grain Boundary Formation in Nickel Nanowires.* Acs Nano, 11(12): 12500-12508. 2017.

135. Goodhew, P. J., T. Y. Tan, and R. W. Balluffi, *Low energy planes for tilt grain boundaries in gold.* Acta Metallurgica, 26(4): 557-567. 1978.

136. Hamilton, J. C., Donald J. Siegel, Istvan Daruka, and François Léonard, *Why Do Grain Boundaries Exhibit Finite Facet Lengths?* Physical Review Letters, 90(24): 246102. 2003.

137. He, Yang, Bin Li, Chongmin Wang, and Scott X. Mao, *Direct observation of dual-step twinning nucleation in hexagonal close-packed crystals.* Nature Communications, 11(1): 2483. 2020.

138. Wang, J., Y. Wang, W. Cai, J. Li, Z. Zhang, and S. X. Mao, *Discrete shear band plasticity through dislocation activities in body-centered cubic tungsten nanowires.* Sci Rep, 8(1): 4574. 2018.

139. Zheng, Sixue, Xiang Wang, Susheng Tan, Guofeng Wang, and Scott X. Mao, *Atomistic processes of diffusion-induced unusual compression fracture in metallic nanocrystals.* Materials Research Letters, 10(12): 805-812. 2022.

140. Zheng, Sixue, Shuhei Shinzato, Shigenobu Ogata, and Scott X. Mao, *Experimental molecular dynamics for individual atomic-scale plastic events in nanoscale crystals.* Journal of the Mechanics and Physics of Solids, 158: 104687. 2022.

141. Zheng, Sixue and Scott X. Mao, *Advances in experimental mechanics at atomic scale.* Extreme Mechanics Letters, 45: 101284. 2021.

142. Zheng, S and Sx Mao, *In situ atomic-scale observation of dislocation-mediated discrete plasticity in nanoscale crystals.* Material Science & Engineering International Journal, 5(3): 93-94. 2021.

143. Plimpton, Steve, *Fast Parallel Algorithms for Short-Range Molecular Dynamics.* Journal of Computational Physics, 117(1): 1-19. 1995.

144. Grochola, Gregory, Salvy P. Russo, and Ian K. Snook, *On fitting a gold embedded atom method potential using the force matching method.* The Journal of Chemical Physics, 123(20): 204719. 2005.

145. Gautam, A., C. Ophus, F. Lançon, V. Radmilovic, and U. Dahmen, *Atomic structure characterization of an incommensurate grain boundary.* Acta Materialia, 61(13): 5078-5086. 2013.

146. Lancon, F., J. Ye, D. Caliste, T. Radetic, A. M. Minor, and U. Dahmen, *Superglide at an internal incommensurate boundary*. Nano Lett, 10(2): 695-700. 2010.

147. Brown, J. A. and Y. Mishin, *Dissociation and faceting of asymmetrical tilt grain boundaries: Molecular dynamics simulations of copper*. Physical Review B, 76(13). 2007.

148. Stukowski, Alexander, *Visualization and analysis of atomistic simulation data with OVITO–the Open Visualization Tool.* Modelling and Simulation in Materials Science and Engineering, 18(1): 015012. 2009.

149. Fang, Zhengwu, Jianwei Xiao, Susheng Tan, Chuang Deng, Guofeng Wang, and Scott X. Mao, *Atomic-scale observation of dynamic grain boundary structural transformation during shear-mediated migration.* Science Advances, 8(45): eabn3785. 2022.

150. Priester, Louisette, *Grain boundaries: from theory to engineering*. Vol. 172. Springer Science & Business Media.2012

151. Schuh, Christopher A., Mukul Kumar, and Wayne E. King, *Analysis of grain boundary networks and their evolution during grain boundary engineering.* Acta Materialia, 51(3): 687-700. 2003.

152. Babcock, S. E. and R. W. Balluffi, *Grain boundary kinetics—II. In situ observations of the role of grain boundary dislocations in high-angle boundary migration.* Acta Metallurgica, 37(9): 2367-2376. 1989.

153. Rae, C. M. F. and D. A. Smith, *On the mechanisms of grain boundary migration.* Philosophical Magazine A, 41(4): 477-492. 1980.

154. Randle, V., *Overview No. 127The role of the grain boundary plane in cubic polycrystals.* Acta Materialia, 46(5): 1459-1480. 1998.

155. Mccarthy, Megan J. and Timothy J. Rupert, *Emergence of directionally-anisotropic mobility in a faceted Σ11 ⟨110⟩ tilt grain boundary in Cu.* Modelling and Simulation in Materials Science and Engineering, 28(5): 055008. 2020.

156. Mccarthy, Megan J. and Timothy J. Rupert, *Shuffling mode competition leads to directionally anisotropic mobility of faceted \ensuremath{\Sigma}11 boundaries in fcc metals.* Physical Review Materials, 4(11): 113402. 2020.

157. Rajabzadeh, A., F. Mompiou, S. Lartigue-Korinek, N. Combe, M. Legros, and D. A. Molodov, *The role of disconnections in deformation-coupled grain boundary migration.* Acta Materialia, 77: 223-235. 2014.

158. Randle, V., *Asymmetric tilt boundaries in polycrystalline nickel.* Acta Crystallographica Section A, 50(5): 588-595. 1994.

159. Masteller, M. S. and C. L. Bauer, *Faceting of migrating 〈110〉 coincidence boundaries in aluminium bicrystals.* Philosophical Magazine A, 38(6): 697-706. 1978.

160. Merkle, K. L., L. J. Thompson, and F. Phillipp, *In-Situ HREM Studies of Grain Boundary Migration.* Interface Science, 12(2): 277-292. 2004.

161. Wei, Jiake, Bin Feng, Ryo Ishikawa, Tatsuya Yokoi, Katsuyuki Matsunaga, Naoya Shibata, and Yuichi Ikuhara, *Direct imaging of atomistic grain boundary migration.* Nature Materials. 2021.

162. Smith, Laura and Diana Farkas, *Non-planar grain boundary structures in fcc metals and their role in nano-scale deformation mechanisms.* Philosophical Magazine, 94(2): 152-173. 2014.

163. Bhattacharya, Aditi, Yu-Feng Shen, Christopher M. Hefferan, Shiu Fai Li, Jonathan Lind, Robert M. Suter, Carl E. Krill, and Gregory S. Rohrer, *Grain boundary velocity and curvature are not correlated in Ni polycrystals.* 374(6564): 189-193. 2021.

164. Merkle, Karl L., *High-resolution electron microscopy of grain boundaries.* Interface Science, 2(4): 311-345. 1995.

165. Duparc, O. Hardouin, S. Poulat, A. Larere, J. Thibault, and L. Priester, *High-resolution transmission electron microscopy observations and atomic simulations of the structures of exact and near Σ = 11, {332} tilt grain boundaries in nickel.* Philosophical Magazine A, 80(4): 853-870. 2000.

166. Medlin, D. L., D. Cohen, and R. C. Pond, *Accommodation of coherency strain by interfacial disconnections at a 90° 〈110〉 grain boundary in gold.* Philosophical Magazine Letters, 83(4): 223-232. 2003.

167. Hardouinduparc, O., J. Couzinie, J. Thibaultpenisson, S. Lartiguekorinek, B. Decamps, and L. Priester, *Atomic structures of symmetrical and asymmetrical facets in a near Σ=9{221} tilt grain boundary in copper.* Acta Materialia, 55(5): 1791-1800. 2007.

168. Rittner, J. D. and D. N. Seidman, *〈110〉 symmetric tilt grain-boundary structures in fcc metals with low stacking-fault energies.* Physical Review B, 54(10): 6999-7015. 1996.

169. Merkle, K. L., L. J. Thompson, and Fritz Phillipp, *high-resolution electron microscopy at a (113) symmetric Thermally activated step motion observed by tilt grain-boundary in aluminium.* Philosophical Magazine Letters, 82(11): 589-597. 2002.

170. Merkle, Karl L., *Atomic structure of grain boundaries.* Journal of Physics and Chemistry of Solids, 55(10): 991-1005. 1994.

171. Barrett, Christopher D. and Haitham El Kadiri, *Fundamentals of mobile tilt grain boundary faceting.* Scripta Materialia, 84-85: 15-18. 2014.

172. Barrett, Christopher D. and Haitham El Kadiri, *Impact of deformation faceting on {101¯2},{101¯1} and {101¯3} embryonic twin nucleation in hexagonal close-packed metals.* Acta Materialia, 70: 137-161. 2014.

173. Wang, Chunyang, Huichao Duan, Chunjin Chen, Peng Wu, Dongqing Qi, Hengqiang Ye, Hai-Jun Jin, Huolin L. Xin, and Kui Du, *Three-Dimensional Atomic Structure of Grain Boundaries Resolved by Atomic-Resolution Electron Tomography.* Matter, 3(6): 1999-2011. 2020.

174. Merkle, K. L. and D. Wolf, *Quasiperiodic features in the atomic structure of long-period grain boundaries.* Materials Letters, 17(5): 217-222. 1993.

175. Bowers, M. L., C. Ophus, A. Gautam, F. Lancon, and U. Dahmen, *Step Coalescence by Collective Motion at an Incommensurate Grain Boundary*. Phys Rev Lett, 116(10): 106102. 2016.

176. Hong, Hyun Uk, Hi Won Jeong, In Soo Kim, Baig Gyu Choi, Young Soo Yoo, and Chang Yong Jo, *Significant decrease in interfacial energy of grain boundary through serrated grain boundary transition.* Philosophical Magazine, 92(22): 2809-2825. 2012.

177. Lee, Sung Bo, Wilfried Sigle, Wolfgang Kurtz, and Manfred Rühle, *Temperature dependence of faceting in Σ5(310)[001] grain boundary of SrTiO3.* Acta Materialia, 51(4): 975-981. 2003.

178. Hsieh, T. E. and R. W. Balluffi, *Observations of roughening/de-faceting phase transitions in grain boundaries.* Acta Metallurgica, 37(8): 2133-2139. 1989.

179. Miyazawa, K, Y Iwasaki, K Ito, and Y %J Acta Crystallographica Section A: Foundations of Crystallography Ishida, *Combination rule of Σ values at triple junctions in cubic polycrystals.* 52(6): 787-796. 1996.

180. Garg, A., W. A. T. Clark, and J. P. Hirth, *Dissociated and faceted large-angle coincident-site-lattice boundaries in silicon.* Philosophical Magazine A, 59(3): 479-499. 1989.

181. Radetic, T., F. Lancon, and U. Dahmen, *Chevron defect at the intersection of grain boundaries with free surfaces in Au.* Phys Rev Lett, 89(8): 085502. 2002.

182. Fang, Zhengwu, Boyang Li, Susheng Tan, Scott Mao, and Guofeng Wang, *Revealing shear-coupled migration mechanism of a mixed tilt-twist grain boundary at atomic scale.* Acta Materialia: 119237. 2023.

183. Hu, Jian, Yn Shi, X Sauvage, G Sha, and K Lu, *Grain boundary stability governs hardening and softening in extremely fine nanograined metals.* Science, 355(6331): 1292-1296. 2017.

184. Liebig, Jan P., Mirza Mačković, Erdmann Spiecker, Mathias Göken, and Benoit Merle, *Grain boundary mediated plasticity: A blessing for the ductility of metallic thin films?* Acta Materialia, 215: 117079. 2021.

185. Zhang, B. B., Y. G. Tang, Q. S. Mei, X. Y. Li, and K. Lu, *Inhibiting creep in nanograined alloys with stable grain boundary networks.* Science, 378(6620): 659-663. 2022.

186. Molodov, Konstantin D. and Dmitri A. Molodov, *Grain boundary mediated plasticity: On the evaluation of grain boundary migration - shear coupling.* Acta Materialia, 153: 336-353. 2018.

187. Randle, V., G. S. Rohrer, H. M. Miller, M. Coleman, and G. T. Owen, *Five-parameter grain boundary distribution of commercially grain boundary engineered nickel and copper.* Acta Materialia, 56(10): 2363-2373. 2008.

188. Combe, Nicolas, Frédéric Mompiou, and Marc %J Physical Review B Legros, *Disconnections kinks and competing modes in shear-coupled grain boundary migration.* 93(2): 024109. 2016.

189. Wan, Liang and Ju Li, *Shear responses of -tilt {1 1 5}/{1 1 1} asymmetric tilt grain boundaries in fcc metals by atomistic simulations.* Modelling and Simulation in Materials Science and Engineering, 21(5): 055013. 2013.

190. Deymier, P. A., M. Shamsuzzoha, and J. D. Weinberg, *Experimental evidence for a structural unit model of quasiperiodic grain boundaries in aluminum.* Journal of Materials Research, 6(7): 1461-1468. 1991.

191. Sun, Xianhu, Dongxiang Wu, Lianfeng Zou, Stephen D. House, Xiaobo Chen, Meng Li, Dmitri N. Zakharov, Judith C. Yang, and Guangwen Zhou, *Dislocation-induced stop-and-go kinetics of interfacial transformations.* Nature, 607(7920): 708-713. 2022.

192. Hirth, J. P. and R. C. Pond, *Compatibility and accommodation in displacive phase transformations.* Progress in Materials Science, 56(6): 586-636. 2011.

193. Pond, R. C., D. L. Medlin, and A. Serra, *A study of the accommodation of coherency strain by interfacial defects at a grain boundary in gold.* Philosophical Magazine, 86(29-31): 4667-4684. 2006.

194. Hirth, Jp and Rc %J Acta Materialia Pond, *Steps, dislocations and disconnections as interface defects relating to structure and phase transformations.* 44(12): 4749-4763. 1996.

195. Humberson, Jonathan and Elizabeth A. Holm, *Anti-thermal mobility in the Σ3 [111] 60° {11 8 5} grain boundary in nickel: Mechanism and computational considerations.* Scripta Materialia, 130: 1-6. 2017.

196. Guo, Yizhong, Jiao Teng, Guo Yang, Ang Li, Yao Deng, Chengpeng Yang, Lihua Wang, Xin Yan, Ze Zhang, Xiaoyan Li, En Ma, and Xiaodong Han, *In situ observation of atomic-scale processes accomplishing grain rotation at mixed grain boundaries.* Acta Materialia, 241: 118386. 2022.

197. Liu, B. Y., J. Wang, B. Li, L. Lu, X. Y. Zhang, Z. W. Shan, J. Li, C. L. Jia, J. Sun, and E. Ma, *Twinning-like lattice reorientation without a crystallographic twinning plane.* Nat Commun, 5: 3297. 2014.

198. Liu, Bo-Yu, Zhen Zhang, Fei Liu, Nan Yang, Bin Li, Peng Chen, Yu Wang, Jin-Hua Peng, Ju Li, En Ma, and Zhi-Wei Shan, *Rejuvenation of plasticity via deformation graining in magnesium.* Nature Communications, 13(1): 1060. 2022.

199. Kou, Zongde, Yanqing Yang, Lixia Yang, Bin Huang, and Xian Luo, *In situ atomic-scale observation of a novel lattice reorienting process in pure Ti.* Scripta Materialia, 166: 144-148. 2019.

200. Hua, Anping and Junhua Zhao, *Shear direction induced transition mechanism from grain boundary migration to sliding in a cylindrical copper bicrystal.* International Journal of Plasticity, 156: 103370. 2022.

201. Zhu, Qi, Lingyi Kong, Haiming Lu, Qishan Huang, Yingbin Chen, Yue Liu, Wei Yang, Ze Zhang, Frederic Sansoz, Haofei Zhou, and Jiangwei Wang, *Revealing extreme twin-boundary shear deformability in metallic nanocrystals.* Science Advances, 7(36): eabe4758. 2021.

202. Zhang, Luchan, Jian Han, Yang Xiang, and David J Srolovitz, *Equation of motion for a grain boundary.* Physical Review Letters, 119(24): 246101. 2017.

203. Van Swygenhoven, H., P. M. Derlet, and A. Hasnaoui, *Atomic mechanism for dislocation emission from nanosized grain boundaries.* Physical Review B, 66(2): 024101. 2002.

204. Li, Qizhen, Lihua Wang, Jiao Teng, Xiaolu Pang, Xiaodong Han, and Jin Zou, *In-situ observation of cooperative grain boundary sliding and migration in the nano-twinned nanocrystalline-Au thin-films.* Scripta Materialia, 180: 97-102. 2020.

205. Chen, Kongtao, Jian Han, Spencer L. Thomas, and David J. Srolovitz, *Grain boundary shear coupling is not a grain boundary property.* Acta Materialia, 167: 241-247. 2019.

206. Li, Huafang, Pengyu Wang, and Cuie Wen, *Recent Progress on Nanocrystalline Metallic Materials for Biomedical Applications.* Nanomaterials, 12(12): 2111. 2022.

207. Baghbanan, Mohammadreza, Uwe Erb, and Gino Palumbo, *Towards the application of nanocrystalline metals in MEMS.* physica status solidi (a), 203(6): 1259-1264. 2006.

208. Valiev, Ruslan Zafarovich, Rinat K Islamgaliev, and Igor V Alexandrov, *Bulk nanostructured materials from severe plastic deformation.* Progress in Materials Science, 45(2): 103-189. 2000.

209. Hughes, D. A. and N. Hansen, *High angle boundaries formed by grain subdivision mechanisms.* Acta Materialia, 45(9): 3871-3886. 1997.

210. Gao, Huajian and Yonggang Huang, *Geometrically necessary dislocation and size-dependent plasticity.* Scripta Materialia, 48(2): 113-118. 2003.

211. Wang, C., K. Du, K. Song, X. Ye, L. Qi, S. He, D. Tang, N. Lu, H. Jin, F. Li, and H. Ye, *Size-Dependent Grain-Boundary Structure with Improved Conductive and Mechanical Stabilities in Sub-10-nm Gold Crystals.* Phys Rev Lett, 120(18): 186102. 2018.

212. Bulatov, Vasily V., Bryan W. Reed, and Mukul Kumar, *Grain boundary energy function for fcc metals.* Acta Materialia, 65: 161-175. 2014.

213. Chen, Peng, Fangxi Wang, and Bin Li, *Transitory phase transformations during {101¯2} twinning in titanium.* Acta Materialia, 171: 65-78. 2019.

214. Medlin, D. L. and J. C. Hamilton, *Formation of hexagonal close packing at a grain boundary in gold by the dissociation of a dense array of crystal lattice dislocations.* Journal of Materials Science, 44(13): 3608-3617. 2009.

215. Cao, Guang, Jiangwei Wang, Kui Du, Xuelu Wang, Jixue Li, Ze Zhang, and Scott X. Mao, *Superplasticity in Gold Nanowires through the Operation of Multiple Slip Systems.* Advanced Functional Materials, 28(51). 2018.

216. Zheng, H., A. Cao, C. R. Weinberger, J. Y. Huang, K. Du, J. Wang, Y. Ma, Y. Xia, and S. X. Mao, *Discrete plasticity in sub-10-nm-sized gold crystals.* Nat Commun, 1: 144. 2010.

217. Wang, Xiang, Sixue Zheng, Shuhei Shinzato, Zhengwu Fang, Yang He, Li Zhong, Chongmin Wang, Shigenobu Ogata, and Scott X. Mao, *Atomistic processes of surface-diffusion-induced abnormal softening in nanoscale metallic crystals.* Nature Communications, 12(1): 5237. 2021.

218. Wang, Xiang, Sixue Zheng, Chuang Deng, Christopher R. Weinberger, Guofeng Wang, and Scott X. Mao, *In Situ Atomic-Scale Observation of 5-Fold Twin Formation in Nanoscale Crystal under Mechanical Loading.* Nano Letters, 23(2): 514-522. 2023.

219. Wang, J. W., S. Narayanan, J. Y. Huang, Z. Zhang, T. Zhu, and S. X. Mao, *Atomic-scale dynamic process of deformation-induced stacking fault tetrahedra in gold nanocrystals.* Nat Commun, 4: 2340. 2013.

220. Bilby, Bruce Alexander, R Bullough, and Edwin Smith, *Continuous distributions of dislocations: a new application of the methods of non-Riemannian geometry.* Proceedings of the Royal Society of London. Series A. Mathematical and Physical Sciences, 231(1185): 263-273. 1955.

221. Han, Jian, Vaclav Vitek, and David J. Srolovitz, *The grain-boundary structural unit model redux.* Acta Materialia, 133: 186-199. 2017.

222. Nes, E., K. Marthinsen, and Y. Brechet, *On the mechanisms of dynamic recovery.* Scripta Materialia, 47(9): 607-611. 2002.

223. Xu, Zipeng, Christopher M. Hefferan, Shiu Fai Li, Jonathan Lind, Robert M. Suter, Fadi Abdeljawad, and Gregory S. Rohrer, *Energy dissipation by grain boundary replacement during grain growth.* Scripta Materialia, 230: 115405. 2023.

224. Winning, Myrjam and Anthony D. Rollett, *Transition between low and high angle grain boundaries.* Acta Materialia, 53(10): 2901-2907. 2005.

225. Orlova, Ts, Am Mavlyutov, As Bondarenko, Ia Kasatkin, M Yu Murashkin, and Rz Valiev, *Influence of grain boundary state on electrical resistivity of ultrafine grained aluminium.* Philosophical Magazine, 96(23): 2429-2444. 2016.

226. Zhang, Qg, X Zhang, By Cao, M Fujii, Koji Takahashi, and T Ikuta, *Influence of grain boundary scattering on the electrical properties of platinum nanofilms.* Applied Physics Letters, 89(11): 114102. 2006.

227. Miyajima, Yoji, Shin-Ya Komatsu, Masatoshi Mitsuhara, Satoshi Hata, Hideharu Nakashima, and Nobuhiro Tsuji, *Change in electrical resistivity of commercial purity aluminium severely plastic deformed.* Philosophical Magazine, 90(34): 4475-4488. 2010.

228. Luo, Jian, Huikai Cheng, Kaveh Meshinchi Asl, Christopher J. Kiely, and Martin P. Harmer, *The Role of a Bilayer Interfacial Phase on Liquid Metal Embrittlement.* Science, 333(6050): 1730-1733. 2011.

229. Yu, Zhiyang, Patrick R. Cantwell, Qin Gao, Denise Yin, Yuanyao Zhang, Naixie Zhou, Gregory S. Rohrer, Michael Widom, Jian Luo, and Martin P. Harmer, *Segregation-induced ordered superstructures at general grain boundaries in a nickel-bismuth alloy.* Science, 358(6359): 97-101. 2017.

230. Dillon, Shen J. and Martin P. Harmer, *Direct Observation of Multilayer Adsorption on Alumina Grain Boundaries.* Journal of the American Ceramic Society, 90(3): 996-998. 2007.

231. Ma, Shuailei, Kaveh Meshinchi Asl, Chookiat Tansarawiput, Patrick R Cantwell, Minghao Qi, Martin P Harmer, and Jian Luo, *A grain boundary phase transition in Si–Au.* Scripta Materialia, 66(5): 203-206. 2012.

232. Detor, A. J., M. K. Miller, and C. A. Schuh, *Solute distribution in nanocrystalline Ni–W alloys examined through atom probe tomography.* Philosophical Magazine, 86(28): 4459-4475. 2006.

233. Reda Chellali, Mohammed, Zoltan Balogh, and Guido Schmitz, *Nano-analysis of grain boundary and triple junction transport in nanocrystalline Ni/Cu.* Ultramicroscopy, 132: 164-170. 2013.

234. Meiners, T., T. Frolov, R. E. Rudd, G. Dehm, and C. H. Liebscher, *Observations of grain-boundary phase transformations in an elemental metal.* Nature, 579(7799): 375-378. 2020.

235. Zhao, Shiteng, Zezhou Li, Chaoyi Zhu, Wen Yang, Zhouran Zhang, David E. J. Armstrong, Patrick S. Grant, Robert O. Ritchie, and Marc A. Meyers, *Amorphization in extreme deformation of the CrMnFeCoNi high-entropy alloy.* Science Advances, 7(5): eabb3108. 2021.

236. Wang, L., P. Liu, P. Guan, M. Yang, J. Sun, Y. Cheng, A. Hirata, Z. Zhang, E. Ma, M. Chen, and X. Han, *In situ atomic-scale observation of continuous and reversible lattice deformation beyond the elastic limit.* Nat Commun, 4: 2413. 2013.

237. Sun, Shiduo, Dongwei Li, Chenpeng Yang, Libo Fu, Deli Kong, Yan Lu, Yizhong Guo, Danmin Liu, Pengfei Guan, Ze Zhang, Jianghua Chen, Wenquan Ming, Lihua Wang, and Xiaodong Han, *Direct Atomic-Scale Observation of Ultrasmall Ag Nanowires that Exhibit fcc, bcc, and hcp Structures under Bending.* Physical Review Letters, 128(1): 015701. 2022.

238. Wang, Zhanxin, Nianke Chen, Xianbin Li, Jiao Teng, Yizhong Guo, Libo Fu, Zihao Zhang, Evan Ma, Lihua Wang, Ze Zhang, and Xiaodong Han, *Atomic-scale observation of strain-induced local amorphization in face-centered cubic metals.* Scripta Materialia, 212: 114553. 2022.